# An Experimental Study of $CO_2$ sequestration in saline aquifers and gas hydrates

Master Thesis in Reservoir Physics


Vegard Havre Paulsen

Department of Physics and Technology

University of Bergen

June 2014

## Summary

Processes related to the displacement of brine by $CO_2$ were studied in core flood experiments in high-permeable, homogeneous Bentheim sandstone using a medical CT scanner. These processes are of high relevance for prediction of $CO_2$ storage capabilities and flow functions related to plume-migration of carbon dioxide injection in saline aquifers. Both saturated and unsaturated $CO_2$ and brine phases were injected in the rock with rates ranging from 0.1-70ml/min. The experimental pressures and temperatures range from 9MPa to 10MPa and 25˚C to 50˚C, respectively, resulting in realistic $CO_2$ sequestration conditions for both supercritical and liquid $CO_2$. The experimental system used in the experiments was built specifically for these experiments, something considered quite challenging.

Saturation profiles and fluid distributions, residual saturations and capillary pressure curves were extracted from CT data and differential pressures over the core. A time-efficient method emulating a spontaneous imbibition process was successfully utilized: slugs of brine were injected prior to stepwise decreasing rates of $CO_2$ injection. The method used to obtain capillary pressure data is a fairly new method where capillary pressure curves can be measured in as little as 10 hours, with the sample remaining intact. Residual $CO_2$ saturations of up to 21.9% of pore volume were observed throughout the experiments, with the highest value coming from the liquid $CO_2$-brine displacements. Viscous displacement seemed to be the main driving force of the displacements and corresponded well with changes in differential and absolute pressure.

The possibility of storing $CO_2$ in natural gas hydrate systems was studied by injecting liquid $CO_2$ in a Bentheim sandstone core with preformed methane hydrate. The temperature was 4˚C and the pressure was 86bar. It is previously shown that a spontaneous exchange process between carbon dioxide and methane takes place due to carbon dioxide being a more thermodynamically stable hydrate former than methane, resulting in safe carbon dioxide storage in hydrate form and a recovery of methane. It was observed that $CO_2$ flowed through the system and also remained in the core after the injection and estimates were made regarding the amount stored in hydrate and as free gas in the pores.

## Acknowledgements

First off, I would like to express my gratitude to Professor Arne Graue and Associate Professor Geir Ersland for providing me with an exciting task, a great research environment and the opportunity to learn and experience lots through relevant subjects and study trips.

A special thanks to PhD candidate Lars Petter Øren Hauge for guidance and collaboration in the hydrate lab and also in planning and building the system used at Haukeland University Hospital as well as the execution of the experiments there. In addition I would like to thank Associate Professor Martin Fernø who has also been a great resource in the project at Haukeland and Dr. Stefan Iglauer whom the Haukeland experiments were conducted in collaboration with.

Thanks to all of my fellow students and everybody else who ventures around the institute for good times, laughter, encouragement, inspiration and so much more. A special thank you to Villy Nielsen for delivering me my mail to my office, supplying me with nourishing food I ordered for more effective work.

Thanks to the guys at the workshop for building parts of the setups and always being able to help, and to Werner Olsen for guidance in building electric components for the heating wire.

Last but not least I would like to thank my family and friends. I love you!

Bergen, September 8, 2014

Vegard Havre Paulsen

# Contents

Summary ..... 3

Acknowledgements ..... 5

Preface ..... 9

Introduction ..... 11

1. Carbon Capture and Storage (CCS) ..... 13

1.1. Carbon dioxide capture ..... 14

1.2. Transport of $CO_2$ ..... 15

1.3. Storage of $CO_2$ ..... 16

1.3.1. Geological storage ..... 16

1.3.2. Ocean storage, mineral carbonation and industrial uses ..... 17

1.4. Principles for $CO_2$ trapping ..... 18

1.4.1. Stratigraphic and structural trapping ..... 19

1.4.2. Residual $CO_2$ trapping and capillary pressure ..... 19

1.4.3. Solubility trapping ..... 23

1.4.4. Mineral trapping ..... 25

1.5. Industrial-scale storage projects ..... 26

1.5.1. The Sleipner project ..... 26

1.5.2. In Salah ..... 27

1.5.3. The Weyburn $CO_2$-EOR Project ..... 28

2. Fundamentals and $CO_2$ storage potential of Natural Gas Hydrates ..... 31

2.1. Natural Gas ..... 32

2.2. Hydrate structures ..... 33

2.3. Cavities and guest molecules ..... 34

2.4. Hydrate thermodynamics and kinetics ..... 36

2.5. Hydrates in nature ..... 39

2.5.1. Hydrate resources ..... 39

2.5.2. Classification of hydrate resources ..... 42

2.6. Production methods for natural gas hydrates ..... 43

2.6.1. Production by dissociation ..... 43

2.6.2. Production by $CH_4$-$CO_2$ exchange ..... 44

2.7. Natural gas hydrate field studies ..... 46

2.7.1. Messoyakha ..... 46
2.7.2. Mallik ..... 47
2.7.3. Ignik Sikumi ..... 47
3. Literature survey ..... 51
4. Experimental setups and procedures ..... 53
4.1. Rock properties ..... 53
4.2. Fluids ..... 54
4.3. Core preparation ..... 56
4.4. Experimental setup and procedure at Haukeland University Hospital ..... 57
4.4.1. Experimental setup at Haukeland University Hospital ..... 57
4.4.2. Computed tomography (CT) imaging ..... 59
4.4.3. CT imaging of $CO_2$ and brine displacements at Haukeland University Hospital ..... 62
4.5. Experimental setup and procedure at the hydrate lab ..... 67
4.5.1. Experimental setup at the hydrate lab ..... 67
4.5.2. $CH_4$-$CO_2$ exchange at the hydrate lab ..... 70
5. Results and discussion ..... 71
5.1. CT imaging of live $CO_2$ and live brine displacements ..... 71
5.1.1. 100% scans for reference purposes ..... 73
5.1.2. Primary drainage ..... 75
5.1.3. Spontaneous imbibition ..... 82
5.1.4. Forced imbibition ..... 84
5.1.5. Secondary drainage ..... 90
5.1.6. Effect of different pressures ..... 93
5.1.7. Capillary pressure ..... 94
5.2. $CH_4$-$CO_2$ exchange at the hydrate lab ..... 97
5.3. Uncertainties ..... 102
6. Conclusions and future work ..... 107
References ..... 109
APPENDIX ..... 113
Nomenclature ..... 113
Appendix A ..... 114

# Preface

According to the 5th Assessment Report "Climate Change 2014: Mitigation of Climate Change" by Working Group III of the IPCC the annual global greenhouse gas (GHG) emissions have continued to grow and reached 49.5 billion tonnes (Gt) of carbon dioxide equivalents in the year 2010, higher than any level prior to that date. Despite robust evidence that GHG emissions have grown at about twice the rate from 2000 to 2010, it seems that the most important driving forces for climate policy in nearly all countries are not the concern about climate change, but economic and political profit. Policies to mitigate emissions are extremely complex and the global financial crisis (2007-2008) has put a spanner in the works for many of the political and socioeconomic processes to mitigate climate change.

The effect fossil fuels have on climate change has been and still is by many regarded as one of our modern world society`s most important issues. Changes must occur in order not to surpass the famous two degree Celsius target ceiling. A total stop in the production and usage of fossil fuels is most likely not going to happen in the current paradigm of the powers that be. According to IPCC`s 2005 report most scenarios project that the supply of primary energy will continue to be dominated by fossil fuels until at least the middle of the century. A transition period with energy efficiency improvements, the switch to less carbon-intensive fuels, nuclear power, solar power and carbon dioxide ($CO_2$) capture and storage (CCS) may be an option. A large fraction of climate change is largely irreversible on human time scales, unless net anthropogenic $CO_2$ emissions were strongly negative over a sustained period of time (Intergovernmental Panel on Climate Change, 2013).

# Introduction

Carbon dioxide can be captured from industrial and energy-related sources, then be compressed and transported for storage in i.e. geological formations. As much as 85-95% of the $CO_2$ processed in a capture plant can be captured with available technology (Intergovernmental Panel on Climate Change, 2005).

Several $CO_2$ storage projects exist around the world, whereas three of them will be discussed in this thesis. Statoil started storing $CO_2$, for economic benefits, in the Utsira Formation in 1996 and during the first 12 years of the projects 11Mt of $CO_2$ was injected (Wright et al., 2009) and The Weyburn project in Canada aims to store 20Mt of $CO_2$ during its lifetime (Condor et al., 2010). Many of the storage projects are started due to governmental taxation, as well as increased interest for EOR.

In order to better understand fluid behavior in saline aquifers used for $CO_2$ storage CT imaging has proven to be a good asset. CT imaging has been used to show that local capillary trapping is an effective and safe storage mechanism. Trapped supercritical $CO_2$ clusters were imaged showing that clusters occupied 25% of the pore space in a sandstone at elevated pressures and temperatures (Iglauer et al., 2011a). Pini also presented a novel method of obtaining capillary pressure curves using CT imaging and differential pressure; important for a better understanding of the processes related to safe storage (Pini et al., 2011). This method from Pini has been tried out in the work conducted for this thesis.

In August 2008 the experimental work to better the understanding of multi-phase flow and processes for $CO_2$ storage in $CO_2$-water systems was started in the reservoir physics group at the Institute for Physics and Technology. The work started with an initiative from Professor Arne Graue, Dr. Åsmund Haugen and MSc. Knut Arne Birkedal who utilized imaging with radioactive tracers to visualize injection of $CO_2$ in water saturated chalk. Brautaset et al. (2008) studied in situ $CO_2$-oil behavior during EOR experiments using MRI. Fluid flow was monitored in situ during waterfloods and subsequent injection of liquid or supercritical $CO_2$ in four Portland Chalk core samples. Several in-house studies on visualization of $CO_2$ flow by PET/CT and NTI imaging have been conducted, mostly for the purpose of EOR. This thesis will focus on the storage aspect of $CO_2$ injection in aquifer systems and in hydrate bearing sediments.

The Department of Physics and Technology at UoB have studied $CH_4$-$CO_2$ exchange as a hydrate production method as well as a $CO_2$ sequestration method for many years. Verification of this exchange process using MRI was studied in-house (Graue et al., 2006b, Baldwin et al., 2009, Ersland et al., 2010), as well as a study focusing on $CO_2$ storage and the spontaneous methane production (Graue et al.,

2006a, Kvamme et al., 2007, Ersland et al., 2009). Knut Arne Birkedal conducted a study focusing on geomechanical stability during $CH_4$-$CO_2$ exchange (Birkedal et al., 2010).

This thesis focuses on safe $CO_2$ storage in saline aquifers and in gas hydrates. Experiments utilizing CT imaging are carried out to better understand fluid flow behavior in brine filled sandstone, as well as a quick method to obtain capillary pressure curves. Due to experimental problems and faulty equipment in the hydrate lab only one $CH_4$-$CO_2$ exchange experiment was conducted to continue the hydrate work of the institute and to further observe $CO_2$ storage possibilities in hydrates.

Chapter 1 and 2 consist of basic theory relevant to the experimental work conducted for this thesis. Chapter 1 focuses on carbon capture and storage (CCS). Storage opportunities in gas hydrates, $CH_4$-$CO_2$ exchange and gas hydrates in general are fairly unconventional subjects and the fundamentals of these subjects are presented in chapter 2. Chapter 3 is a literature study of some relevant publications for the subject of this thesis. Chapter 4 shows the experimental setups and procedures and the results are presented and discussed in chapter 5. Chapter 6 contains conclusions and future work.

# 1. Carbon Capture and Storage (CCS)

Carbon dioxide ($CO_2$) capture and storage (CCS) is the process consisting of the separation of $CO_2$ from industrial and energy-related sources, transport to a storage location and long-term isolation from the atmosphere (Intergovernmental Panel on Climate Change, 2005).

Capture of $CO_2$ can be applied to large point sources like large fossil fuel or biomass energy facilities, major $CO_2$-emitting industries, natural gas production, synthetic fuel plants and fossil fuel-based hydrogen production plants. The $CO_2$ is captured, compressed and transported for storage in i.e. geological formations. Available technology captures about 85-95% of the $CO_2$ processed in a capture plant, but 10-40% more energy is needed than for a plant without CCS, most of which is for capture and compression (Intergovernmental Panel on Climate Change, 2005). A power plant with CCS can emit 80-90% less $CO_2$ than a plant without CCS, but it also produces a larger total amount of $CO_2$, as seen in Figure 1-1.

This section will cover the fundamentals of CCS, its potential and challenges and give field examples. The 2005 report "Carbon Dioxide Capture and Storage" by the Intergovernmental Panel on Climate Change is recommended for further reading and major parts of this chapter is based on information collected in the report.

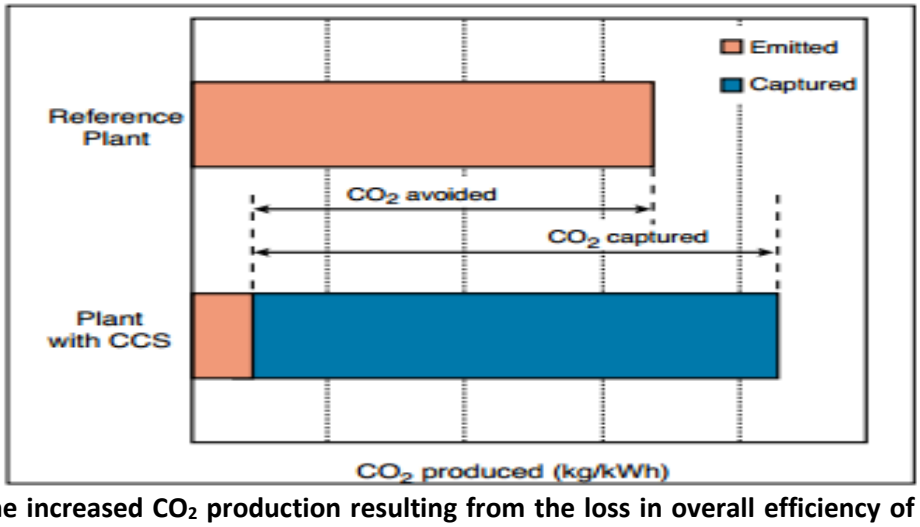


**Figure 1-1. The increased $CO_2$ production resulting from the loss in overall efficiency of power plants due to the additional energy needed for capture, transport and storage result in a larger amount of total $CO_2$ produced (lower bar) relative to the reference plant (upper bar) without a capture system (Intergovernmental Panel on Climate Change, 2005).**

## 1.1. Carbon dioxide capture

The capture of $CO_2$ is the most challenging and costly part of carbon capture and storage. Changes and additions to current carbon emitting points need to be made in order to capture $CO_2$. There are currently three main approaches to capturing $CO_2$: post-combustion, pre-combustion and oxyfuel combustion (Intergovernmental Panel on Climate Change, 2005).

Post-combustion systems separate $CO_2$ from the exhaust gases produced when the fuel in question combusts in air. Current post-combustion capture systems normally employ an organic solvent such as monoethanolamine (MEA), or another liquid solvent, to capture the $CO_2$. The fraction of $CO_2$ in the exhaust gas stream is typically 3-15% by volume and the main constituent is nitrogen from the air. This method can be applied to existing $CO_2$-sources with some modifications because it separates $CO_2$ after combustion.

Pre-combustion systems separate $CO_2$ before any combustion happens. The primary fuel is processed in a reactor with steam and oxygen to produce a mixture rich in hydrogen and carbon monoxide. A second reactor, called a “shift reactor”, produces more hydrogen and $CO_2$ from a reaction with steam. The next step is then to separate the hydrogen for fuel usage, and $CO_2$ for storage. These systems produce concentrations of $CO_2$, 15-60% by volume, making them more favorable for $CO_2$ separation. The downsides are, however, that it is a more costly and complex process than post-combustion capture.

Oxyfuel combustion systems use pure oxygen (95-99%) instead of air for combustion of the primary fuel. The result is a flue gas consisting of mainly water vapor and $CO_2$. This flue has $CO_2$ concentrations greater than 80% by volume. The water vapor, any air pollutants and non-condensed gases (such as nitrogen) is removed and the $CO_2$ is sent for storage. Oxyfuel combustion systems are still in the demonstration phase and the process of separating oxygen from air is costly.

## 1.2. Transport of $CO_2$

Unless the carbon capture-plant is directly above the storage site, the $CO_2$ needs to be transported to a suitable storage location. Pipelines, both onshore and offshore, are the most common method for transporting $CO_2$. The cost of transport in pipelines decreases when the mass flow rate per year increases. Other ways of transport are by ships, road or railroad. In Figure 1-2, the costs of the different transport methods are plotted against distance.

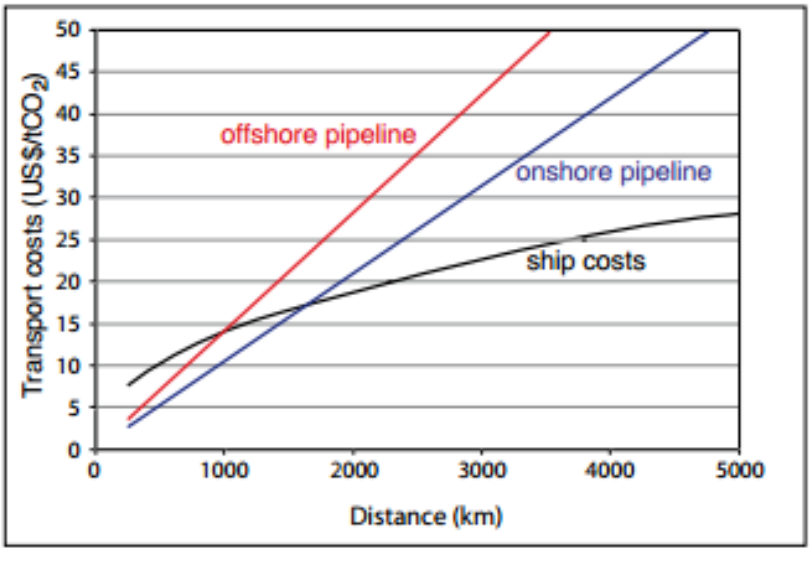


**Figure 1-2. Costs (USD/t$CO_2$ transported) plotted against transport distance for onshore pipelines, offshore pipelines and ship transport. Pipeline costs are given for a mass flow of 6Mt$CO_2$/yr. Ship cost include temporary storage facilities, harbor fees, fuel costs, and loading and unloading activities. Additional costs for liquefaction compared to compression are also included (Intergovernmental Panel on Climate Change, 2005).**

Pipelines are subject to internal corrosion during dense phase $CO_2$ transportation and experiments have shown that corrosion may take place at water concentrations far below the water solubility in a pure water-CO2 system when impurities, i.e. SOx, NOx and $O_2$ are present (Dugstad and Halseid, 2012).

## 1.3. Storage of $CO_2$

This section examines different ways in which carbon dioxide can be stored or put out of the carbon cycle. Geological storage, ocean storage, mineral carbonation and industrial uses are some main categories in this regard. In addition, storage in natural gas hydrate reservoirs is looked in to.

### 1.3.1. Geological storage

Geological storage can be further divided into three types: storage in oil and gas reservoirs, deep saline aquifer formations and unminable coal beds. In all of the abovementioned $CO_2$ is injected in a dense form into rock formations deep below the surface of the earth. This thesis will focus on storage in deep saline formations and storage in natural gas hydrate reservoirs in the form of $CO_2$-hydrate. The exchange process between $CH_4$ and $CO_2$ in the hydrates will be discussed in chapter 2 of this thesis.

Depleted oil and gas reservoirs, and also saline aquifers, have already held fluids such as natural gas, oil and brine confined within a geological structure over geological time. Hence they are potential candidates for $CO_2$ storage. Sedimentary basins, both offshore and onshore, can be suitable storage formations. Storage of $CO_2$ in hydrocarbon reservoirs or deep saline formations is usually expected to take place at depths where the temperature and pressure is high enough for $CO_2$ to be liquid or supercritical. In general, depths below 800m are needed for this. The resulting density of $CO_2$ is 50-80% the density of water; hence buoyancy forces will drive $CO_2$ upwards. This results in the need for a sealing (impermeable) cap-rock, just as in a common hydrocarbon reservoir.

$CO_2$ can be stored in coal beds where it is unlikely that the coal will later be mined, provided that permeability is sufficient. This can also enhance methane production. $CO_2$ storage in unminable coal beds is still in the demonstration phase (Intergovernmental Panel on Climate Change, 2005). Many coal basins containing ideal beds for sequestration are near many $CO_2$ emitting sources and coal has the potential to trap $CO_2$ for a long time dependent on the rank, quality and geology of the coal beds (Stanton et al.).

### 1.3.2. Ocean storage, mineral carbonation and industrial uses

There are several methods for carbon dioxide storage that have been thought of and considered executed, some more relevant than others. This section will briefly discuss ways to store $CO_2$ that are not included in the work done in this thesis.

Ocean storage is a potential way to store $CO_2$ at depths greater than 1000m. It is still in the research phase and there have been small-scale field experiments. Ocean storage can be achieved by transporting $CO_2$ via pipelines or ships and inject it into the water column of the ocean or at the sea floor. This means that the dissolved $CO_2$ still will be a part of the carbon cycle (Intergovernmental Panel on Climate Change, 2005). The ocean is able to hold an amount of CO2 that is highly connected to the temperature of the ocean. Higher $CO_2$ levels in the ocean also means a lower pH-value, and acidification of the oceans compromise natural ecosystems (Hoegh-Guldberg et al., 2007). Hence ocean storage is not considered a feasible option.

Mineral carbonation is a method of fixating $CO_2$ as mineral components in naturally occurring rocks. The reaction between i.e. magnesium oxide (MgO) and $CO_2$ produces magnesium carbonate ($MgCO_3$). These chemical reactions are slow and would need to be accelerated considerably to be a viable storage method for $CO_2$ captured from anthropogenic sources (Intergovernmental Panel on Climate Change, 2005).

Industrial uses of $CO_2$ include chemical and biological processes utilizing $CO_2$ (i.e. methanol production), direct use of $CO_2$ (i.e. the horticulture industry, refrigeration, food packaging, fire extinguishers etc.), and EOR use. Two thirds of this $CO_2$ is used to produce urea. Industrial uses could lead to an increase in overall emissions of $CO_2$, rather than a net reduction (Intergovernmental Panel on Climate Change, 2005).

## 1.4. Principles for $CO_2$ trapping

Some of the most important principles for $CO_2$ storage in geological formations will be explained in this section. Deposited and transported rock grains and organic material as well as minerals that are formed after the rocks are deposited constitute the geological formations in the subsurface. The space between the grains, the pore space, is occupied by fluids that may be displaced when $CO_2$ is injected. $CO_2$ may also dissolve in or mix with the fluid or react with the minerals. As seen in Figure 1-3, the physical process of residual $CO_2$ trapping and geochemical processes of solubility trapping and mineral trapping increase with time (Intergovernmental Panel on Climate Change, 2005). This section will briefly cover stratigraphic and structural trapping, residual $CO_2$ trapping, solubility trapping, mineral trapping as well as storage as hydrate in gas reservoirs.

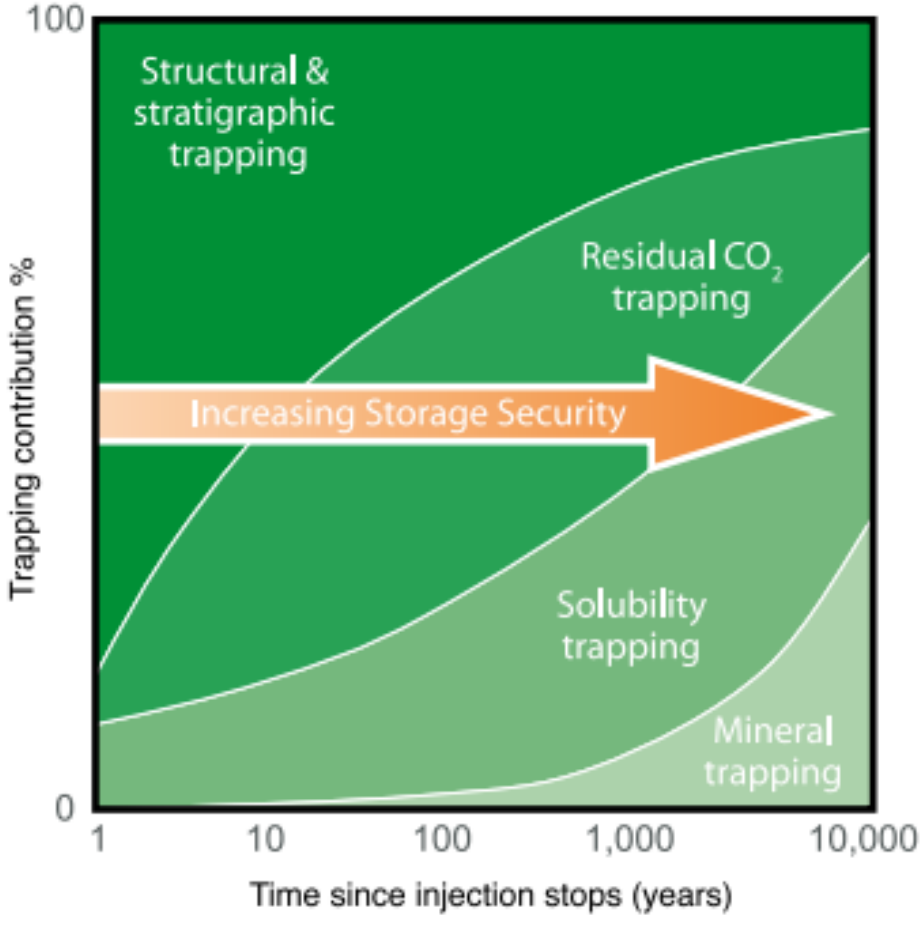


**Figure 1-3. Storage safety relies on a combination of physical and geochemical trapping. The physical process of residual $CO_2$ trapping and geochemical processes of solubility trapping and mineral trapping increases over time, with mineral trapping being most time-dependent. (Intergovernmental Panel on Climate Change, 2005)**

### 1.4.1. Stratigraphic and structural trapping

Physical trapping of $CO_2$ below sealing, low-permeable caprocks (i.e. shale or salt) is the main option for $CO_2$ storage in geological formations. Shallow gas hydrates may also act as a seal. Sedimentary basins can have such trapping structures and are occupied mainly by saline water, oil and gas. $CO_2$ is less dense than water and buoyancy forces will drive it upwards when it is injected in a saline formation. Along this route some $CO_2$ will be left immobile as residual $CO_2$ saturation (Intergovernmental Panel on Climate Change, 2005).

Structural traps include those formed by folded or fractured rocks, i.e. faults. Faults may act as both permeability barriers and conduits of flow (Seeburger, 1981). Stratigraphic traps are formed by changes in rock type caused by variation in the sediments and setting in the area of deposition. Both of these trap types are fitting for $CO_2$ storage, but to avoid fracturing the caprock or re-activating faults a specific burden pressure must not be exceeded (Sibson, 1995).

### 1.4.2. Residual $CO_2$ trapping and capillary pressure

Residual trapping, or capillary trapping, involves $CO_2$ bubbles being trapped as an immobile phase surrounded by brine. This is dependent on displacement hysteresis and the capillary pressure characteristics of the $CO_2$-brine system. Residual $CO_2$ trapping can occur over shorter timeframes relative to the other trapping mechanisms and is proven; hence it is important for CCS (Pentland, 2010). Miscibility, wettability and contact angle hysteresis are aspects that are important in order to understand capillary trapping and will be discussed briefly in this section. For further reading, the PhD thesis written by Christopher Pentland in 2010 is recommended.

Supercritical $CO_2$ and brine are mutually soluble and mass transfer will occur between them when $CO_2$ is injected into an aquifer. This mass transfer will occur near the well and at the front of the $CO_2$ plume and in these areas the displacement is miscible (see Figure 1-4). However the biggest region will be the immiscible displacement region, where $CO_2$ is saturated with brine and brine is saturated with $CO_2$. This is the most important region for assessing $CO_2$ storage potential.

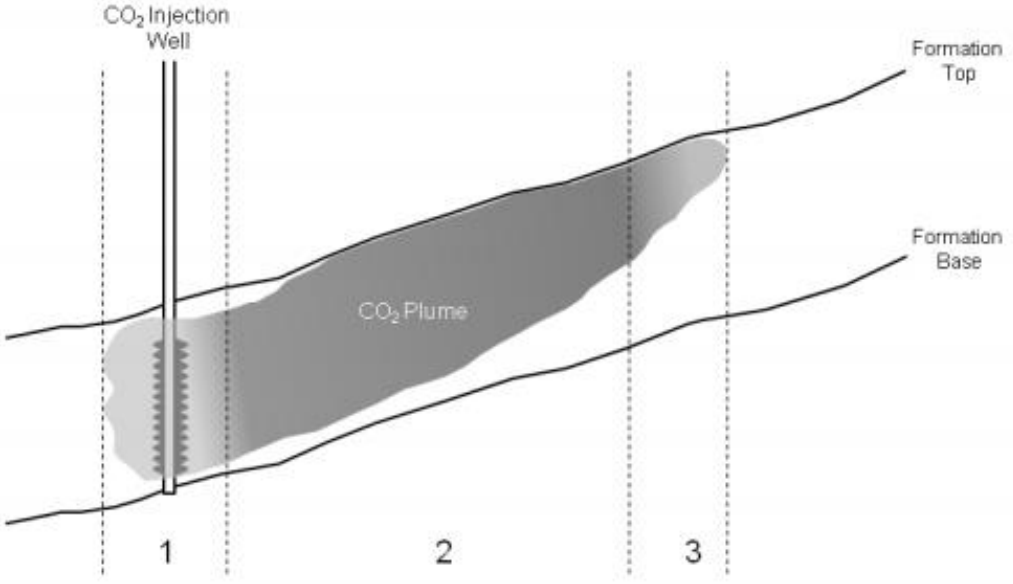


**Figure 1-4. A cross-section of a storage formation illustrating the migration path of an injected $CO_2$ plume. Three displacement regions are shown: (1) Near-wellbore region: formation water dissolves into the freshly injected (dry) $CO_2$. (2) $CO_2$ and brine are equilibrated: saturation changes in the pore space are a result of immiscible phase on phase displacements. (3) Leading edge of the $CO_2$ plume where $CO_2$ comes into contact with under-saturated formation brine and $CO_2$ dissolves into the brine. (Pentland, 2010)**

Equilibrated $CO_2$ and brine will have an interface, and an interfacial tension, between them due to the difference in cohesive forces between the molecules at the surface of each phase and the molecules in the bulk of each phase. In Figure 1-5, these fluids are shown together with a solid surface. A contact angle, $\theta$, between the $CO_2$-brine interface and the solid surface is shown. The contact angle is measured through the denser phase and if $\theta$ < 90˚ the system prefers the denser phase, in this case water. The contact angle can be used to determine the wettability of the system. The system is said to be water-wet when the contact angle is less than 75˚, intermediate-wet for contact angles between 75˚ and 105˚ and oil-wet ($CO_2$-wet) for contact angles larger than 75˚ (Treiber and Owens, 1972). When the non-wetting phase ($CO_2$) displaces the wetting phase (brine) in a porous system, the contact angle will be smaller than in an opposite scenario. In the first scenario the wetting phase saturation is decreasing and in the second scenario the wetting phase saturation is increasing. These two processes are called drainage and imbibition, respectively. This difference in contact angle shows that the contact angle is dependent upon the current and previous flow sequences. This is called the hysteresis of the system (Pentland, 2010).

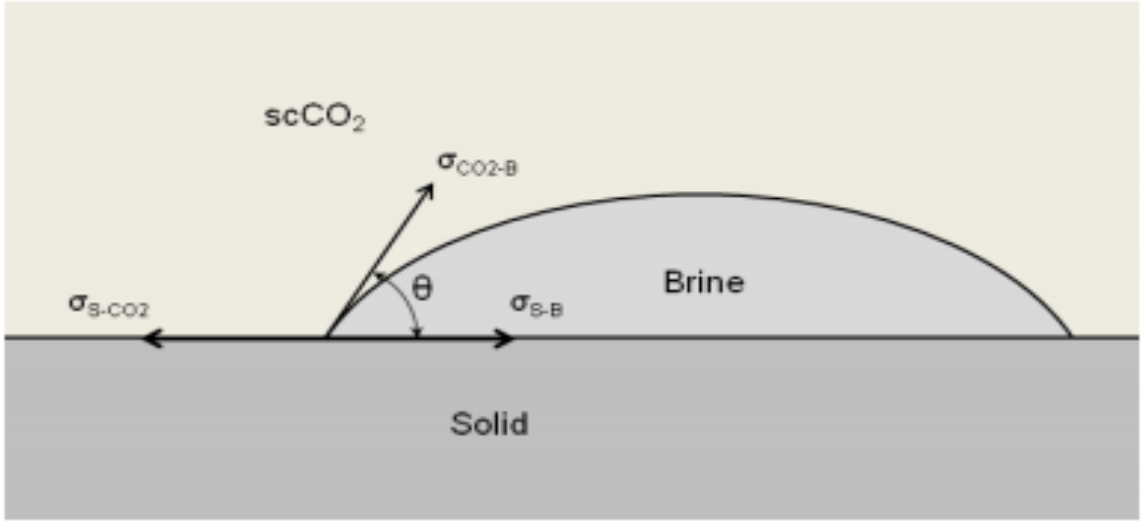


**Figure 1-5. Contact angle and interfacial tensions in a three-phase ($CO_2$-brine-solid) system. sc stands for supercritical and the interfacial tension is denoted by σ (Pentland, 2010).**

In a porous water-wet system a primary drainage will result in $CO_2$ occupying the center of progressively smaller pores as the injection pressure increases. A thin water-film is retained on the rock surface. This can be seen in Figure 1-6a. When water imbibes into the system again, the water-film will get thicker and thicker and in many pores $CO_2$ will be left as immobile droplets surrounded by brine. These droplets are not inter-connected and are controlled by local capillary forces. This effect is called snap off and the result can be seen in Figure 1-6b.

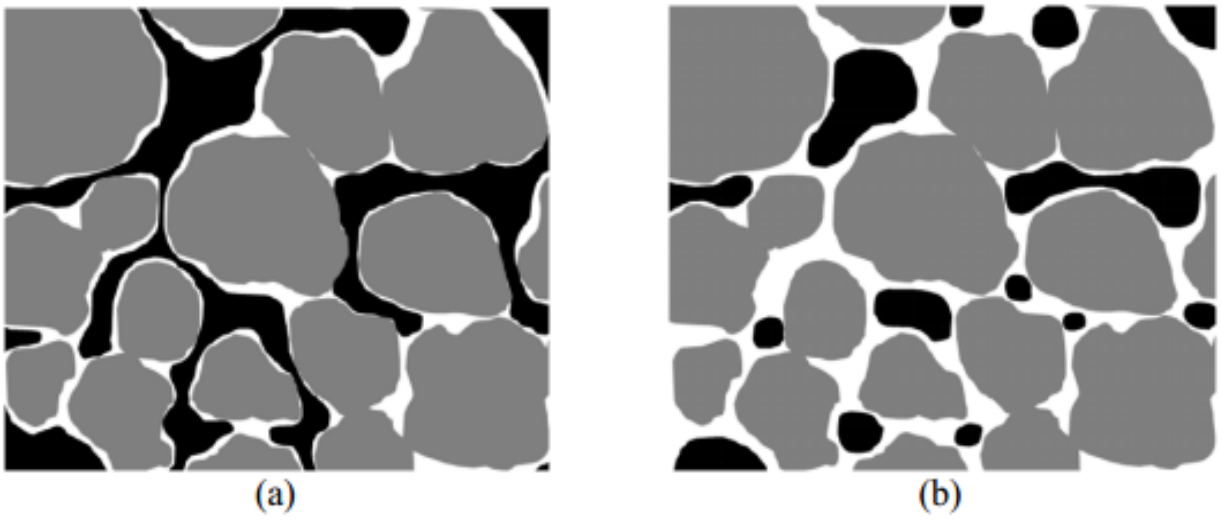


**Figure 1-6. Example of distribution of $CO_2$ (black) and brine (white) within an idealised porous media (grey). (a) $CO_2$ saturation after primary drainage. (b) Residual $CO_2$ saturation after waterflooding. (Pentland, 2010).**

Capillary pressure is defined as the difference in pressure between the non-wetting phase and wetting phase and can be seen as a force that pulls a fluid upwards, such as absorbing fluid in a paper towel. As seen in Figure 1-7 the water raises in a water-wet capillary tube and the interface between the fluids is curved. Because the tube has an affinity to water the water is pulled up the walls of the tube.

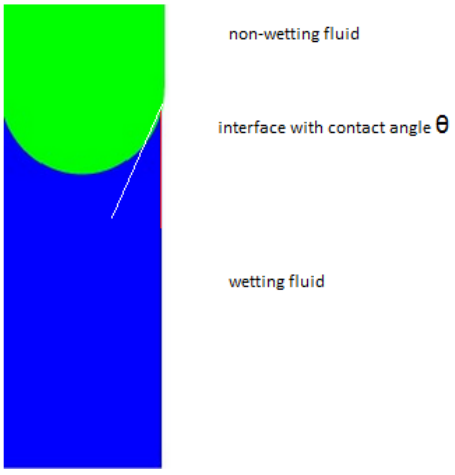


**Figure 1-7. Illustration of a water-wet capillary tube with a water phase and a gas phase.**

For calculation of the capillary pressure, $P_c$, across the interface between two immiscible liquids, the Laplace equation can be used:

$$P_C = P_{nw} - P_w = \sigma\left(\frac{1}{r_1} + \frac{1}{r_2}\right) \quad (1.1)$$

Here, $P_{nw}$ is the non-wetting phase pressure and $P_w$ is the wetting phase pressure, $\sigma$ is the interfacial tension and $r_1$ and $r_2$ is the principal radii of the curvature of the interface. If $\sigma$ is zero, the fluids are miscible (Pentland, 2010). If $r_1 = r_2$ an equation showing that the capillary pressure is mainly dependent on pore channel radius can be written:

$$P_C = \frac{2\sigma \cdot \cos\theta}{r} \quad (1.2)$$

where $\theta$ is the contact angle between the fluids and $r$ is the radius of the pore throat being filled. In imbibition, the wetting phase fills the narrowest pores or throats first, in decreasing order of capillary pressure (Pentland, 2010). The number of throats connected to a pore is known as the coordination number ($N_{coord.}$). Large coordination numbers tend to lead to less trapping because of more paths for the non-wetting fluid to be displaced.

Figure 1-8 shows the inverse relationship between capillary pressure and wetting phase saturation. These capillary pressure curves show, in this case, an immiscible, water-wet system with water and $CO_2$. This is a similar system to what is used in the experiments in this thesis.

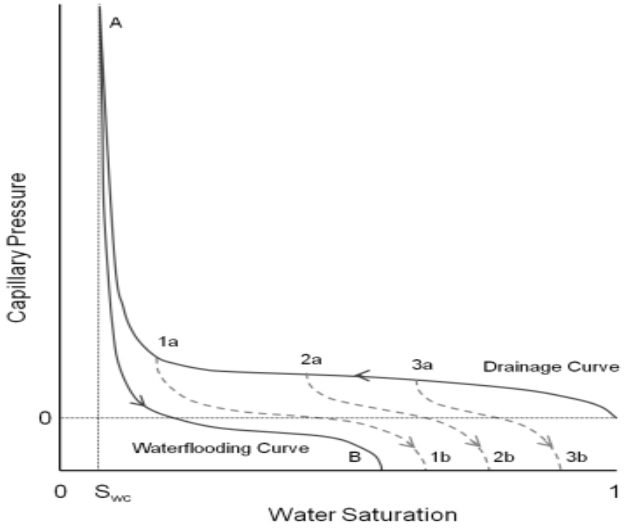


**Figure 1-8. Capillary pressure curves for drainage and imbibition (waterflooding) for a water-wet system with water and $CO_2$. The solid curves represent the maximum saturation changes that happen in a system with the largest possible applied positive or negative capillary pressures. The bounding curves define the connate water saturation (Swc, point A) and the maximum residual saturation of the non-wetting phase (point B). If a smaller positive capillary pressure is applied prior to waterflooding then scanning curves (dashed lines; 1a-1b, 2a-2b, 3a-3b) can be plotted in-between the bounding curves. (Pentland, 2010).**

### 1.4.3. Solubility trapping

Solubility trapping is a process where $CO_2$ dissolves in formation water, leading to only one phase and eliminating the buoyant forces that would otherwise drive $CO_2$ upwards. More $CO_2$ can dissolve in formation water at low temperatures and salinities, than at high temperatures and salinities (Intergovernmental Panel on Climate Change, 2005). Brine saturated with $CO_2$ is denser than regular brine and it will therefore migrate downwards, aiding in mixing brine and $CO_2$ and thus helping the dissolution process (Pentland, 2010). When some of the injected $CO_2$ dissolves in the formation water, less of it will migrate towards the caprock and the risk of leakage is thus smaller. Temperature is more significant than pressure to $CO_2$ solubility in brine. As seen in Figure 1-9 around 4g of $CO_2$ per 100g of $CO_2$ can dissolve per 100g of brine at 50˚C and 10MPa pressure. This was important data for the experiments conducted at Haukeland University Hospital for this thesis when making live fluids; brine saturated with $CO_2$ and $CO_2$ saturated with brine.

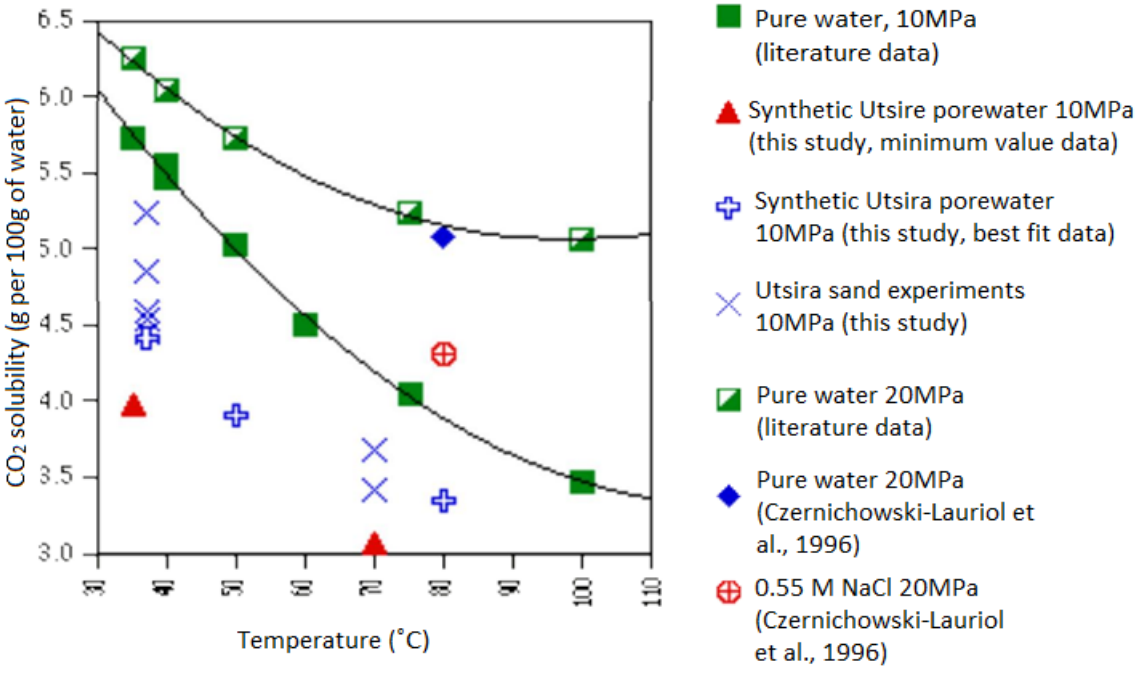


**Figure 1-9. Comparison of $CO_2$ solubility in pure water, synthetic Utsira pore water, Utsira sand experiments water and brine at different pressures plotted against temperature (Rochelle, 2002).**

The amount of brine that is soluble in $CO_2$ is much lower than the amount of $CO_2$ that is soluble in brine, as seen in Figure 1-10. Using these data the amount of brine soluble in $CO_2$ was calculated and mixed. This will be discussed further in section **4.2**.

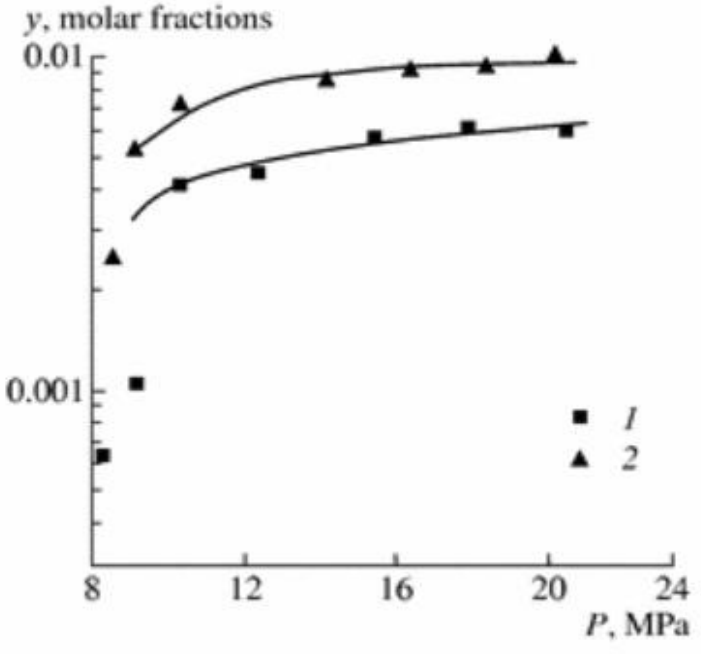


**Figure 1-10. The solubility of water in supercritical carbon dioxide: (1) 313K and (2) 323K. The solid lines indicate calculation. (Sabirzyanov et al., 2000)**

### 1.4.4. Mineral trapping

Mineral trapping can occur when $CO_2$ is dissolved in formation water and after a long time converts to stable carbonate minerals after a series of geochemical, chemical equilibrium, mineral dissolution and precipitation reactions. Carbonic acid ($H_2CO_3$) will form upon dissolution of $CO_2$ in formation water. Carbonic acid is unstable and will dissociate to ionic species reacting with the rock, leading to a rise in ph. These ionic species will over time react with the brine and rock and a fraction of it may precipitate as stable carbonate minerals (Intergovernmental Panel on Climate Change, 2005). Mineral trapping relies on the dissolution of other minerals in the aquifer that provide $Ca^{++}$, $Mg^{++}$ and $Fe^{++}$ ions for the conversion (Thibeau et al., 2007). Mineralization of $CO_2$ is probably the safest option for $CO_2$ storage, however, mineralization takes hundreds of thousands of years to yield a large enough quantity of minerals (Nghiem et al., 2010, Intergovernmental Panel on Climate Change, 2005).

## 1.5. Industrial-scale storage projects

This section will mention three of the biggest industrial-scale storage projects in the world: the Sleipner project in an offshore saline formation in Norway, the Weyburn EOR project in Canada and the In Salah project in a gas field in Algeria. The two most significant of these, in terms of cumulative volume injected and experience of $CO_2$ storage, are Sleipner and In Salah. These fields have been in operation for 13 and 5 years, respectively (Wright et al., 2009).

### 1.5.1. The Sleipner project

The Sleipner project was set in motion due to the 1991 introduction of the Norwegian offshore $CO_2$ tax of around 50$/ton. The project has passed break even due to the avoidance of this tax (Wright et al., 2009).

The Sleipner field injects $CO_2$ in the Utsira Formation (800-1100m below sea level) which is a saline aquifer. $CO_2$ is injected over a 38m interval and a shallow long-reach highly deviated well at 1012m depth is used to take the $CO_2$ 2.4km away from the producing wells and platform area (to avoid erosion) (Wright et al., 2009, Singh et al., 2010). The reservoir is of high quality with an average porosity of 36% and a permeability range of 1 to 5 Darcy and is mainly sandstone with a number of thin shale layers (Singh et al., 2010). The pressure and temperature conditions, as well as the porosity and permeability, at the Sleipner site (37˚C and 100bar at the injection point) are fairly similar to the experimental conditions in the $CO_2$-brine displacements conducted at Haukeland University Hospital for this thesis (25-50˚C and 90-100bar).

Injection started in 1996 and an essentially linear injection rate has taken place since then, leading to around 11Mt of accumulated $CO_2$ injected as of 2008 (Wright et al., 2009). In comparison, the Norwegian domestic greenhouse gas emissions were 52,7Mt of $CO_2$ equivalents in 2012 (Statistics Norway, 2014). A recent report released by The Norwegian Petroleum Directorate states that the Utsira Formation and the underlying Skade Formation has a theoretical storage capacity of 15.77Gt (Halland et al., 2014).

Figure 1-11 shows six time-lapse seismic data surveys that show regular expansion of the $CO_2$ plume. The Utsira Formation has nine silt strings and these multiple layers have resulted in much better storage efficiency than in a purely homogeneous unit, although maximum growth of the $CO_2$ plume now occurs in the uppermost layer (Wright et al., 2009).

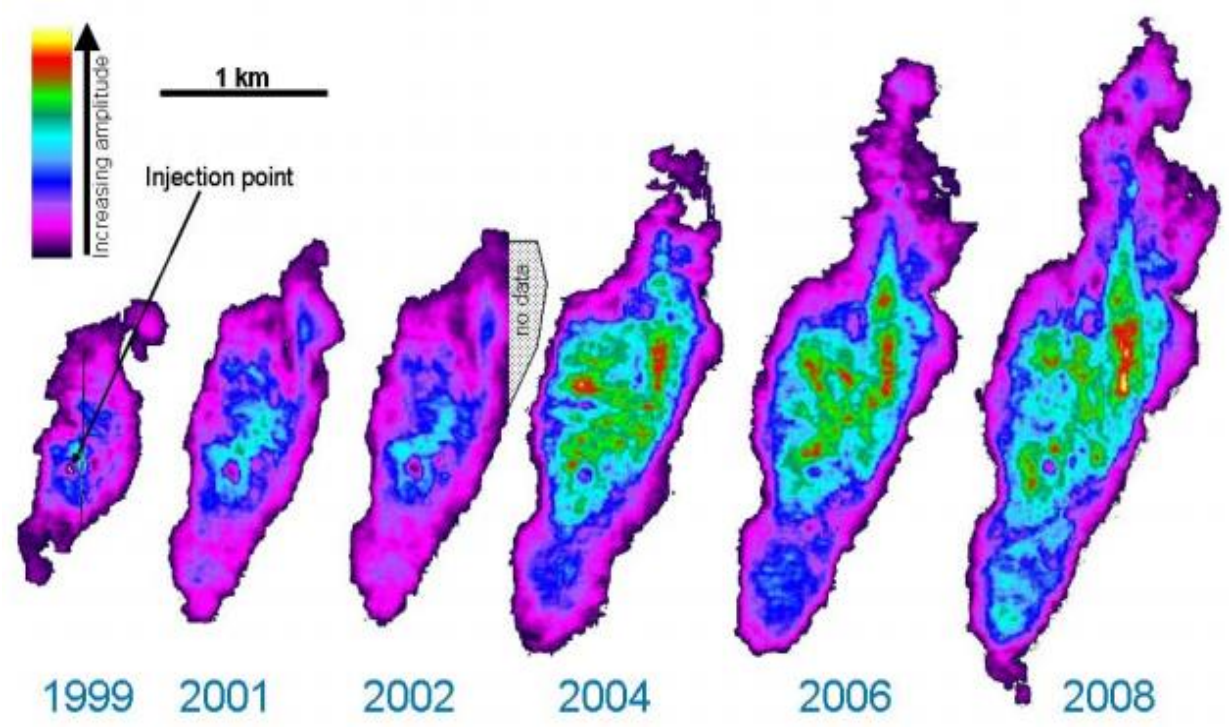


**Figure 1-11. Six time-lapse seismic data surveys showing the expansion of the $CO_2$ plume at the Utsira Formation over a 9-year period from 1999 to 2008 (Wright et al., 2009).**

### 1.5.2. In Salah

In Salah Gas (ISG) is a joint venture project that comprises a phased development of eight gas fields located in the Ahnet-Timimoun Basin in the Algerian Central Sahara (Wright et al., 2009). The project processes and strips gas from the Krechba Field (containing up to 10% $CO_2$) and reinjects it into a sandstone reservoir at a depth of 1800m, storing up to 1.2Mt$CO_2$/yr. Horizontal injection wells (up to 1.5km) are used to inject $CO_2$ into the 5mD reservoir, much less permeable than in the Sleipner project (Intergovernmental Panel on Climate Change, 2005).

The Krechba Field is an anticline with a top seal of 950m of mudstones. A preliminary risk assessment of the $CO_2$ storage integrity as well as extensive monitoring has been applied. Figure 1-12 shows a schematic of the In Salah Project, including production and injection wells. It is expected that the injected $CO_2$ will eventually migrate into the area of the current gas field after depletion of the gas zone. (Intergovernmental Panel on Climate Change, 2005).

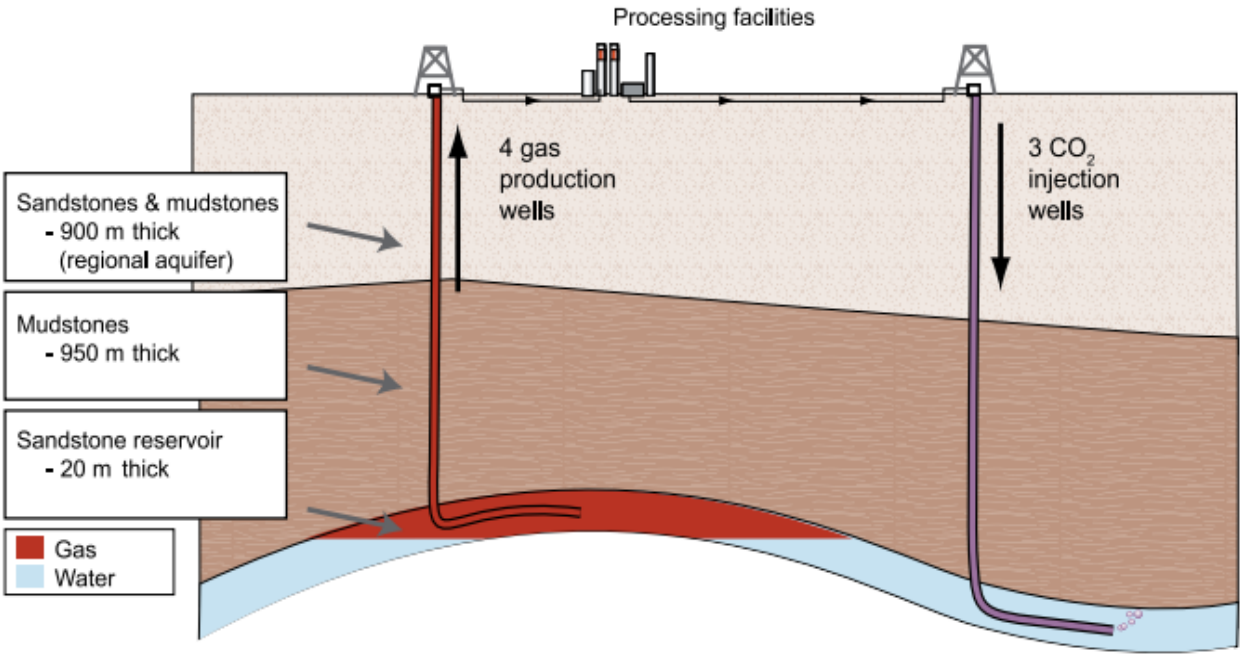


**Figure 1-12. Schematic illustration of the In Salah Gas Project, Algeria. One $MtCO_2$/yr will be stored in the gas reservoir. Long-reach horizontal wells with slotted intervals of up to 1.5 km are injecting $CO_2$ into the water-filled parts of the gas reservoir (Intergovernmental Panel on Climate Change, 2005).**

### 1.5.3. The Weyburn $CO_2$-EOR Project

The Weyburn $CO_2$-enhanced oil recovery ($CO_2$-EOR) project began $CO_2$ injection in late 2000 and has an expected lifetime of 20-25 years. It is located in the Williston Basin, a geological structure extending from south-central Canada into north-central United States. The aim of the project is to permanently store nearly all of the injected $CO_2$, thus eliminating the $CO_2$ that would normally be released at the end of the field life (Intergovernmental Panel on Climate Change, 2005).

The $CO_2$ for the Weyburn $CO_2$-EOR project is dehydrated and compressed 325km south of Weyburn at a gasification plant in Beulah, North Dakota, USA, that gasifies coal to make synthetic methane. This gives off a relatively pure stream of $CO_2$ as a byproduct. The $CO_2$ is then piped to Weyburn in southeastern Saskatchewan, Canada, for use in the field. This piping is designed to go on for 15 years with delivered $CO_2$ volumes dropping from 5000 to about 3000 t/day, or approximately 20Mt of $CO_2$ in total. The compressed $CO_2$ is injected into the oilfield in alternating slugs with water, also known as water-alternating-gas or WAG (Intergovernmental Panel on Climate Change, 2005, Condor et al., 2010).

The oil reservoir at the Weyburn field is a fractured carbonate with a thickness of 20-27m. The basal and primary seals consist of anhydrite and a thick, flat-lying shale rock above a regional unconformity also

forms a good barrier. The field is designed to optimize the sweep efficiency of the $CO_2$ for EOR-purposes by drilling a combination of vertical and horizontal wells (Intergovernmental Panel on Climate Change, 2005).

All of the produced $CO_2$, along with some water, are transported to surface facilities where it is separated, compressed and reinjected into the reservoir production zone (Intergovernmental Panel on Climate Change, 2005, Condor et al., 2010). Extensive monitoring is applied to determine any potential leakage (Intergovernmental Panel on Climate Change, 2005).

# 2. Fundamentals and $CO_2$ storage potential of Natural Gas Hydrates

Natural gas hydrates (NGH) are ice-like, solid compounds that consist of water and another hydrate former, often referred to as the guest molecule. Water interconnects through hydrogen bonding and form cages or cavities that can host small non-polar or slightly polar guests. Common guest molecules are methane, ethane, propane and carbon dioxide. These guest molecules are captured in cavities in a crystalline water structure and help stabilize the structure. Hydrates may form at high pressures and low temperatures and there are vast amounts found in nature, mostly methane hydrates (Hester, 2009). This chapter will provide fundamentals of natural gas hydrates. The main reference used in this chapter is the book "Clathrate Hydrates of Natural Gases" by E. Dendy Sloan and Carolyn A. Koh (Sloan and Koh, 2008) and it is recommended for further reading. Hydrates are a fairly unconventional subject and the fundamentals is therefore presented in a comprehensive way in this thesis although technical difficulties lead to only one $CO_2$-$CH_4$ exchange experiment being conducted.

Water is the main component in gas hydrates due to its special properties, the most important of which its ability to form hydrogen bonds. Water, while melting at 0° C and boiling at 100° C, is at its most dense between 0° and 4° C, which results in water expanding upon freezing.

The water molecule consists of two hydrogen atoms (H) and one oxygen atom (O) covalently bound together in an H-O-H structure with an angle of 104.5°. The oxygen atom has eight electrons; with the electronic configuration $1s^2 2s^2 2p^4$, and the hydrogen atoms has the electronic configuration $1s^1$. The electrons in the hydrogen atoms are shared with two bonding electrons of oxygen. The water molecule has four charges and a permanent electric dipole. This is because the shared electrons with the protons give the molecule two positive charges and the lone pair electrons give the molecule two negative charges. Figure 2-1 shows how the molecules bond.

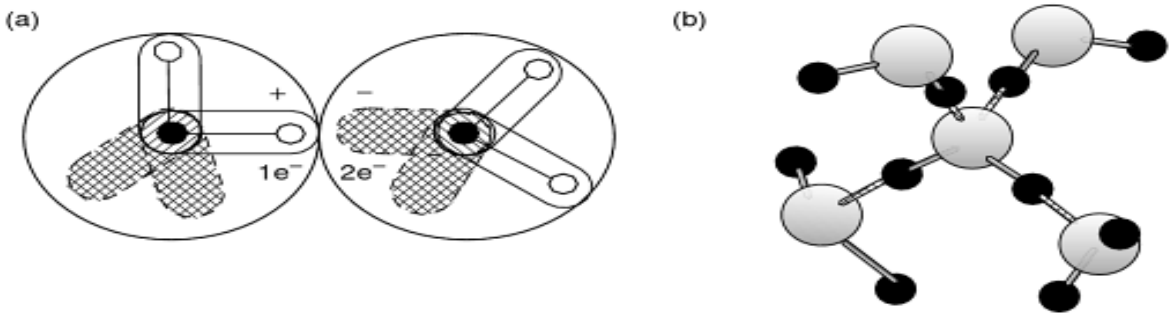


**Figure 2-1. Hydrogen bonding of water molecules. (a) between two water molecules. (b) between four water molecules (Sloan and Koh, 2008).**

## 2.1. Natural Gas

Methane, ethane and propane are all hydrocarbons covered by the term “natural gases” and they are of interest to the industry because of their energy potential. Carbon dioxide and nitrogen are examples of other natural gases that are less valuable. This thesis will examine the storage of carbon dioxide ($CO_2$) in hydrates. The reason for injecting $CO_2$ in methane hydrate reservoirs is that $CO_2$ is a more thermodynamically stable hydrate former than methane ($CH_4$), hence a spontaneous exchange of guest molecules will happen in the hydrates and methane can be produced while $CO_2$ is stored (Ersland et al., 2010, Graue et al., 2006a, Komai et al., 2000).

Methane is a colorless gas, which melts at -182.5° C and boils at -164° C and will be in gas phase at the temperatures and pressures used in the experimental work done in this thesis (Daintith, 2010).

Carbon dioxide ($CO_2$) is a molecule consisting of one carbon atom and two oxygen atoms in a linear structure. $CO_2$ in gas phase has a slightly irritating odor, is colorless and is denser than air. Under normal conditions $CO_2$ is a gas, but at temperatures higher than 31.1° C and pressures higher than 73.9 bar $CO_2$ is said to be in a supercritical state (see Figure 2-2). In this state it behaves as a gas, but the density can exceed the density of liquid water. $CO_2$ is soluble in water and the resulting solution has a higher density than pure water. In the temperature and pressure regimes in the experiments conducted in this thesis, $CO_2$ will be in liquid phase and supercritical state.

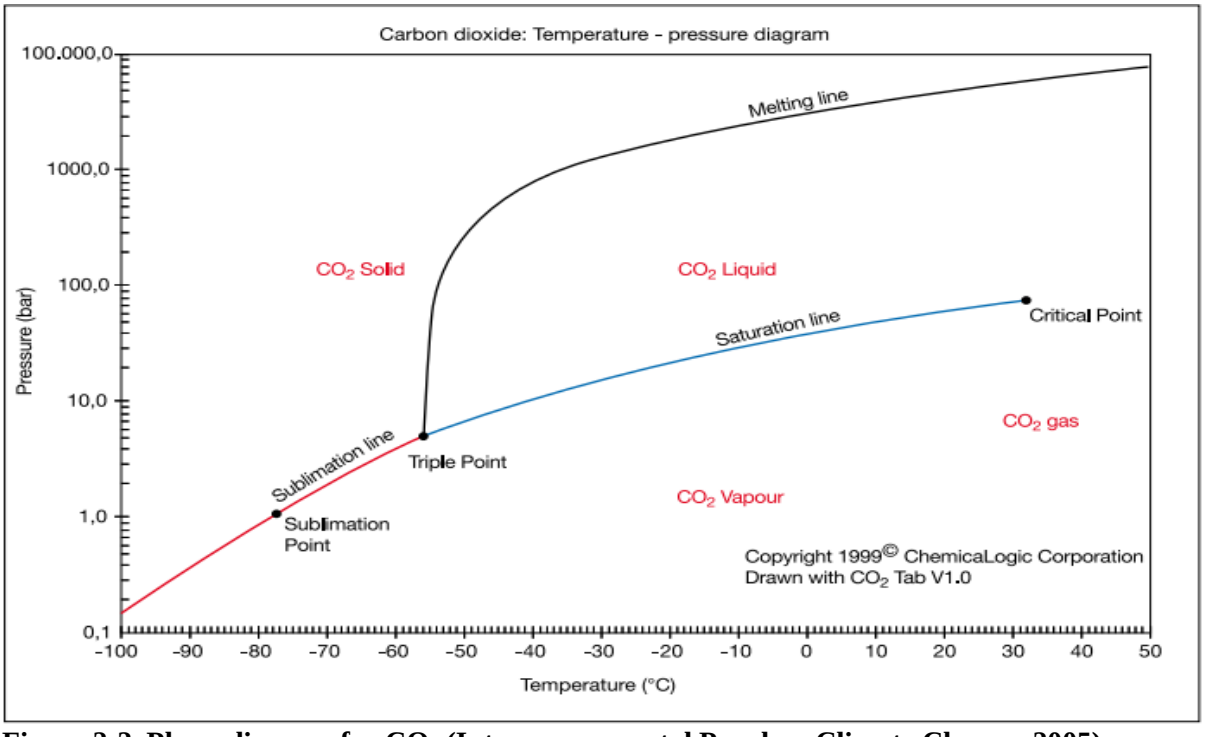


**Figure 2-2. Phase diagram for $CO_2$ (Intergovernmental Panel on Climate Change, 2005).**

## 2.2. Hydrate structures

Hydrates are crystalline, ice-like compounds and can form three different crystal structures: cubic structure I (sI), cubic structure II (sII), or hexagonal structure H (sH). The major difference from ice is that hydrates only form in the presence of a guest molecule of proper size, whereas ice is a pure compound. Typical proper sized molecules for structure I is methane, ethane, carbon dioxide and hydrogen sulfide. These molecules have diameters between 4.2 and 6 Å, whereas smaller molecules, such as nitrogen and hydrogen, form structure II. Molecules with a diameter between 6 and 7 Å, such as propane and iso-butane, will also form structure II. For structure H, molecules with diameters of typically 7-9 Å in addition to smaller molecules such as methane, are needed as guests. Figure 2-3 shows the crystal unit structures discussed here (Sloan and Koh, 2008).

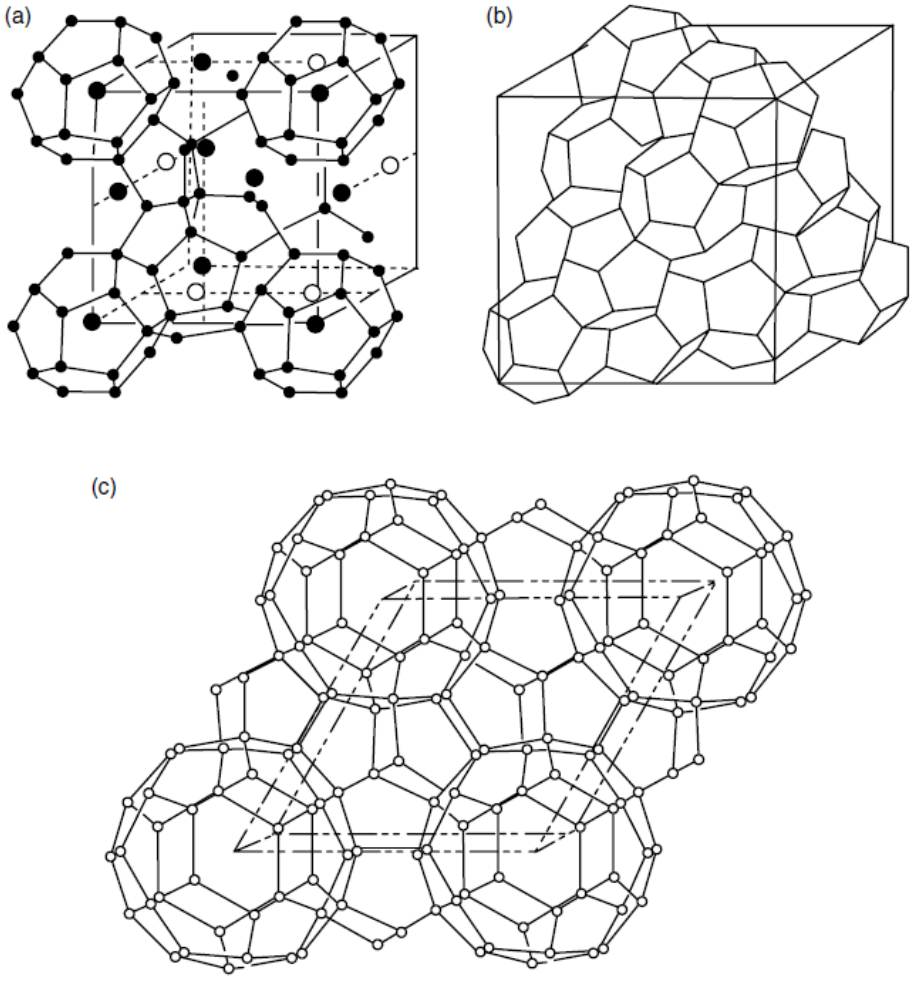


**Figure 2-3. Crystal unit structures: (a) sI-hydrate, (b) sII-hydrate, (c) sH-hydrate (Sloan and Koh, 2008).**

Structure I and structure II are found in nature and therefore is of more interest than structure H. In the experiments conducted in this thesis the structure present is structure I. Structure I consists of two pentagonal dodecahedrons ($5^{12}$) and six tetrakaidecahedron ($5^{12}6^2$). The pentagonal dodecahedron is labeled $5^{12}$ because it has 12 equal pentagonal faces and the tetrakaidecahedron is labeled $5^{12}6^2$ because it has 12 pentagonal and 2 hexagonal faces. Structure I hydrate is unique because it can form from only small guests such as methane or carbon dioxide and is therefore suitable for $CO_2$-$CH_4$ exchange. Structure II hydrate consists of sixteen pentagonal dodecahedron ($5^{12}$) and eight hexakaidecahedral ($5^{12}6^4$). Both structure I and structure II has two different cages, whereas structure H has three different cages (Sloan and Koh, 2008).

## 2.3. Cavities and guest molecules

Inside the hydrate structures there are cavities where hydrophobic guest molecules can be captured. These cavities consist mostly of pentagonal and hexagonal faces. To stabilize the hydrate structures it is necessary to fill most of the cavities with molecules which do not compete or interfere with the hydrogen bonding of the clathrate water structure. It needs to be a molecule with the proper dimensions to fit within the voids "van der Waals-wise" and without strong hydrophilic properties (Jeffrey, 1984). The guest molecule should not have too strong a polarity as it may break the hydrogen bonds forming the cavity. Methanol is an example of such a substance and it has been used as a hydrate inhibitor as well as for hydrate dissociation (Sira, 1990). The cages for the different structures are shown in Figure 2-4.

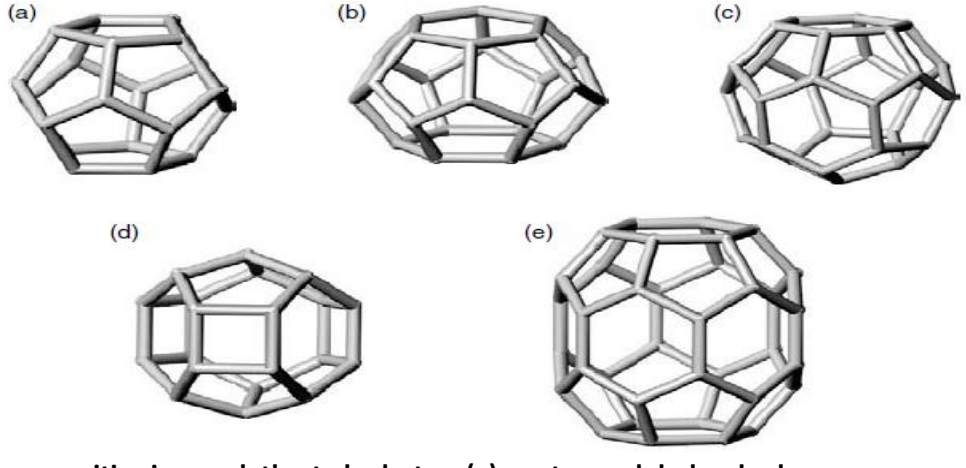


**Figure 2-4. Three cavities in gas clathrate hydrates: (a) pentagonal dodecahedron ($5^{12}$), (b) tetrakaidecahedron ($5^{12}6^2$), (c) hexakaidecahedron ($5^{12}6^4$), (d) irregular dodecahedron ($4^3 5^6 6^3$), and (e) icosahedron ($5^{12}6^8$) (Sloan and Koh, 2008).**

Pentagonal dodecahedron ($5^{12}$) is the smallest cavity and is included in the three structures mentioned in this thesis. 20 molecules are needed to make the pentagonal dodecahedron cavity. Tetrakaidecahedron ($5^{12}6^2$) has the most important role in stabilizing structure I hydrates and can fit guests with diameters less than 6 Å. Hexakaidecahedron ($5^{12}6^4$) can host guests with a diameter of up to 6.6 Å (Sloan and Koh, 2008). In Table 2-1 some properties of structure I and structure II can be seen.

**Table 2-1. Important properties of structure I and II.**

| Hydrate crystal structure | I | | II | |
|---|---|---|---|---|
| Cavity | **Small** | **Large** | **Small** | **Large** |
| **Description** | $5^{12}$ | $5^{12}6^2$ | $5^{12}$ | $5^{12}6^4$ |
| **Number of cavities/unit cell** | 2 | 6 | 16 | 8 |
| **Average cavity radius (Å)** | 3.95 | 4.33 | 3.91 | 4.73 |

The ratio between the diameter of the guest molecules and the diameter of the cavities must be in the right range. If it is too low, the guest will not stabilize the cavity, and if it is too high it will not fit in the cavity. A size ratio lower bound of 0.76 has been suggested (Sloan and Koh, 2008).

Methane is a tetrahedral molecule consisting of a single carbon and four hydrogen atoms with covalent bonds. It is the most common guest for hydrates found in nature and is also the most common component in natural occurring hydrocarbon gas. Table 2-2 shows diameter and ratio between molecular diameter and cavity diameter in the three relevant guest molecules used in in-house hydrate experiments at UoB.

**Table 2-2. Ratio of molecular diameters to cavity diameters for some gas hydrate formers (Sloan and Koh, 2008).**

| | | Molecular diameter/cavity diameter for cavity type | | | |
|---|---|---|---|---|---|
| Guest hydrate former | | **Structure I** | | **Structure II** | |
| Molecule | **Diameter (Å)** | $\mathbf{5^{12}}$ | $\mathbf{5^{12}6^2}$ | $\mathbf{5^{12}}$ | $\mathbf{5^{12}6^4}$ |
| **Nitrogen** | 4.1 | 0.804 | 0.700 | 0.817 | 0.616 |
| **Methane** | 4.36 | 0.855 | 0.744 | 0.868 | 0.655 |
| **Carbon dioxide** | 5.12 | 1.00 | 0.834 | 1.02 | 0.769 |

## 2.4. Hydrate thermodynamics and kinetics

Hydrates are stable in and form under conditions where the temperature is low and the pressure is high. The concentration of hydrate former is also a factor. In Figure 2-5 the correlation of the pressures and temperatures where hydrate is stable is shown. If the conditions are on the right side of the hydrate equilibrium line (AB), hydrate will not form, or it will melt. A thermodynamic driving force is required for hydrate to be formed. If the temperature is lowered and/or the pressure increased so that the metastable or labile region is entered, hydrate can form. The molecular concentration can also be increased to achieve this and different guest molecules also require different pressures to form hydrate (Sloan and Koh, 2008).

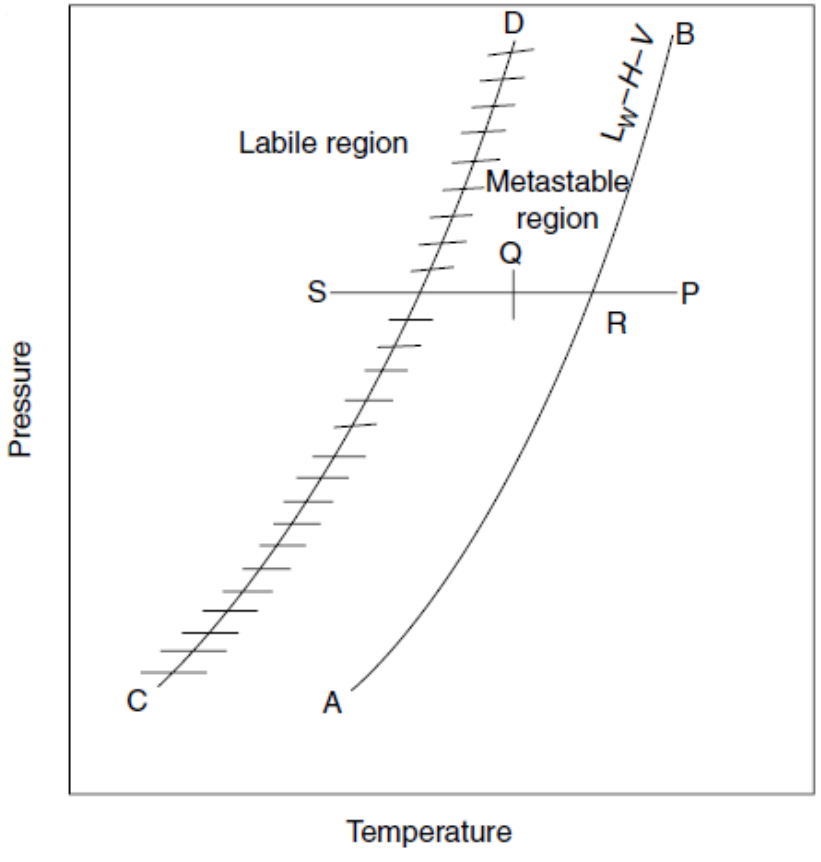


**Figure 2-5. Hydrate formation conditions. Hydrate cannot form, and will melt, in the stable zone to the right of equllibrium line AB. In the metastable region (between AB and CD) spontaneous crystallization is improbable. However, if a crystal seed were placed in such a metastable solution, growth would occur on it. The unstable or labile (supersaturated) zone (to the left of CD) is where spontaneous crystallization occurs.**

When hydrates form, the first thing that happens is the formation of crystal nuclei that are not visible to macroscopic probes. The time it takes until there is a detectable amount of hydrate phase or until there is a detectable number of moles of hydrate former gas consumed, is called the induction time. After this initial induction period, a period of rapid growth occurs. Eventually the water is consumed by hydrate formation and the slope of gas consumption flattens. This is shown in Figure 2-6 below, which is an example of a laboratory experiment with the same logging method used in the experimental work in this thesis.

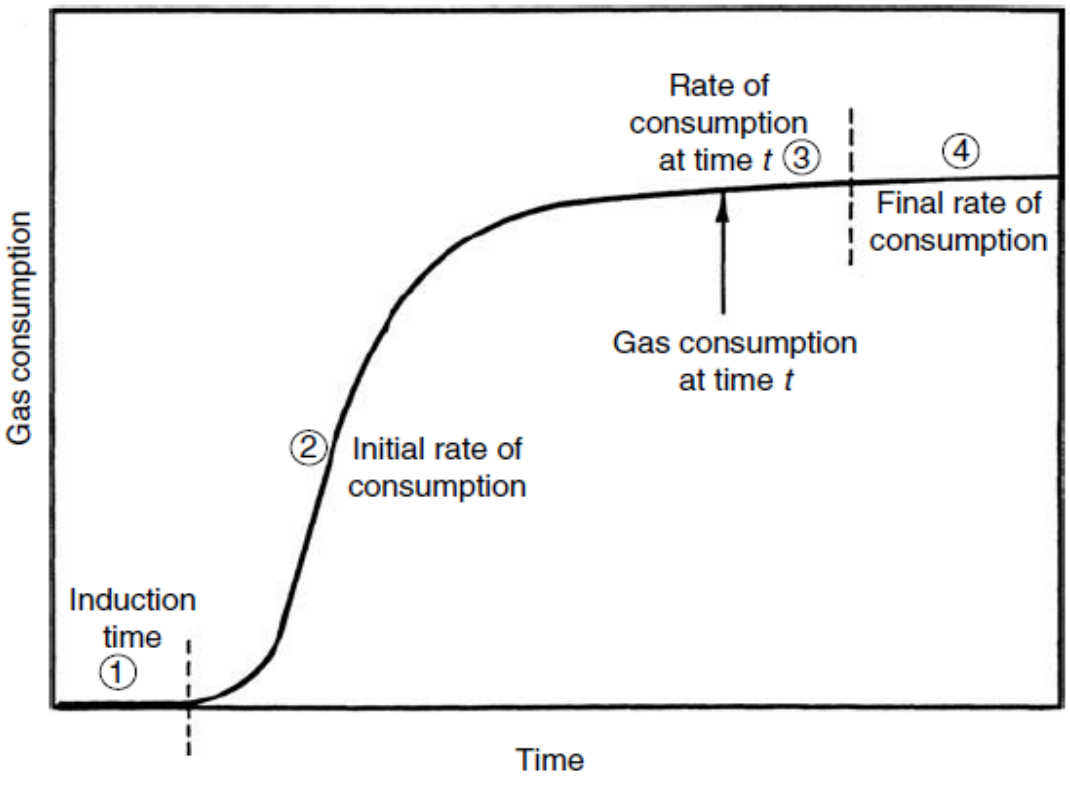


**Figure 2-6. Gas consumption vs time for hydrate formation (Sloan and Koh, 2008).**

After a critical radius of a cluster of molecules is reached, monotonic growth occurs. This phenomenon of spontaneous growth can be explained by the excess Gibbs free energy (ΔG) between a small solid particle of solute and the solute in solution. ΔG is the sum of the surface excess free energy ΔGS (for solute molecules becoming part of the surface of the crystal nuclei), and the volume excess free energy ΔGV (for solute molecules ending up in the bulk/interior of the crystal nuclei) (Sloan and Koh, 2008). As seen in Figure 2-7, the critical Gibbs free energy needs to be exceeded in order to reach spontaneous growth of nuclei/clusters.

Hydrate dissociation is another important aspect in natural gas production from methane hydrates as well as in industrial flow assurance. The dissociation process is endothermic and will consume heat; hence it is often limited by heat transfer. Dissociation may occur when adding heat, reducing pressure or by injecting an inhibitor.

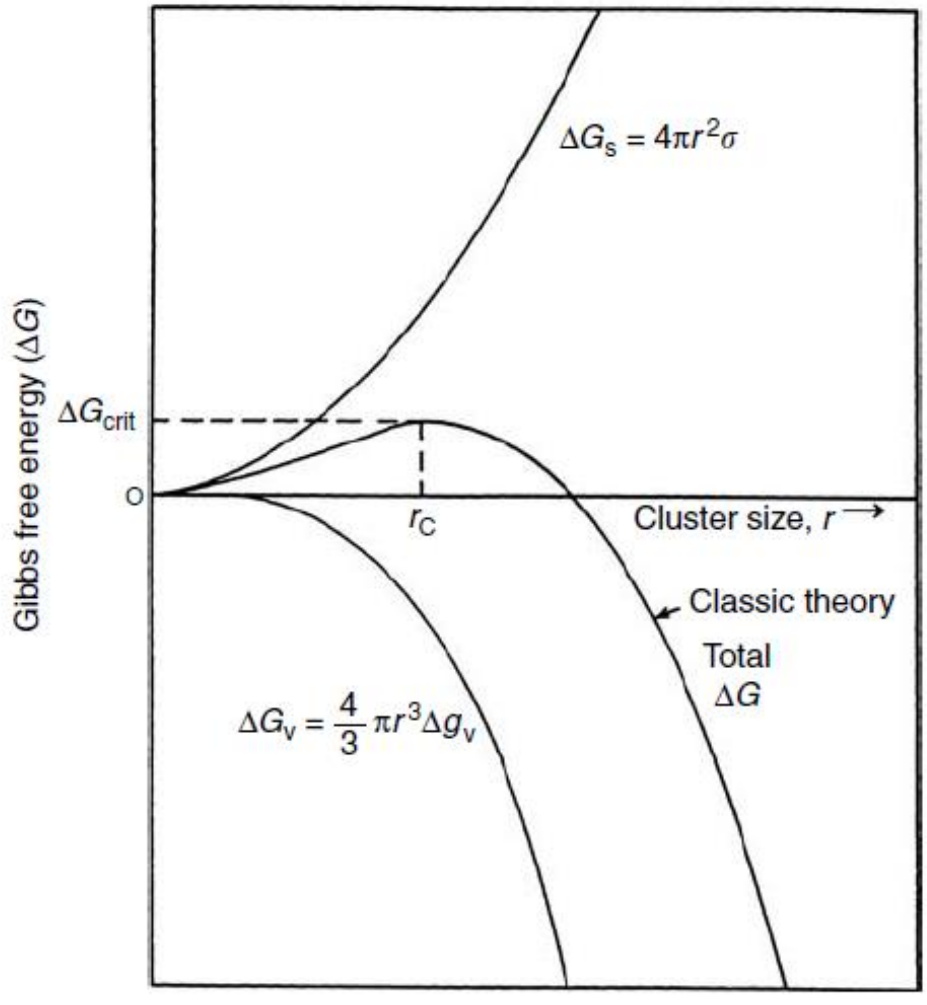


**Figure 2-7. Comparison of surface excess free energy ($\Delta G_S$) and volume excess free energy ($\Delta G_V$) as functions of cluster size (Sloan and Koh, 2008).**

## 2.5. Hydrates in nature

Artificial formation of hydrates in laboratory studies was observed around 1800, but in 1965 Makogon announced the discovery of *in situ* hydrates in the permafrost regions of the Soviet Union. Hydrates appear to be ubiquitous in nature and are likely to form wherever methane and water are present at hydrate thermobaric conditions, thus they have existed for millions of years (Sloan and Koh, 2008). Natural gas hydrates are plentiful in nature, but only concentrated sources are useful as a possible energy source. Just the terrestrial hydrate deposits resource is equivalent to 12000 years of current annual world natural gas consumption, and the oceanic gas hydrate deposits are at least two orders of magnitude larger (Wang and Economides, 2011).

### 2.5.1. Hydrate resources

The estimates of *in situ* natural gas hydrates deposits worldwide vary between $10^{14}m^3$ and $10^{18}m^3$ according to Sloan and Koh (2008). These are large quantities, knowing that the energy consumption of the United States for 1000 years at the current rate is $10^{15}m^3$. Kvenvolden (1988) indicated that even the lower limit estimates of the hydrate resources of the planet are twice that of the equivalent amount of energy of all fossil fuel deposits in total. If only a fraction of the methane in these estimates is recoverable, hydrates could play an enormous role for the energy sector.

Gas hydrates on earth are located mostly at the continental margins of the oceans and in areas with continuous permafrost. In these areas the earth is cold, giving the temperature and pressure conditions for hydrates to form and remain stable. These areas are called the Hydrate Formation Zone (HFZ) and can reach a thickness of 400 to 800m in permafrost regions (Makogon, 2010). Figure 2-8 shows a map of the discovered gas hydrate deposits. Information about the distribution of gas hydrates in continental margin sediment has been gathered mostly from BSR (bottom-stimulating reflector), which is a seismic reflection at the sediment to clathrate stability zone interface caused by density differences (Mosher et al., 2005).

Figure 2-9 shows arbitrary examples of the depths and temperatures where hydrates are stable in permafrost and in oceans. The depth of intersection between the phase boundaries and the geothermal gradients are the lower limit of stability of hydrates and are likely to match with the BSR. Also, the hydrates at this depth are the most easily dissociated due to them being at the phase boundary (Sloan and Koh, 2008). Figure 2-9a shows the methane hydrate stability region bounded by the phase boundary and the geothermal gradient. Here hydrates are stable with only one other phase in excess: in most

cases liquid water with dissolved methane (Sloan and Koh, 2008). In Figure 2-9b the hydrate stability region starts below the seafloor. Hydrates would be unstable above this because they have a lower density than water and the methane concentration in bulk phase seawater is low.

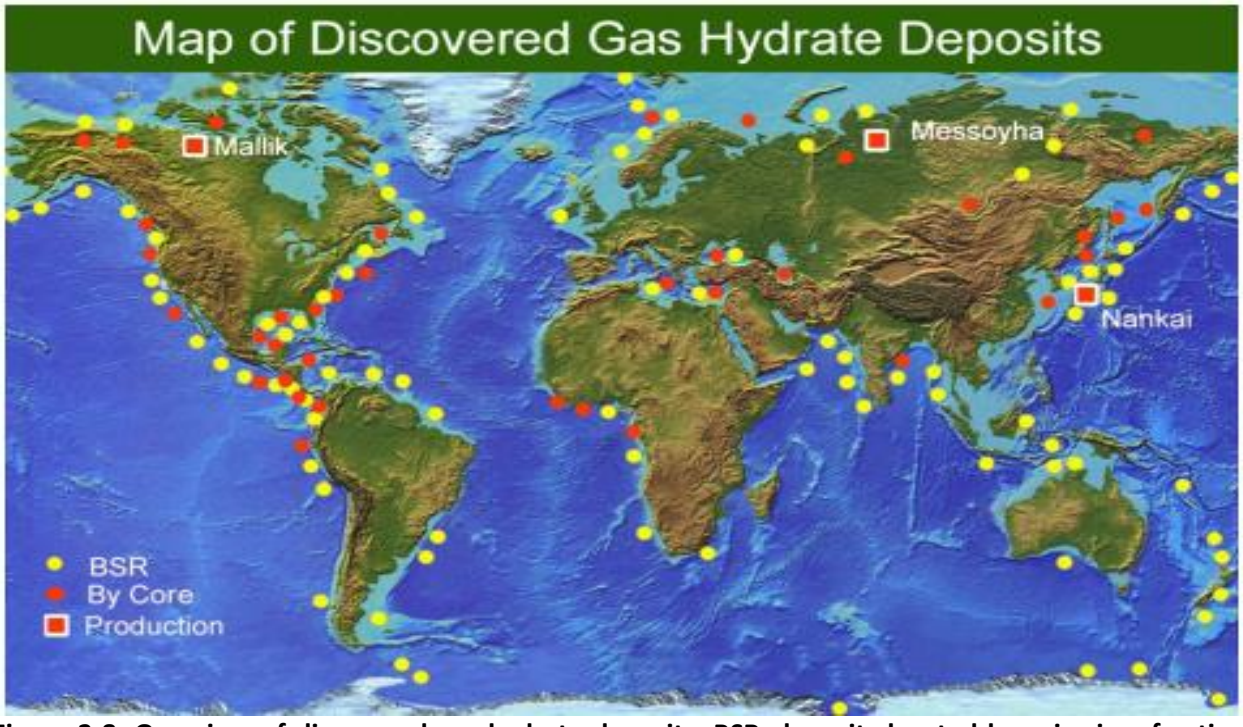


**Figure 2-8. Overview of discovered gas hydrate deposits. BSR=deposits located by seismic refraction (Makogon, 2010).**

In the oceans of the world methane hydrates are stable below around 300-600m of water depth, typically. The gas hydrate stability zone can extend for hundreds of meters below the sea floor, with a general temperature range from 2 to 20˚ C, limited by the availability of methane. In permafrost regions the gas hydrate stability zone normally occurs around 100-300m depth and can extend several hundred meters depending on where the base of permafrost is, with a general temperature range of -10 to 20˚ C (Hester, 2009).

The methane gas that constitutes in the formation of hydrates can be either biogenic or thermogenic. Biogenic methane is formed from anaerobic bacterial decomposition of organic matter and thermogenic methane is formed from thermal cracking of organic material (Hester, 2009).

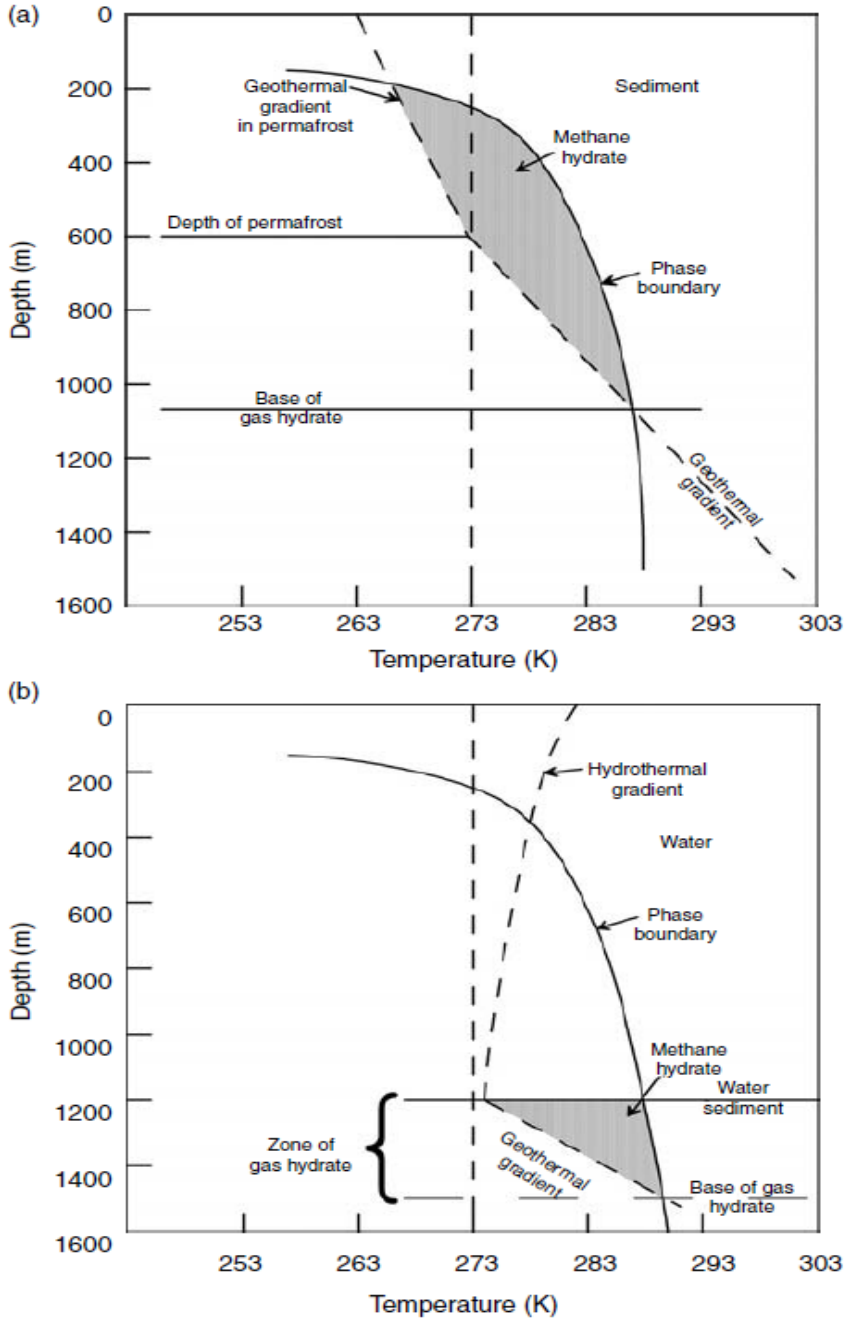


**Figure 2-9. Temperature and depth conditions for methane hydrate stability (a) in permafrost and (b) in marine systems (Sloan and Koh, 2008).**

### 2.5.2. Classification of hydrate resources

While the estimated reserves of natural gas hydrate are vast and several times the size of conventional fossil fuels, there are issues regarding the recoverability of these reserves. Both technical and economic issues have to be taken into consideration. Most of the natural gas hydrate resources are thought to be unlikely for commercial production. Figure 2-10 shows the distribution of hydrate resources in a pyramid shape indicating that the most likely commercial targets for production are not the biggest fraction of the total reserves. At the top of the pyramid are the arctic sandstones under existing infrastructure, followed by arctic sandstones away from existing infrastructure. An example of this kind of reserve, under existing infrastructure, is Ignik Sikumi at the North Slope of Alaska. Below the arctic sandstone reserves are the deep-water sandstones, high-permeable deposits like e.g Gulf of Mexico. Next are low-permeable reserves and at the moment it seems unlikely they will be targeted for methane production, especially considering the existing infrastructures around some arctic sandstones.

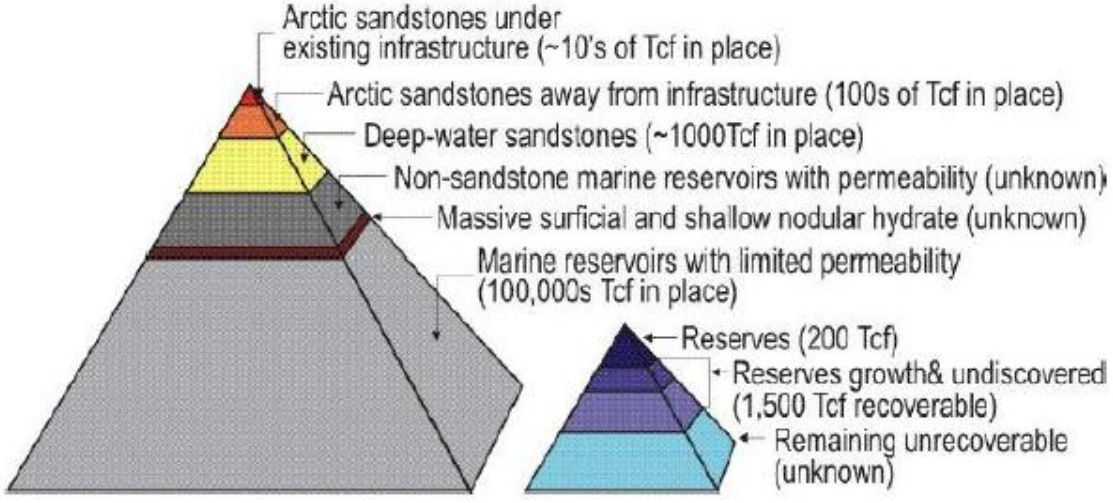


**Figure 2-10. Classification pyramid from (Boswell, 2006).Classification of gas hydrate reserves with respect to their size and relative prospects for future production (left) and conventional gas reserves (right).**

A classification system based on mobile phases present below the hydrate bearing layer (HBL) and the presence of confining strata is shown in Table 2-3. Class 1 hydrate accumulations consist of a hydrate zone and an underlying two-phase fluid zone with free gas. The hydrate interval typically has large hydrate saturations and thus a very low effective permeability. Class 1 hydrates are the most favorable for gas production since only small changes in pressure and temperature are needed in order for dissociation to occur (Moridis and Collett, 2003). Class 2 deposits consist of a hydrate-bearing layer overlying a free water zone (with no free gas). Class 3 deposits consist only of the hydrate-bearing layer and no mobile fluids. Classes 2 and 3 have less defined production potentials than Class 1 and the

desirability is dependent on thermodynamic proximity to hydrate equilibrium, economic and environmental concerns among other issues (Moridis and Collett, 2003). Class 4 and Class 3 deposits are similar except that Class 4 deposits do not have confining strata. Economically viable production from Class 4 deposits is not likely and thus this class of hydrate deposits is not a promising gas production target (Moridis and Sloan, 2006)

**Table 2-3. Classification of different hydrate reservoirs based on mobile phases and the presence of confining strata (Hester, 2009).**

| Deposit type | Zones present | Mobile phases | Confining strata |
|---|---|---|---|
| Class 1 | Two zones: hydrate-bearing layer (HBL) above two-phase zone | Free gas, water | Yes |
| Class 2 | Two zones: HBL above one-phase zone | Water | Yes |
| Class 3 | One zone: HBL | None | Yes |
| Class 4 | One zone: HBL | None | No |

## 2.6. Production methods for natural gas hydrates

This section will cover different schemes for gas production from hydrates in nature. In order to produce gas from hydrates, the hydrates have to dissociate or be introduced to a more thermodynamically stable hydrate former than methane, i.e. carbon dioxide. Possible production schemes include *depressurization, thermal stimulation, thermodynamic inhibitor injection, $CH_4$-$CO_2$ exchange* or a combination of these. Since the focus of this thesis is storage of carbon dioxide, this section will focus mainly on the exchange method. Production methods are worth including in this part due to the fact that it is more likely that $CO_2$ storage in hydrates will be implemented if there is an added bonus aspect of methane production.

### 2.6.1. Production by dissociation

Hydrate dissociation can occur from three different processes: *Depressurization, thermal stimulation* and *inhibitor injection*. *Depressurization* is done by lowering the pressure to a point below the hydrate stability pressure. This is a cost effective method as it does not require large amounts of added energy, but a lot of excess water as well as sand production could cause problems. *Thermal stimulation* is done by increasing the temperature to a point above the hydrate stability temperature. This is an energy demanding method. *Inhibitor injection* will cause the equilibrium line to shift upwards and the hydrate will move out of the hydrate stability region. Inhibitors (i.e. alcohols and salts) are most commonly used in flow assurance to dissociate hydrates and inhibit hydrate growth in pipelines. An illustration of these different methods of hydrate dissociation can be seen in Figure 2-11 from Makogon (1997).

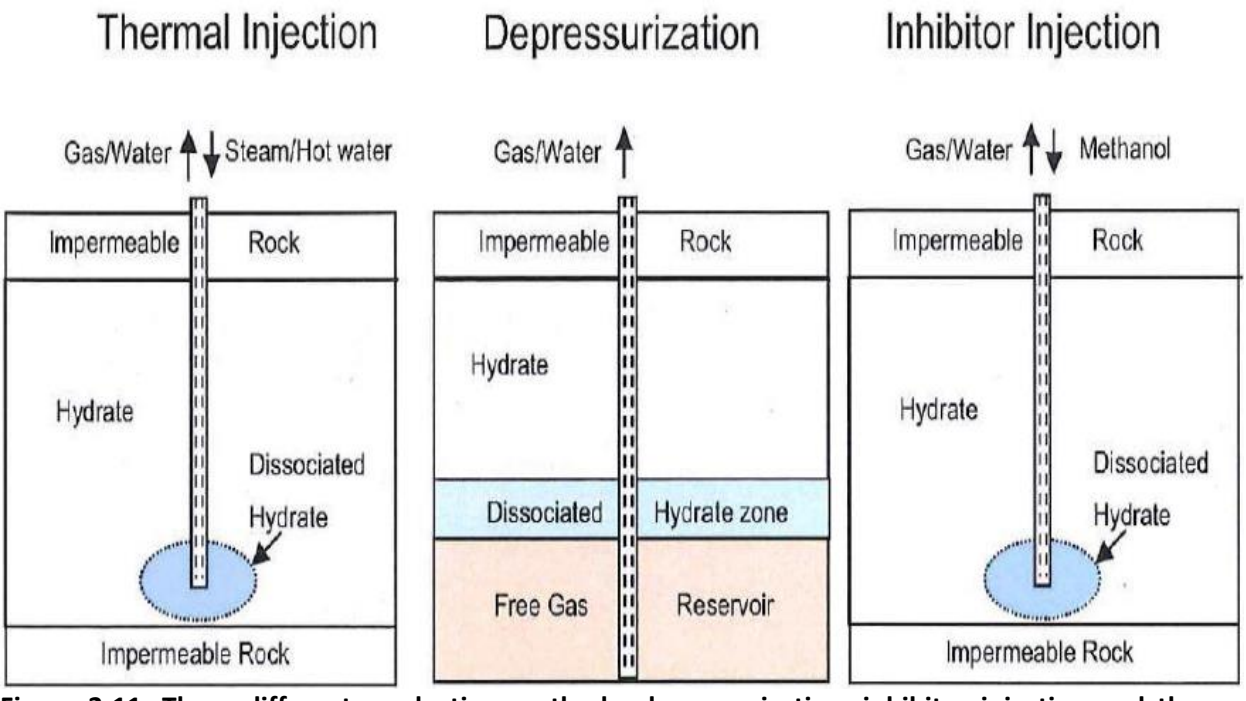


**Figure 2-11. Three different production methods: depressurization, inhibitor injection and thermal stimulation. All are based on dissociation of the present hydrate consequently liberating trapped gas (Makogon, 1997).**

As of today, the only gas hydrate production technique applied is production by dissociation, often as a combination of all three of the techniques listed above. When hydrates dissociate, water will be released and produced and sand may or may not also be produced. Hydrate dissociation is an endothermic process and care must therefore be taken in order to avoid secondary formation of hydrates or ice. Another concern is the geomechanical stability in a dissociation setting; The porosity and permeability of the reservoir zone may change and the integrity of the wells may be compromised (Moridis et al., 2009).

### 2.6.2. Production by $CH_4$-$CO_2$ exchange

The most relevant production method for this thesis is production through an exchange process where $CO_2$ takes the place of $CH_4$ in the natural gas hydrates, thus releasing and producing $CH_4$. It is known that $CO_2$ is a more thermodynamically stable guest than $CH_4$ in natural gas hydrates (see Figure 2-12). This exchange process has been shown using magnetic resonance images (MRI) of core plugs where methane has been spontaneously produced with no added heat and no associated water production (Graue et al., 2006a). The exchange rates deeper into gas hydrates (in bulk form, not in porous media) have been found to be slow (McGrail, 2004), but replacement of $CO_2$ gas hydrates could be achieved within a short period 12 hours) in pure samples of $CH_4$ gas hydrate that had been synthesized as solid crystals (Komai

et al., 2000, Komai, 2002). In addition, it has been shown that in porous media the exchange kinetics improved and a more favorable result was seen (Schoderbek et al., 2012).

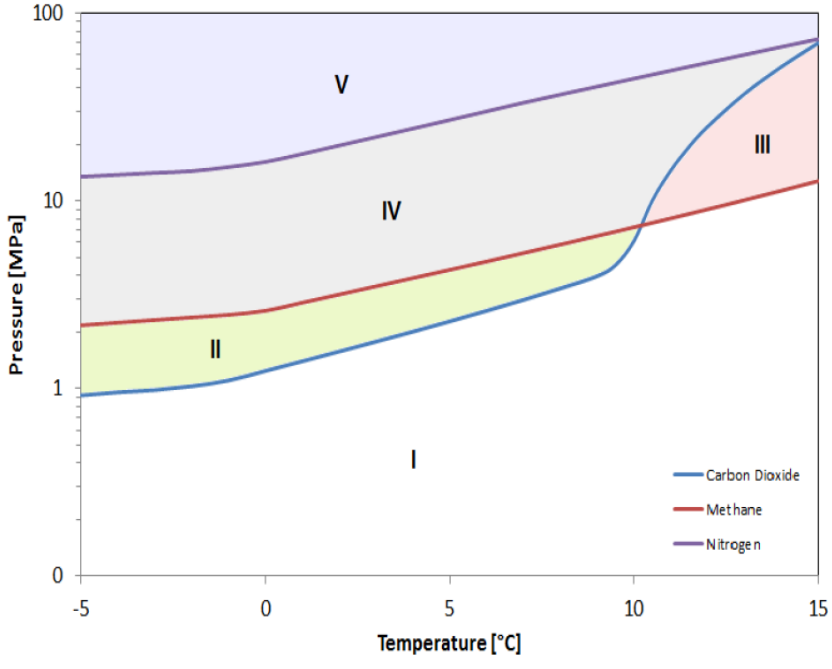


| PT-Area | Hydrate phases |
|---|---|
| I | No hydrate |
| II | $H_{CO2}$ |
| III | $H_{CH4}$ |
| IV | $H_{CO2}$-$H_{CH4}$ |
| V | $H_{CO2}$-$H_{CH4}$-$H_{N2}$ |

**Figure 2-12. Comparison of hydrate equllibrium curves for carbon dioxide, methane and nitrogen as simple hydrates (Hågenvik, 2013). At temperatures below 10˚C the $CO_2$ hydrate is stable at lower pressure values than $CH_4$, making $CO_2$-$CH_4$ exchange possible.**

Figure 2-13 shows a schematic diagram of the guest molecule exchange process in the medium cages and the $CH_4$ reformation in the small cages. The $CO_2$ molecule is too large to occupy the S-cage and thus the $CH_4$ molecule will re-occupy it in order for the structure to remain stable (Ota et al., 2005). The main advantages of this production method are: hydrates will stay intact and geomechanically stable, not producing vast amounts of water and $CO_2$ will be sequestrated. However, the recovery rate is less than by dissociation and large volumes of $CO_2$ are needed.

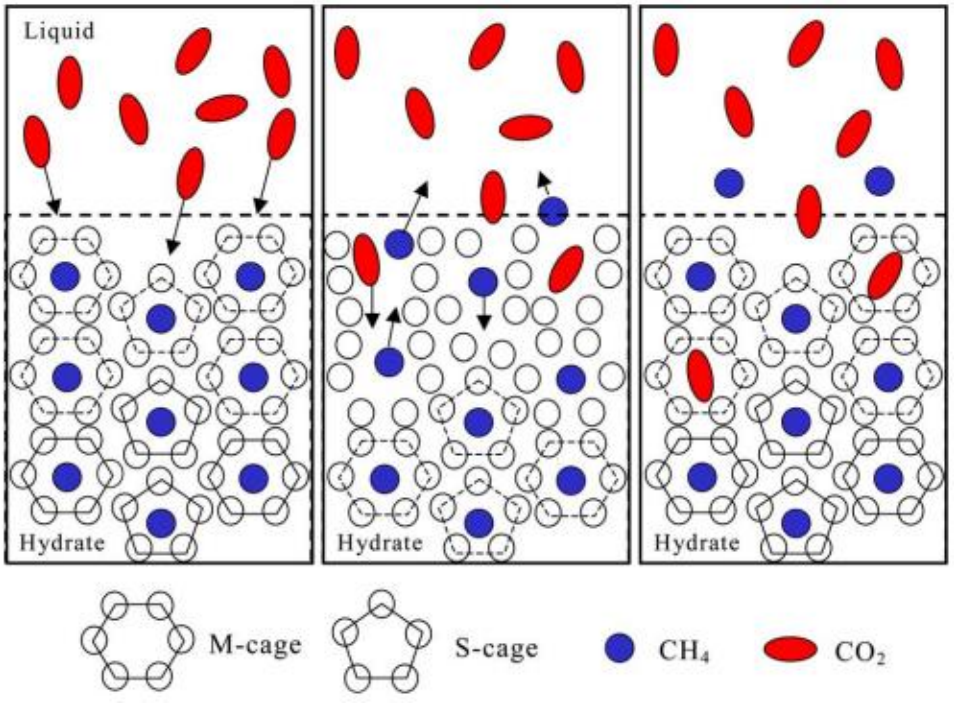


**Figure 2-13. Illustration of carbon dioxide replacing methane as a guest molecule in structure I bulk hydrate. Carbon dioxide is only replacing methane in the large cages (M-cages) and the methane reoccupies the small cages (S-cages) (Ota et al., 2005).**

## 2.7. Natural gas hydrate field studies

This section will give a short overview of three NGH fields that have undergone a production scenario: Messoyakha in Russia, Mallik in Canada and Ignik Sikumi on the north slope of Alaska. Ignik Sikumi is the most significant with respect to this thesis, as it was a pilot test for a $CH_4$-$CO_2$ exchange scenario. All of these projects are in permafrost regions.

### 2.7.1. Messoyakha

The Messoyakha gas hydrate field, located in the northeast of western Siberia, is the first case of gas production from hydrate in the permafrost. There is a hydrate deposit overlying the free gas zone and hydrates were produced from this field semicontinuously for 17 years. The production in the Messoyakha field has been due to both depressurization (via the production of the free gas reservoir) and injection of inhibitors, as well as combinations of the two (Sloan and Koh, 2008).

Production from the field began in 1969 and produced for around two years while the pressure conditions were still above the hydrate dissociation point. After that, hydrates started to dissociate and the pressure exceeded expected values. Since 1982 the production has been moderate and the produced amount of gas has been equivalent to the amount of gas liberated from hydrate. Gas liberated from hydrates has amounted to around 36% of the total amount of gas produced from the field (Sloan and Koh, 2008, Makogon, 1997).

### 2.7.2. Mallik

The Mallik 2002 well is the first scientifically documented evidence that gas could be produced from hydrates; Messoyakha provided an incentive for further research with scientifically enhanced testing at Mallik. The major accomplishments of Mallik 2002 was that gas immediately was produced, with certainty from hydrates, via depressurization and thermal stimulation, and data were obtained for calibration of well logs and simulation of hydrate production (Sloan and Koh, 2008).

Lessons learned from Mallik include that gas hydrate deposits are much more permeable than previously thought, that they contain natural fractures and that they can be fractured artificially (Collett, 2005). The extensive monitoring of the project led to optimistic projections for gas production from hydrates in the future.

### 2.7.3. Ignik Sikumi

Ignik Sikumi #1 is of high relevance to this thesis as it was drilled and designed specifically for testing $CO_2$-$CH_4$ exchange in hydrate-bearing sandstones. The field test was started in 2011 in the North Slope of Alaska, in permafrost. Schoderbek et al (2012) wrote a paper about this field trial in 2012 stating that the trial was a success.

According to Schoderbek et al (2012), the well was drilled vertically to a depth of around 790m encountering four hydrate-bearing sandstones. The upper sand, “C Sand”, was chosen for injection due to the highest hydrate concentrations, its thick-bedded, homogeneous character and pressure and temperature regimes closest to laboratory tests. It has been shown that a spontaneous in-situ exchange between methane and carbon dioxide will happen in a hydrate saturated core under exposure to liquid CO2 (Ersland et al., 2010, Baldwin et al., 2009).

NMR logging and multi-mineral models indicated a hydrate saturation, $S_H$, of 76% in the homogeneous 14m thick Upper C sand interval, and that the remaining pore volume was filled with water and not free gas (Schoderbek et al., 2012). Schoderbek (2012) mentions two critical issues during the planning of the test: the free water could cause loss of injectivity due to secondary hydrate formation upon injection of $CO_2$, and the injection pressure of $CO_2$ could exceed the parting pressure of the reservoir. To avoid secondary hydrate formation, modeling of a different compositions of $CO_2/N_2$ in the injection gas was carried out, giving results suggesting that the optimal composition was 23% $CO_2$ + 77% $N_2$ (mole percent) (Schoderbek et al., 2012). This composition gives a single phase vapor injectant, something that simplified the testing.

The injection phase of the test lasted for fifteen days, injecting a total volume of around 210 mscf of mixed gas, reaching bottomhole pressures of near 1420 psia (Schoderbek et al., 2012). The next step, the production, was executed in four phases over a five week period: 1) Unassisted flowback, 2) Jet pumping above $CH_4$-hydrate stability pressure, 3) Jet pumping near $CH_4$-hydrate stability pressure, and 4) Jet pumping below $CH_4$-hydrate stability pressure (Schoderbek et al., 2012).

As can be seen in Figure 2-14 Ignik Sikumi #1 produced nearly 1000 mscf of gas. At the final stage the pressure was below the hydrate stability pressure and an additional increase in the production can be seen. Most of the 162 mscf of $N_2$ injected was recovered while more than half of the 48 mscf of $CO_2$ injected remained in the formation, as can be seen in Figure 2-15. (Schoderbek et al., 2012).

In Figure 2-14 the approximate time periods for the four production steps are drawn, showing that the fastest and most significant gas recoveries happen during jet pumping near and below methane hydrate stability pressure.

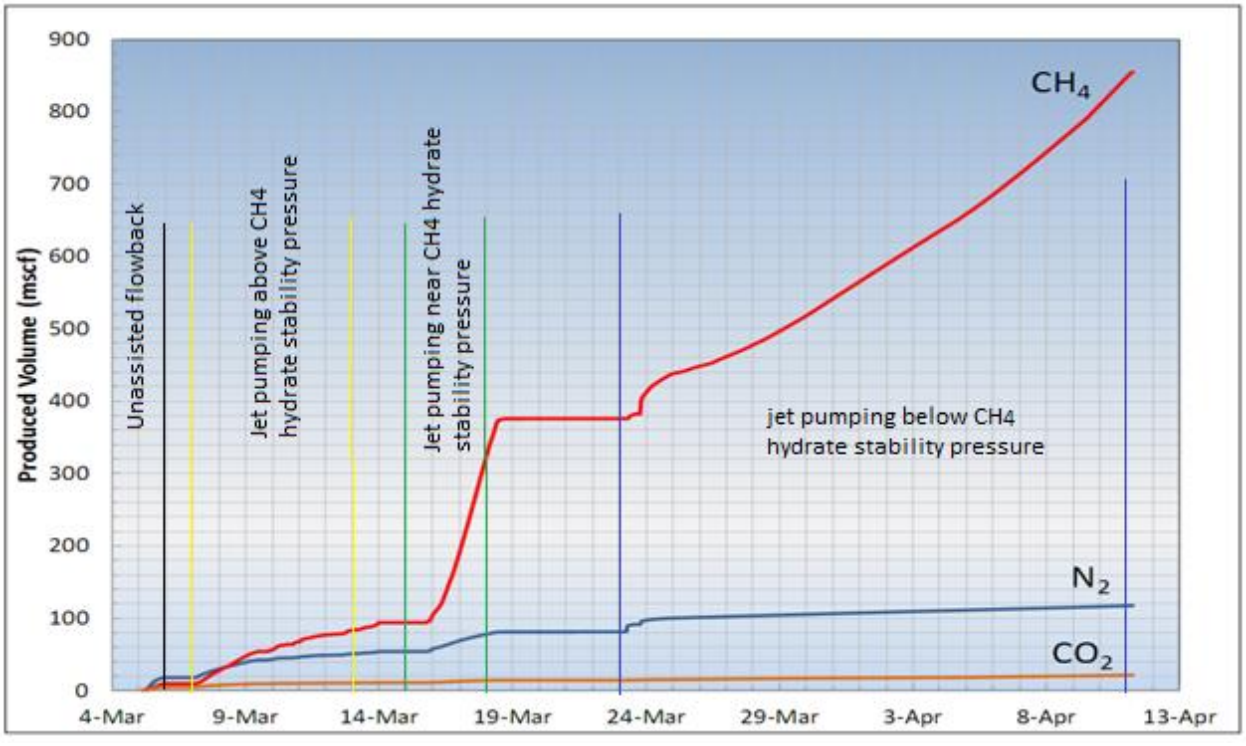


**Figure 2-14. Ignik Sikumi production curves showing produces volume of methane, nitrogen and carbon dioxide vs time. The final stage of the production, from 23 March to 11 April, was conducted below the methane hydrate stability region. Modified from (Schoderbek et al., 2012).**

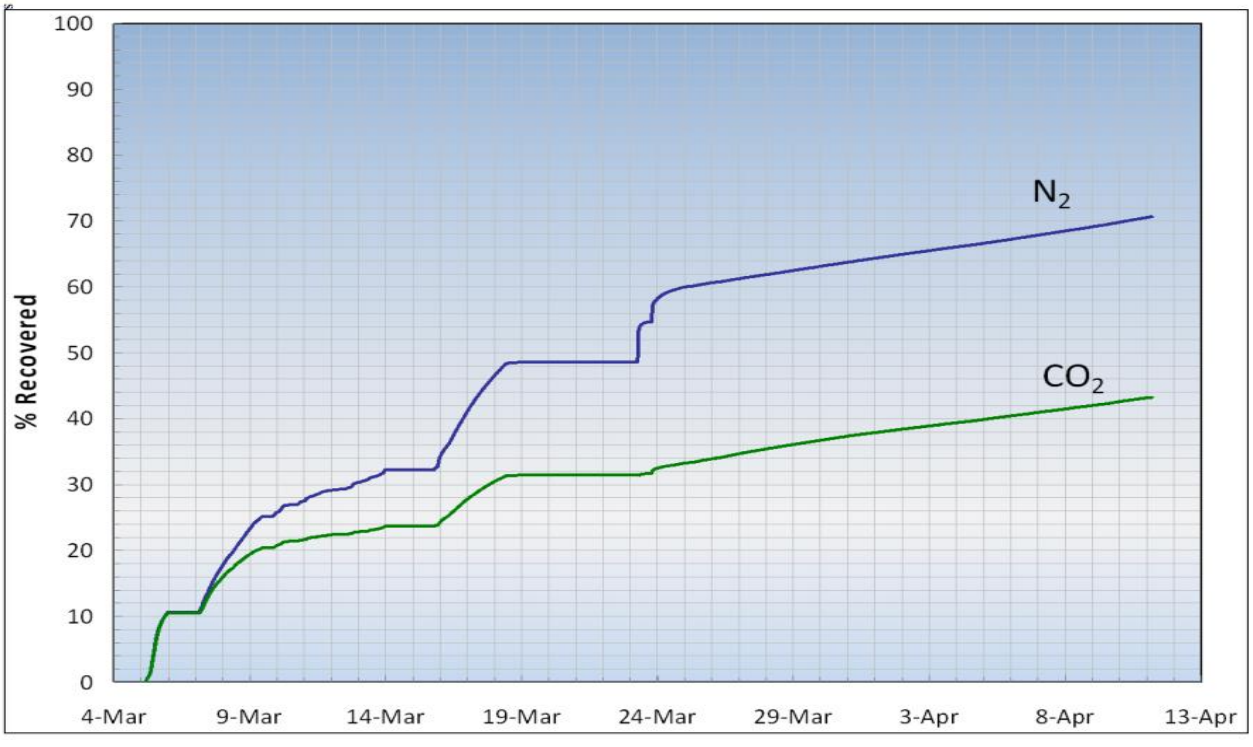


**Figure 2-15. Composition of injected gas produced at Ignik Sikumi #1 during the various phases of the production. Most of the injected $CO_2$ remained in the reservoir for storage (Schoderbek et al., 2012).**

# 3. Literature survey

Although $CO_2$ has been injected into geological formations for several decades and for various purposes - including enhanced oil recovery (EOR) - long term storage of $CO_2$ is a fairly new concept. The first commercial example is Weyburn in 2000, mentioned in chapter 1. This chapter will review relevant publications on topics that are important to understand in conjunction with $CO_2$ sequestration.

Aquifers are commonly seen as preferred $CO_2$ sequestration sites for anthropogenic $CO_2$ emissions due to their large capacity and the fact that they can be found all over the world. In order to safely store $CO_2$ for thousands of years in such formations, careful planning is of the essence. However, brine formations require significantly more effort to evaluate potential leakage risks compared to depleted oil and gas reservoirs that are known to have a sealing cap-rock (Sengul, 2006). Capillary trapping is seen as a quick way to store $CO_2$ safely since $CO_2$ is trapped as an immobile, residual phase surrounded by formation water.

A simulation study conducted by Nghiem (2009) shows that residual/capillary gas trapping and solubility trapping are important competing storage mechanisms and that residual gas trapping can be increased by water injection in low-permeability aquifers, but not in high-permeability aquifers. A different simulation study concluded that a larger number of wells enhances residual and solubility trapping, but lowers sweep efficiency (Chamwudhiprecha and Blunt, 2011). This study also showed that aquifer thickness plays a more important role on pressure response and immobilization than area.

A fundamental understanding of core-scale and pore scale multi-phase flow behavior of $CO_2$-water systems is important to anticipate and optimize storage capacity and trapping mechanisms. A steady-state experiment in a brine-$CO_2$-sandstone system conducted by Perrin (2009) confirmed, like this thesis, that $CO_2$ saturation is dependent on flow rate, with the displacement efficiency being higher for a higher flow rate. A transient and steady state measurement showed that 25% to 40% of the water is displaced by $CO_2$ in sandstone cores (Benson et al., 2005). Both these studies demonstrate that small heterogeneities may limit displacement efficiency. Pentland (2010 & 2011) showed that up to 35% of $CO_2$ is capillary trapped in a $CO_2$-brine-sandstone system (Pentland, 2010, Pentland et al., 2011). It has been proposed through capillary trapping experiments conducted at elevated temperatures and pressures on sandpacks and sandstones that a porosity of 22% is an optimal porosity for CO2 storage (Iglauer et al., 2011b).

A saturated $CO_2$-brine experiment, with similarities to experiments in this thesis, was conducted as part of a publication by S. Berg (2011). Findings show that a $CO_2$-water-sandstone system is not strongly water-wet; hence with respect to wettability it matters whether experiments are conducted with $CO_2$ or with model fluids. Findings by Pini (2011) and Qi (2009) also support this. The study conducted by Pini also presents a novel method for obtaining capillary pressure curves at core scale and sub-core scale in a $CO_2$-brine system using CT imaging for saturation measurements. This method was utilized in experiments for this thesis. Perrin and Benson (2009) conducted an experimental study using a medical CT scanner to map porosity in heterogeneous core samples and looked into the correlation between heterogeneity and $CO_2$ distribution.

Simulation studies on reservoir scale have proposed that injecting $CO_2$ and formation brine simultaneously, followed by chase brine will store more $CO_2$ securely than injecting $CO_2$ alone (Qi et al., 2009).

Several studies have been made on the subject of gas hydrate stability, $CH_4$-$CO_2$ exchange and gas hydrates as a safe way to store $CO_2$. Already in 1993 Ebinuma proposed that carbon dioxide was a more thermodynamically stable hydrate former than methane. It has also been shown that the exchange process Is favorable from a kinetics point of view (Lee et al., 2003). Since then there have been numerous studies on the subject of $CH_4$-$CO_2$ exchange and it has been verified using MRI in laboratory experiments that an exchange process is taking place in sandstone, where no heat is added (Graue et al., 2006b, Ersland et al., 2010, Baldwin et al., 2009). Professor Bjørn Kvamme has done extensive work on hydrates, both experimental (using MRI to visualualize and follow the kinetics of hydrate formation) and theoretical (using i.e. computer simulations), and has proposed storage of $CO_2$ in natural hydrate gas reservoirs with the added effect of an extra seal by the hydrates as well as produced natural gas (Kvamme et al., 2007).

The work of the hydrate group at the Institute for Physics and Technology at UoB headed by Graue and Kvamme has resulted in a successful pilot study on $CH_4$-$CO_2$ exchange in Ignik Sikumi in cooperation with Conoco Phillips (Schoderbek et al., 2012). Studies have been done to see if the exchange process can be enhanced by use of chemical additives (Hossainpour, 2013) and thermal stimulation (Hamre Håheim, 2013).

# 4. Experimental setups and procedures

The experimental part of the thesis - including experimental setup and procedures, rock material and core and fluid preparation - will be presented in this chapter. The results in this master thesis are based on experiments conducted at the lab and in the CT scanner at Haukeland University Hospital and in the hydrate laboratory at the Institute of Physics and technology (IFT) at the University of Bergen. The objective of these experiments is to study fluid behavior, trapping and storage potential and to obtain capillary pressure curves, all in a $CO_2$-brine-sandstone system, using a medical CT scanner and differential pressure measurements, as well as injecting $CO_2$ in methane hydrate for storage purposes.

## 4.1. Rock properties

Bentheim sandstone outcrop from the Bentheim quarry in Lower Saxony, Germany, was used in all experiments conducted in this thesis (see Figure 4-1). These samples have very homogeneous values in terms of mineralogy, pore distribution and permeability. The Bentheim sandstone is a sedimentary rock with typical porosity and permeability values of 23% and 1100mD, respectively. These samples also exhibit a uniform pore size distribution with an average diameter of 125 microns ($10^{-6}$m) and the mineralogy is 99% quartz with traces of the clay mineral kaolinite (Graue et al., 2006a, Husebø, 2008). Later studies from Ramstad and Rueslåtten (2013) have shown that the mineralogy varies and that Bentheim sandstone often consists of more than 95% quartz and minerals such as kaolinite, chlorite, carbonates, pyrite and K-feldspar in smaller amounts.

**Figure 4-1. Bentheim sandstone core. The diameter is around 5cm and the length is around 14cm.**

## 4.2. Fluids

The fluids used in the experiments at Haukeland University Hospital were prepared beforehand. Water was mixed with 5wt% of iodide salt (potassium iodide for the first experiment and sodium iodide for the rest). The water (with exception of the first experiment) was also saturated with $CO_2$ to achieve a condition of immiscible displacement during the experiments. As seen in Figure 1-8 in section **1.4.3.** temperature and pressure conditions impact the solubility of $CO_2$ in water. The amount of $CO_2$ needed to saturate the water was calculated based on data from Rochelle (2002) and a surplus of $CO_2$ was allowed to equilibrate with water in a shaker at the desired temperature and pressure for at least a day (see Figure 4-2).

**Figure 4-2. The shaker used for mixing of the live brine. The buffer was strapped to the bottom of the shaker, which was set for desired temperature, and connected to the ISCO pump in the front of the picture set to keep constant pressure.**

The $CO_2$ was saturated with brine (except for in the first experiment). The buffer used for live $CO_2$ preparation was too heavy for the shaker and therefore brine and $CO_2$ was just mixed in the injection pump. The amount of brine that is soluble in $CO_2$ is much lower than the amount of $CO_2$ that is soluble in brine, as seen in Figure 1-9. A surplus of brine was allowed to equilibrate with $CO_2$ under experimental conditions for a day before the experiment.

Table 4-1 shows the fluid properties for the fluids used in the experiments at Haukeland University Hospital.

**Table 4-1. Fluid data for the CT imaging experiments.**

| Fluid | Contents | Density, ρ (kg/m$^3$) | Viscosity, μ (cP) | Condition |
|---|---|---|---|---|
| **Carbon dioxide (l)** | CO2 | 799.65 | 0.0706 | 25˚C, 90 bar |
| **Live carbon dioxide (l)** | CO2+H2O+NaI | 799.65* | 0.0706* | 25˚C, 90 bar |
| **Live carbon dioxide (sc)** | CO2+H2O+NaI | 285-385* | 0.0231-0.0284* | 50˚C, 90-100 bar |
| **Dead brine** | H2O+KI | 1001* | 0.888* | 25˚C, 90 bar |
| **Live brine** | H2O+NaI+CO2 | 1001* | 0.888* | 25˚C, 90 bar |
| **Live brine** | H2O+NaI+CO2 | 991.9-992.3* | 0.548-0.549* | 50˚C, 90-100 bar |

Data from NIST web book. *: Values for the pure form of the fluids are used.

Cores intended for hydrate experiments were saturated by placing them horizontally in a container filled with water covering the lower part of the cores, leading to a spontaneous imbibition. The cores were then weighed to check if desired water saturation was reached. In the case of a too high saturation the cores were partially drained using a vacuum pump with the pump pressure kept well within a secure range to mitigate vaporization of water, thus minimizing risks of uncertainties related to changes in salinity.

## 4.3. Core preparation

The Bentheim sandstone cores used at Haukeland University Hospital were cut to lengths of around 10cm and the workshop at the institute reduced the diameter to around 5cm. The cores for hydrate experiments were cut to around 15cm of length. The cores were dried in a heating cabinet, weighed and measured. Three measurements were taken with a caliper and the average value was used. To minimize $CO_2$ exposure to the rubber sleeve in the core holder the cores were wrapped in aluminum foil and connected to the end-pieces using aluminum tape (see Figure 4-3).

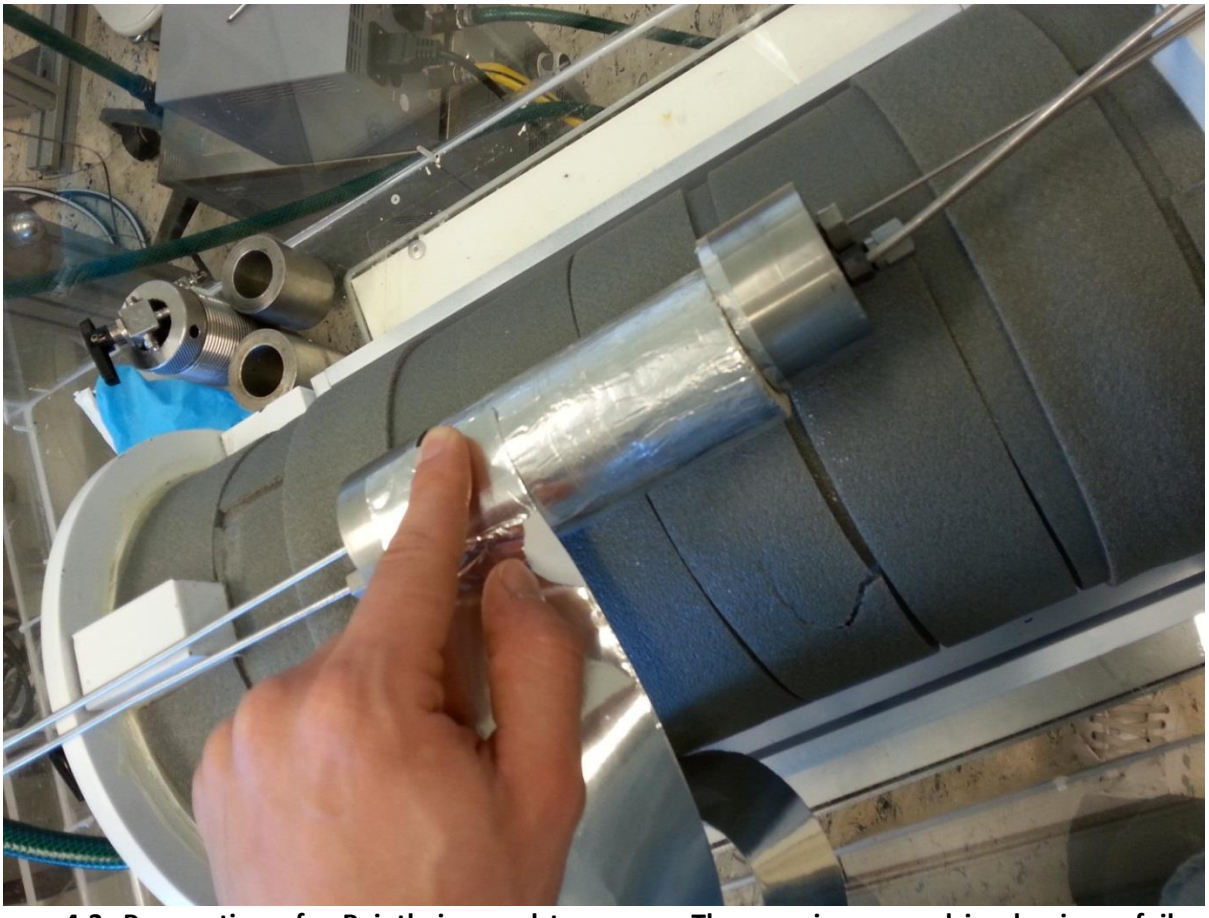

**Figure 4-3. Preparation of a Beintheim sandstone core. The core is wrapped in aluminum foil and aluminum adhesive tape covering part of the end-pieces.**

Cores used in hydrate experiments are saturated with brine - mixed to desired composition - by submerging the core horizontally into the brine mixture inducing a spontaneous imbibition. The saturation goal was calculated using the average porosity of the core and the core volume. A vacuum pump was used to remove excess water and then the core sample was wrapped in plastic and aluminum foil as explained above.

## 4.4. Experimental setup and procedure at Haukeland University Hospital

The setup used for the experiments at Haukeland University Hospital is shown in Figure 4-4. Time, effort, trial and error were needed to build and test the setup and it was modified and improved after each experiment. Fluid displacements utilizing $CO_2$ under high pressures and elevated temperatures requires a good setup design and high-quality equipment and it is a demanding task to obtain quality data. This chapter presents equipment used, experimental setups and procedures used for the $CO_2$-brine displacement experiments.

### 4.4.1. Experimental setup at Haukeland University Hospital

The experimental setup used on Haukeland was modified and improved for each experiment. Two high pressure Sanchez Technologies pumps were used; one for injecting $CO_2$ and one to receive produced fluids and keep a constant back pressure. One of two high pressure ISCO pumps kept a constant confining pressure at 120 bar and the other was used to inject oil into the injection buffer to drive brine through the core. A three-way valve was used to switch easily from $CO_2$ injection to brine injection. A thermometer was fitted at the inlet end-piece to monitor temperature at the inlet end of the core. Differential pressure across the core was also monitored by fitting tubing from a transducer straight to the end-pieces on each side of the core. The system was built mainly in the lab at Haukeland and wheeled into the CT room on trolleys (see Figure 4-7).

The first experiment was done in room temperature without a thermometer at the face of the core and without differential pressure measurements. The fluids were unsaturated (not live fluids) and the water bath and heating wire were not part of the system. The next experiment was conducted with saturated fluids (live fluids) as well as temperature and differential pressure measurements. Experiment number three was carried out at 50˚C using the water bath and the newly fitted heating wire around the injection pump and buffer. To prevent heat loss from the tubing it was covered in heat-isolating tape, however a heat-loss was still experienced. The volume produced in the production pump was significantly lower than the injected volume due to a change in density because the production pump kept room temperature. To mitigate this change heating wire was wrapped around the production pump for the following experiments and an additional heating wire was made to keep parts of the injection tubing heated in experiment 5. Experiment 4 and 5, conducted together with Dr Stefan Iglauer from the Department of Chemical & Petroleum Engineering at Curtin University, was thought to require the possibility of injecting live brine and live $CO_2$ simultaneously. The three-way valve at the inlet-side was

then switched to two two-way valves; however, co-injection was not necessary. A figure (Figure A1) of the modified setup is included in the appendix.

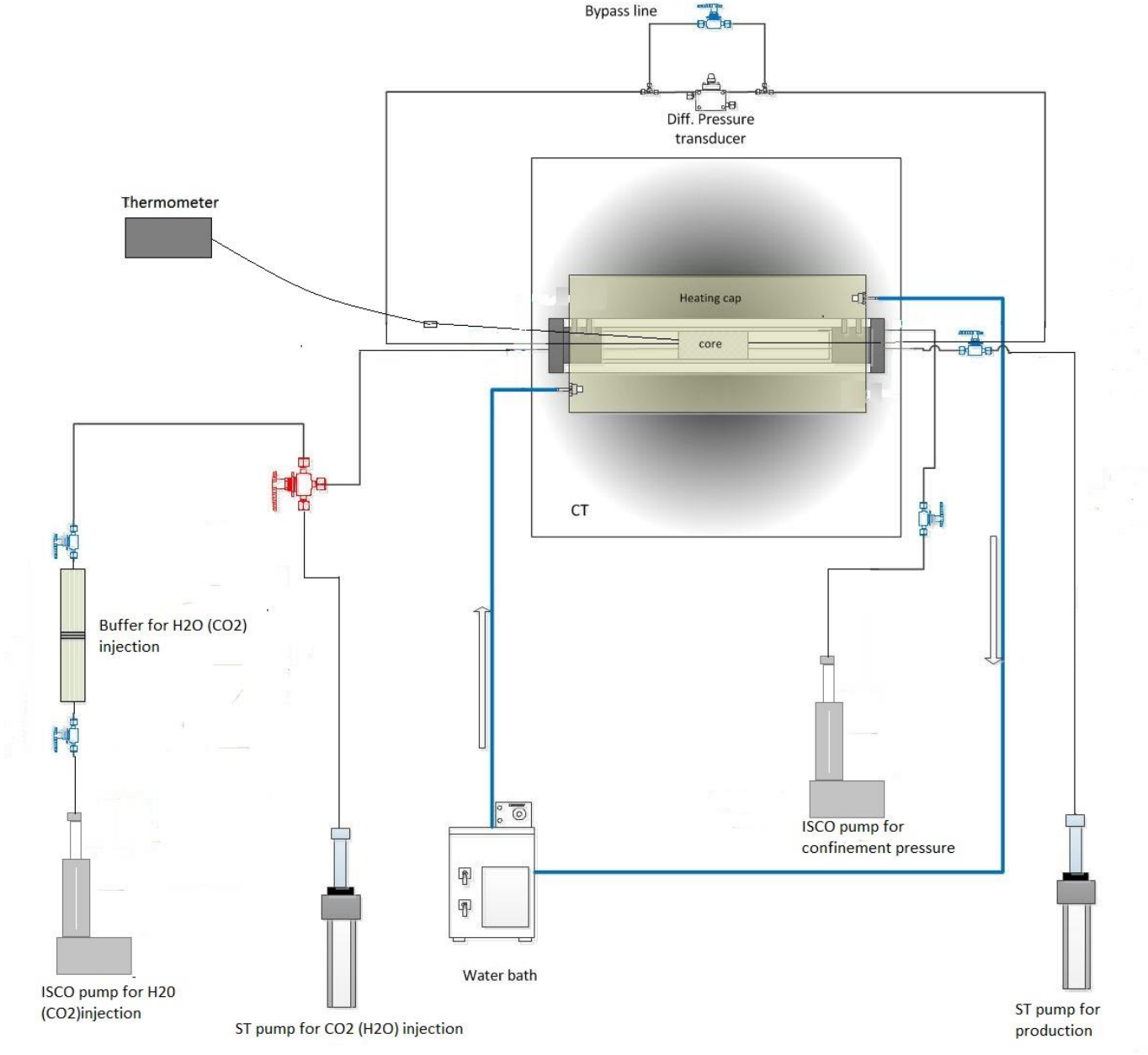


**Figure 4-4. Experimental setup used at Haukeland Uniersity Hospital. A heating wire was wrapped around the injection buffer, ST pump for injection and the ST pump for production.**

**Equipment used at CT-setup at Haukeland University Hospital**

- Aluminum core holder for 2" cores
- Customized polyoxymethylene (POM) heating cap from UoB workshop
- 2 x ST pumps (Sanchez technologies) 1 liter, with Falcon software
- 2 x ISCO syringe pumps 265ml
- 2 laptop computers for logging and pump software
- Validyne P61 differential pressure transducer
- Swagelok tubings, fittings and valves
- Autoclave fittings and valves
- Omega multilogger thermometer HH506RA
- Buffer/accumulator
- 5 trolleys to wheel setup into CT room
- Around 30m of heating wire from RS Components, fitted with termination kits, thermostat, wall socket and junction boxes
- Siemens Biograph ™ TruePoint ™ medical PET/CT scanner
- Gyrotory shaker with heating element for fluid mixing
- Grant heating/cooling bath

### 4.4.2. Computed tomography (CT) imaging

Imaging the distribution of porosity, permeability, and fluid phases is important in order to understand single and multiphase flow characteristics of porous media. X-ray computed tomography (CT) has become an increasingly more important and powerful tool for non-destructive imaging. It can offer fine spatial resolution, is easy to apply and is adaptable to many types of experimental procedures and flow conditions (Akin and Kovscek, 2003). In this thesis a CT is used to image fluid saturations and distributions. Together with differential pressure over the core sample being monitored, this also gives a promising and quick way of obtaining capillary pressure curves (Pini et al., 2011).

Computed tomography (CT) uses an X-ray source that rotates around the sample to obtain one-dimensional projections of X-ray attenuation at different angles (see Figure 4-5). A detector on the opposite side of the source measures the attenuation of the X-rays as they pass through the sample. A cross-sectional slice through the sample is then reconstructed by computer, and finally several such images constitute a three-dimensional image of the sample (Vinegar, 1986).

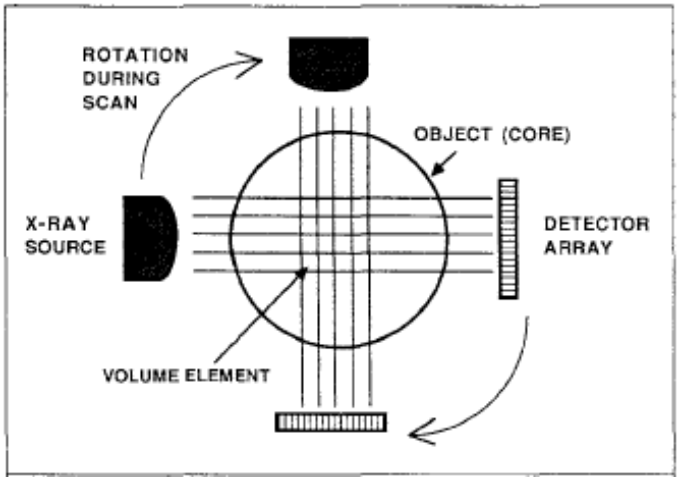


**Figure 4-5. Schematic showing the principle of how a CT apparatus operates (Withjack, 1988).**

The intensity of the electromagnetic X-ray radiation is affected by Compton-scattering (higher intensity) and absorption (lower intensity). The linear attenuation coefficient, $\mu_a$, for the material a, is measured. It is given in Beer-Lamberts law (Beer, 1852) which is given in the following equation:

$$I = I_0 e^{-\mu_a x} \tag{4.1}$$

Where $I_0$ is the intensity of the incident beam, I, is the intensity after passing through the material and x is the thickness of the material. The attenuation coefficient is larger for more dense materials and less for less dense materials. The CT computer converts attenuation coefficients into corresponding numerical value, CT numbers. In general higher CT numbers are associated with greater attenuation of the X-rays, and in a given material, higher intensity beams display less attenuation (lower CT numbers) than lower intensity beams (Withjack, 1988). This implies that high CT numbers are associated with high density materials.

The water saturation during multiphase flooding experiments was calculated using the following equation (Akin and Kovscek, 2003):

$$S_w = \frac{CT_{wr} - CT_{gwr}}{CT_{wr} - CT_{gr}} \tag{4.2}$$

The subscript gwr refers to rock containing two phases, gas and water, while wr and gr refer to rock fully saturated by water and gas, respectively. The CT numbers are attenuation coefficients converted into corresponding numerical values and are given in Hounsfield units. Each Hounsfield unit represents a

0.1% change in density with respect to a calibration density scale. Akin and Kovscek (2003) is recommended for further reading.

All images in these experiments were taken with Siemens Biograph$^{TM}$ TruePoint$^{TM}$ medical PET/CT scanner at Haukeland University Hospital. Up to around 90 scans were taken for each experiment obtaining 228 slices for each scan. The resolution used was 1.947 pixels per mm and the voxel size was 0.51x0.51x0.60 mm.

### 4.4.3. Capillary pressure measurements

The method for obtaining capillary pressure curves used in this thesis, explained in the following, was presented by Pini (2011) and utilizes an experimental configuration similar to the one used in traditional steady-state relative permeability experiments. The experimental setup in this thesis is inspired by the setup used by Pini (2011) and our aim was to be able to perform the novel method presented in his work.

The core is initially fully saturated with the wetting fluid (water) and the non-wetting phase ($CO_2$) is injected at a constant flow rate. The outlet pressure is kept constant and the pressures at the inlet ($P_1$) and outlet ($P_2$) are continuously monitored. After a while the water production stops and equilibrium (steady-state) conditions are reached. The wetting phase pressure then reaches a constant value, provided that this phase is continuous across the core, which is expected for a strongly water-wet core. Across the outlet face of the core the pressure of the wetting fluid is continuous while the pressure of the non-wetting fluid might not be. The capillary end-effect is a result of this and it is proposed that the capillary pressure at the outlet of the core might take a finite value, before jumping to zero just outside the core (Richardson et al., 1952). The pressure drop across the core $\Delta P = P_1 - P_2$ corresponds to the capillary pressure at the inlet face of the core. When measuring the saturation at the inlet face of the core using CT scans a direct correlation between saturation and capillary pressure can be established, and by repeating these measurements for increasing $CO_2$ flow rates a capillary pressure curve can be obtained.

In order for the water pressure to remain continuous, water contact has to be maintained at the outlet of the core. If this condition is not met the pressure drop across the core does not correspond to the capillary pressure at the inlet face of the core. This is achieved using an end-cap that provides a small space for fluids at the outlet face of the core.

Another essential premise for this methods application is that the system behaves in the same way as in the absence of viscous and buoyancy forces (Wilkinson, 1986). This can be assessed quantitatively by considering the relative strength of viscous to capillary forces:

$$\frac{\Delta Pvisc}{\Delta Pcap} \sim \frac{u\mu/k}{\gamma_{12}/r} = KN_c \qquad (4.3)$$

Where the capillary number is given by $N_c = u\mu/\gamma_{12}$, where $\mu$ is the displacing fluid viscosity, $u$ is the superficial velocity and $\gamma_{12}$ is the interfacial tension. $K = r^2/k$, where *K* is a constant that depends on the permeability *k* and the grain size *r* (Wilkinson, 1986). No gravity segregation can be observed within the core (see Fig. 5-2) and thus the applicability of the method is confirmed.

### 4.4.4. CT imaging of $CO_2$ and brine displacements at Haukeland University Hospital

All cores were initially saturated with brine, followed by a primary drainage by injecting $CO_2$ (saturated with brine in all experiments except experiment 1), representing the initial migration of $CO_2$ through the aquifer. Then brine saturated with $CO_2$ (unsaturated brine in experiment 1) was injected, representing the trailing edge of an advancing $CO_2$ plume or artificial brine injection. Some $CO_2$ is displaced in this step, leaving behind a residually trapped fraction of $CO_2$. A secondary drainage was then carried out and a possible hysteresis effect was seen. The experimental conditions are representative of a deep saline aquifer showing typical storage conditions.

#### *Experiment 1- unsaturated fluids at 25˚C and 90 bar*

For this experiment brine (water and potassium iodide 5wt%) and pure liquid $CO_2$ was used. The Bentheim sandstone core was prepared as discussed in section **4.3**. The equipment was wheeled into the CT room on trolleys (see Figure 4-7) and the setup was put back up. The core holder was positioned in the CT scanner (see Figure 4-6) and a test scan was taken in order to see that the positioning was satisfying. A scan of the core pressurized to 90 bar with 100% $CO_2$ was taken, then the system was opened to the atmosphere and a dry scan was acquired. The system was then re-pressurized with 100% brine and a new scan was acquired. Confinement was kept at 120 bar and the temperature of the room was 24˚C. To avoid differences in the X-ray damping around the core, room tempered water was filled in the heating cap, even though there was no circulation.

The primary drainage was started by injecting $CO_2$ at increasing rates (1ml/min, 2ml/min, 5ml/min, 10ml/min, 20ml/min and 50ml/min). However, the rate did not increase particularly beyond 1ml/min

and an increasing injection pressure was observed due to a broken valve and tubing. Hence the injection rate was not increased beyond 5ml/min. A pore volume (≈50ml) of $CO_2$ was supposed to be injected at each rate prior to scanning the sample and increasing the rate.

The three-way valve at the inlet side of the core holder was turned in order to inject brine for forced imbibition. Brine injection was carried out in the same way as the $CO_2$ was supposed to (with rates of 1ml/min, 2ml/min, 5ml/min, 10ml/min, 20ml/min and 50ml/min), with scans acquired after each flow rate. The ISCO pump injecting oil into the buffer injecting brine to the system needed to be refilled with oil during the experiment because the pump volume was too low.

Due to the $CO_2$ injection in this experiment being compromised by a bad valve and tubing, the secondary drainage was only carried out with rates 1ml/min and 2ml/min. The ST pump that was used as an accumulator for produced fluids was set to keep constant pressure except for the two highest rates where it was set to retract with a constant rate similar to the injection rate. All pump data were logged during the experiment and the experiment was conducted over two days.

### *Experiment 2 – saturated fluids at 25˚C and 90 bar*

For this experiment sodium iodide was mixed in distilled water (5wt%) instead of potassium iodide. The fluids were also saturated with each other (live fluids). The brine was introduced to $CO_2$ and mixed in the shaker. The buffer with $CO_2$ was too heavy for the shaker so it was instead left to equilibrate with a few ml of brine. In an ideal case live fluids make the displacement immiscible, whereas in experiment 1 - with unsaturated fluids - the displacement was miscible. The sandstone core was prepared and the equipment wheeled in to the CT room set up and positioned in the scanner. The system pressure was 90 bar and confinement 120 bar. This experiment was conducted with no circulation from the heating bath, but the heating cap was filled with water. 100% $CO_2$, dry, 100% dead brine and 100% live brine scans were acquired.

The broken tubing and valve from experiment 1 was fixed. Hence the procedure for primary drainage, secondary drainage and imbibition was executed the way it was planned for experiment 1 (1ml/min, 2ml/min, 5ml/min, 10ml/min, 20ml/min and 50ml/min). The high pressure ST pump that was used as an accumulator for produced fluids was set to keep constant pressure except for the two highest rates where it was set to retract with a constant rate similar to the injection rate. The temperature and differential pressures were logged in addition to all the pump data. The experiment was conducted over two days.

### *Experiment 3 – Saturated fluids at 50˚C and 90 bar*

In experiment 3 the live brine was mixed the same way as in experiment 2 except at 50˚C. The live $CO_2$ was made by putting a few ml of brine (excess brine) into the ST pump before filling it with $CO_2$ at 90 bar pressure. A heating wire was wrapped around the ST pump to ensure that the live $CO_2$ kept 50˚C and also around the live brine buffer. The injection tubing was insulated. The core preparation and system setup was otherwise the same, except for the heating bath circulating 50˚C water through the heating cap, maintaining the core at desired temperature. System pressure was 90 bar and confinement 120 bar. 100% $CO_2$, dry, 100% dead brine and 100% live brine scans were obtained.

The displacement procedures were the same as in the two previous experiments except one difference: for the first rate of each displacement (1ml/min) a scan was taken every three minutes instead of after injecting a whole pore volume. This was done in order to better visualize the initial displacements.

In this experiment the production pump was set to constant pressure all the time except for the two highest rates of live brine injection. The production pump was not preheated, therefore the $CO_2$ volume decreased upon cooling after passing through the system and constant retraction rate was not necessary and it would also have been difficult to set the correct rate. For the two highest rates of live brine injection the production pump was set to retract at the same rate as the injection rate, since the brine does not go through the same density changes in the different temperature regimes as the $CO_2$.

The temperature, differential pressure and all pump data were logged during the experiment. The experiment was done in two days.

### *Experiment 4 – saturated fluids at 50˚C and 90 bar*

Experiment 4 was conducted with Dr. Stefan Iglauer from Curtin University. The fluids and core were prepared in the same manner as earlier and the equipment was set up after being wheeled into the CT room. In addition to a dry scan, a 100% dead brine scan, a 100% live brine scan and a 100% $CO_2$ scan a scan was taken after opening the valve between the $CO_2$ and the system before starting the injection. The pressure regimes were the same as earlier: 90 bar pore pressure and 120 bar confinement pressure. In this experiment the production pump was also covered in heating wire to mitigate the density changes after the fluids passed through the system.

The primary drainage was similar to previous experiments, except 60ml of fluid was injected for each rate. The same goes for the secondary drainage. A spontaneous imbibition method was introduced in this experiment. 10ml slugs of brine were injected at 2ml/min followed by CO2 injection with decreasing

rates (20ml/min, 10ml/min, 5ml/min, 2ml/min, 1ml/min). A scan was taken after each brine slug. After the spontaneous imbibition, a forced imbibition was performed in a similar manner as in the previous experiments. The secondary drainage was started at a lower rate than in the previous experiments. $CO_2$ was injected at 0.1ml/min overnight (with the production pump retracting at constant rate 0.1ml/min) before conducting the rest of the drainage in the same way as in previous experiments. The temperature, differential pressure and all pump data were logged during the experiment. The experiment was carried out over two days.

### *Experiment 5 – saturated fluids at 50˚C and 100 bar*

This experiment was also conducted together with Dr. Stefan Iglauer. The fluids and core were prepared in the same manner as earlier except that the fluids were mixed at 100bar pressure because that was the experimental pressure. The equipment was wheeled in and set up similar to previous experiments and the preliminary scans were taken. Part of the injection tubing was also covered in a newly installed heating wire in this experiment.

The primary drainage was started with a $CO_2$ flood at 1ml/min and 3 CT scans were taken before increasing the rate to 2ml/min. Then another nine scans were acquired and the rate was increased to 5ml/min. One scan was obtained for this and each successive rate (10ml/min, 20ml/min, 50ml/min and 70ml/min). The production pump pressure was controlled manually by adjusting the retraction rate to keep the pressure at around 100bar. The spontaneous imbibition was done similar to experiment 4 except with decreasing $CO_2$ rates starting at 65ml/min (then 55ml/min, 45ml/min, 35ml/min, 25ml/min and 15ml/min). The forced imbibition was conducted with rates 1ml/min, 2ml/min, 5ml/min, 10ml/min, 20ml/min and 50ml/min with scans taken after each rate. The secondary drainage was conducted with rates 1ml/min, 5ml/min, 10ml/min, 20ml/min, 50ml/min and 70ml/min with scans taken after each rate.

The temperature, differential pressure and all pump data were logged during the experiment. The experiment was conducted over two days.

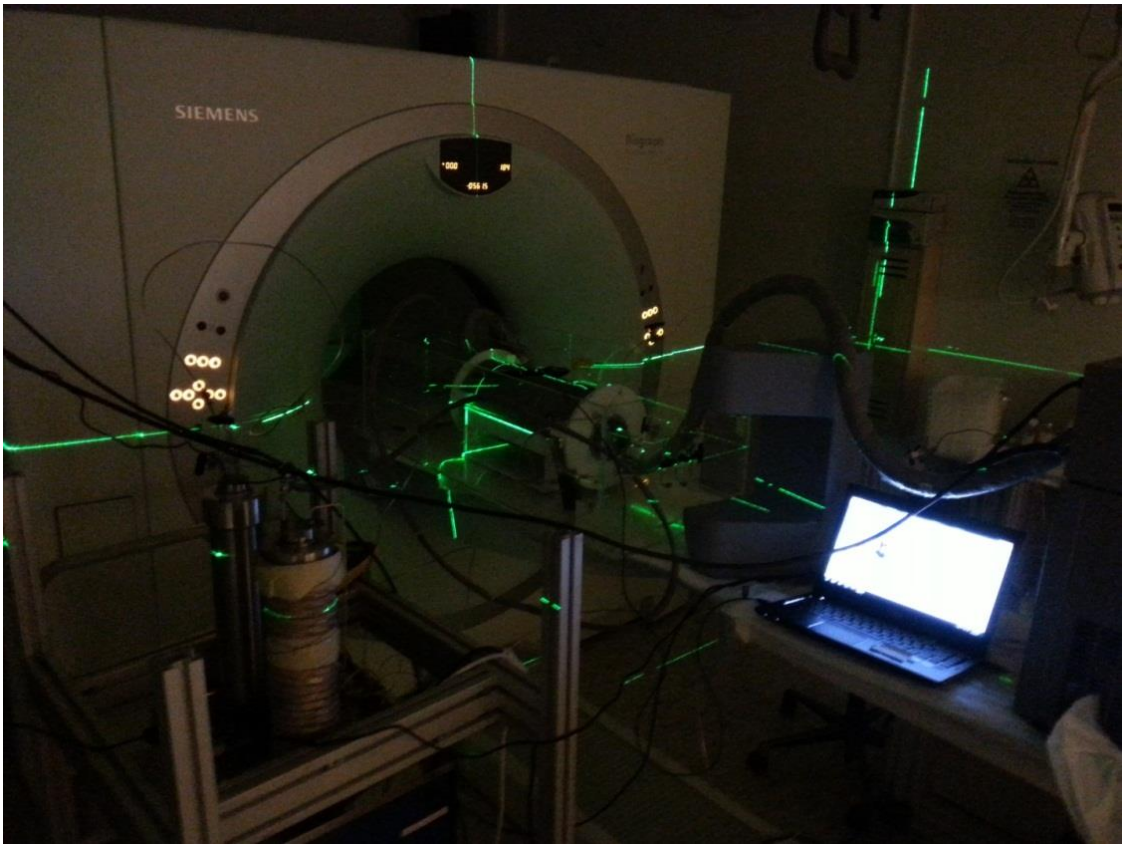


**Figure 4-6. Positioning of the core in the CT. The lasers create a grid of lines to make positioning easier.**

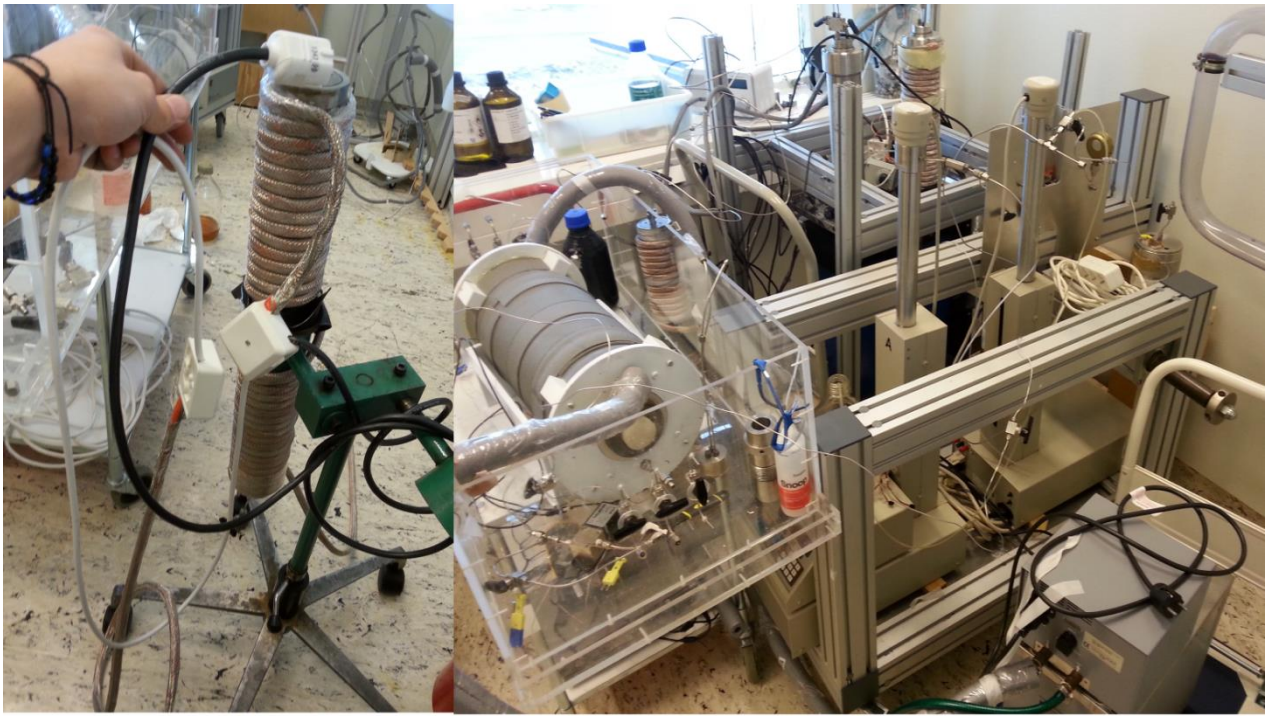

**Figure 4-7. The setup at the small lab on Haukeland before it was wheeled in to the CT room. Five trolleys were used: one for the two ST pumps, one for the two ISCO pumps, one for the core holder, one for the heating bath and one for the live brine buffer (left).**

## 4.5. Experimental setup and procedure at the hydrate lab

The focus of this thesis is $CO_2$ storage and therefore the potential for storage in hydrates, through $CO_2$ injection in hydrate bearing sandstone, was investigated. This chapter presents equipment used, experimental setup and procedure used for $CH_4$-$CO_2$ exchange at the hydrate lab.

### 4.5.1. Experimental setup at the hydrate lab

The setup at the hydrate lab is schematically illustrated in Figure 4-8. The hydrate lab consists of three different setups: setup A (resistivity), setup B (baseline) and setup C (temperature). In all setups Bentheim sandstone is used as the porous medium for methane hydrate to form. After hydrate is formed the $CH_4$-$CO_2$ exchange process is started and after this the hydrate is dissociated. There were some problems with the GC in the fall of 2013 and in 2014 the cooling baths stopped working, hence only setup C was used for experiments conducted for this thesis and time for experiments was severely limited.

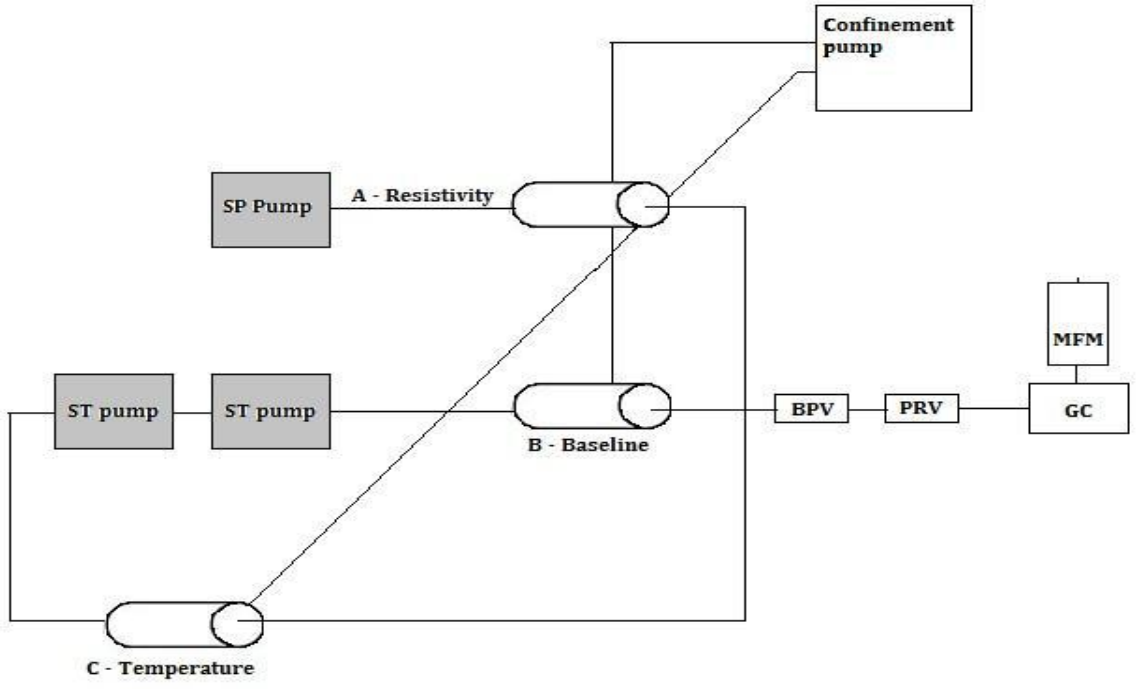


**Figure 4-8. Schematic overview of the hydrate laboratory at the University of Bergen. All three setups have cooling jackets. Setup A measures resistivity, setup B is used as baseline and setup C is used for temperature experiments. Production line and confinement pump are also illustrated. Only setup C is used in this thesis. (Hamre Håheim, 2013).**

Setup C is schematically shown in Figure 4-9. A cooling bath circulates antifreeze through the cooling cap that encloses the core holder, maintaining the desired temperature in the system. The temperature is logged at the surface of the core sample by an Omega Multilogger thermometer at the inlet side. The ISCO pump is used to reach the desired confinement pressure, surpassing the pore pressure, and then the buffer is used to maintain the desired pressure. One part of the buffer is filled with N-Decane oil and the other side is pressured with Nitrogen. The bypass valve makes it possible to isolate the core during the experiment and change the gas in the system as well as injecting gas from both sides simultaneously. The pressure transducers monitor pore pressure during the experiment. At the production end the fluids first meet a back pressure valve (BPV) set to 86 bar using nitrogen. If the pore pressure exceeds this set pressure (86 bar) the BPV releases gas to maintain desired pressure. Next in line is the Swagelok pressure regulator that ensures a lower output pressure to the Gas Chromatograph (GC) which has a pressure limit. A Bronkhorst Mini Cori Mass Flow Meter (MFM) measures produced gas.

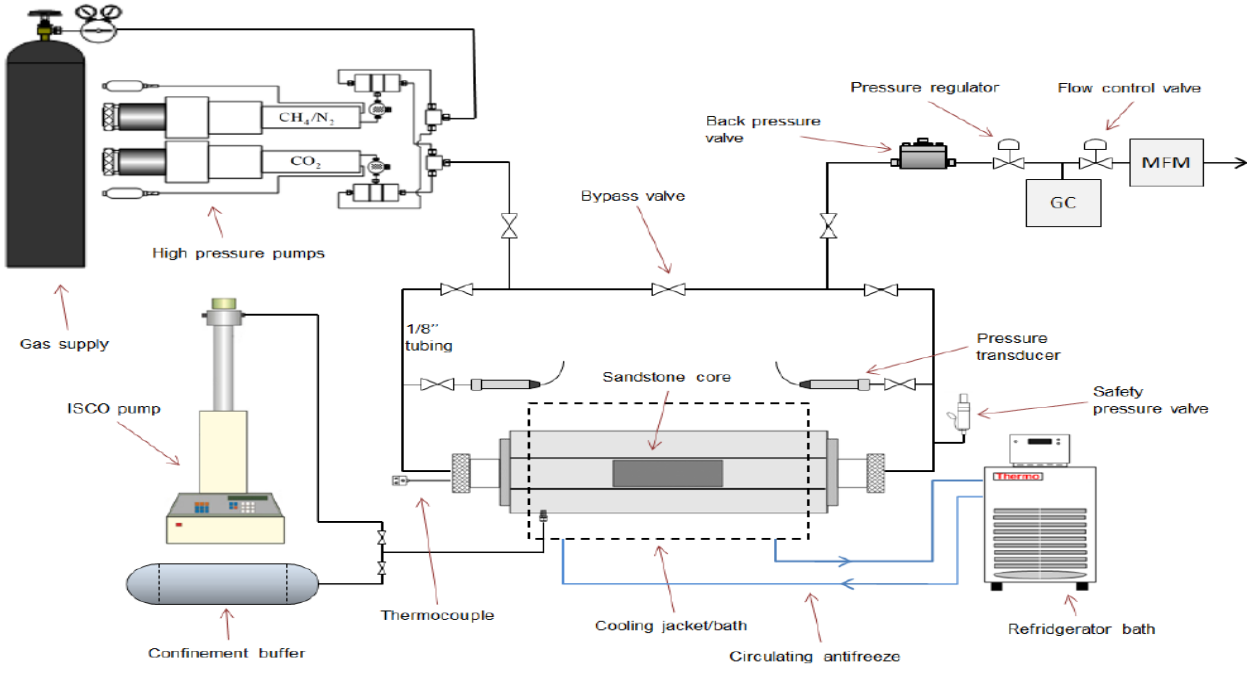


**Figure 4-9. Hydrate setup C. Confinement system consisting of an ISCO pump and a buffer, refrigerator bath circulating antifreeze to maintain desired temperature in system and the system inlet is connected to two high pressure ST pumps used for hydrate formation and $CO_2$ injection. (Hågenvik, 2013)**

**Equipment used at the hydrate lab**

- Hassler Type Core Holder
- Customized Cooling jacket from UiB workshop
- Sanchez Technologies Stigma 300 Pump (ST pump), with Falcon software
- Thermo Neslab Digital Plus RTE17 refrigerated bath circulator
- Omega Multilogger Thermometer HH506RA
- Edwards RV3 Vacuum pump
- Agilent Technologies 3000 Micro Gas Chromatography (GC)
- Bronkhorst Mini Cori Flow, Digital Mass Flow Meter/Controller (MFM)
- Back pressure valve with nitrogen applied at 86 bar
- Swagelok Pressure Regulator (high pressure to low pressure)
- Swagelok manometers (confining pressure and pressure regulator)
- Haskel pump
- Isco Series D Pump (confinement pressure build up pump)
- Buffer (Confinement pressure)
- 2 Unik 5000 Pressure sensors/transducers
- Druck DPI 610 calibrator
- Slug Injector

### 4.5.2. $CH_4$-$CO_2$ exchange at the hydrate lab

#### *Hydrate formation procedure*

After saturation and preparation of the core it was mounted in the core holder, the outlet and inlet valves were closed and the system was vacuumed to remove any gas from the system. The system was then pressurized to the desired pressure with $CH_4$ from both sides, keeping the confinement pressure above system pressure. Inlet, outlet and bypass valves remained open throughout the formation process while the pump was set to keep constant pressure of 83bar. The temperature was set to 4˚C. PVT data were logged and hydrate formation can be observed by the amount of gas consumed. When gas consumption was stable and at a rate close to zero the formation is completed. The system was then tested for leaks. During the formation the pump stopped for a while and was started again. Implications are covered in chapter 5.

#### *$CH_4$-$CO_2$ exchange procedure*

The core was isolated and the rest of the tubing and system were cleaned and vacuumed. The pump and the rest of the system were both filled and pressurized to 83bar with $CO_2$. The bypass valve was closed, inlet and outlet valves were opened and the ST pump was set to inject with a constant rate of 0.1ml/min inducing a pressure build up. When the pressure exceeded 86bar (BPV pressure) the back pressure valve released produced gas to the pressure regulator. The pressure regulator was set to let gas through at 1.5bar pressure due to limitations in the GC. Composition and mass of the produced gas were measured in the GC and MFM, respectively. A choke valve before the GC ensured a steady flow through the GC. Logging of the composition and mass produced enabled estimation of the methane produced and the $CO_2$ stored. The flow from the MFM went to the ventilation chamber.

The relatively high injection rate allowed for one pore volume to be injected in a day. This experiment was conducted by injecting $CO_2$ for around 8 hours then closing the production valve and set the pump to keep constant pressure. The first flow was done on day 1 and then the production valve was closed for day 2 and day 3. On day 4 the procedure was repeated, closing the production valve overnight and repeating this procedure on day 5.

The conditions during the exchange process were well within both the methane hydrate and carbon dioxide hydrate stability zone.

# 5. Results and discussion

In this chapter the experimental results are presented and discussed. The CO2-water displacement experiments conducted at Haukeland will be presented first followed by gas hydrate experiments carried out in-house at the Department of Physics and Technology. Observations are discussed as the results are presented.

## 5.1. CT imaging of live $CO_2$ and live brine displacements

This chapter will present data analyzed from the $CO_2$-brine displacements conducted at Haukeland. The similar parts of each experiment will be presented together making it easier to compare the results. The data presented will also be examined from a carbon dioxide storage perspective. Core data from the experiments are given in Table 5-1.

**Table 5-1. Core data.**

| Core ID | Weight dry (g) | Length (cm) | Diameter (cm) | PV (ml) | Desired system pressure (bar) | Desired system temperature (˚C) |
|---|---|---|---|---|---|---|
| **CO2_1** | 391.53 | 9.82 | 5.02 | 44.70 | 90 | 25 |
| **CO2_2** | 406.65 | 10.05 | 5.04 | 46.12 | 90 | 25 |
| **CO2_3** | 406.31 | 10 | 5.04 | 45.89 | 90 | 50 |
| **CO2_4** | 402.67 | 9.95 | 5.03 | 45.48 | 90 | 50 |
| **CO2_5** | 407.2 | 10.07 | 5.04 | 46.21 | 100 | 50 |

The permeability and porosity of these cores were not measured experimentally. Instead the typical permeability and porosity of Bentheim sandstone - 1100mD and 23%, respectively - was used because it is often used as a reservoir analog and considered a fairly homogeneous rock with evenly distributed pore sizes.

Figure 5-1 shows an example of a CT image visualized in ImageJ; a public domain, Java-based image processing program. The core, rubber sleeve, confinement oil, core holder and heating cap are included in the image. Figure 5-2 is a normalized CT image showing saturation distribution throughout the core. This image is processed in ImageJ: pixel sizes are increased fivefold, the picture is cropped, normalized and the colors are adjusted. This may be an effective tool for analyzing CT data from experiments and

predicting plume-migration at a carbon dioxide storage site. The results presented in this chapter are focused more towards saturation profiles than imaging from image processing programs, such as ImageJ. Saturation profiles provide a quick an easy way to observe the saturation distribution throughout the core and, in combination with pressure data, to obtain capillary pressure curves.

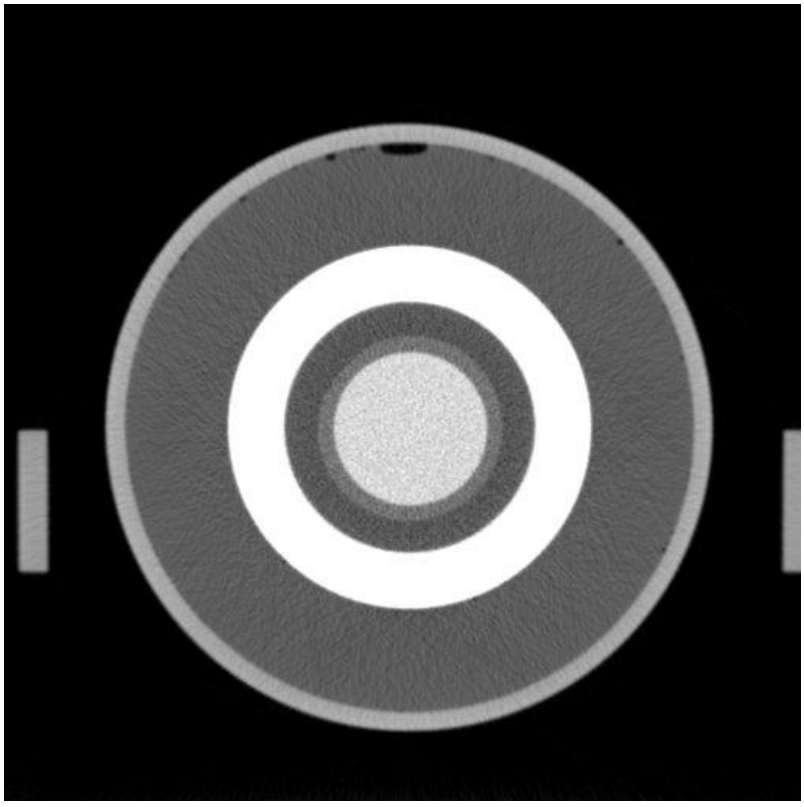

**Figure 5-1. A cross section CT-image of the core. The core sample is in the middle with the rubber sleeve, confinement oil, core holder, water and heating cap around it. An air bubble can be seen at the top of the image and part of the core holder stand can be seen at the left and right side. More dense materials show as a lighter color, i.e. the metal core holder is white and the air is black.**

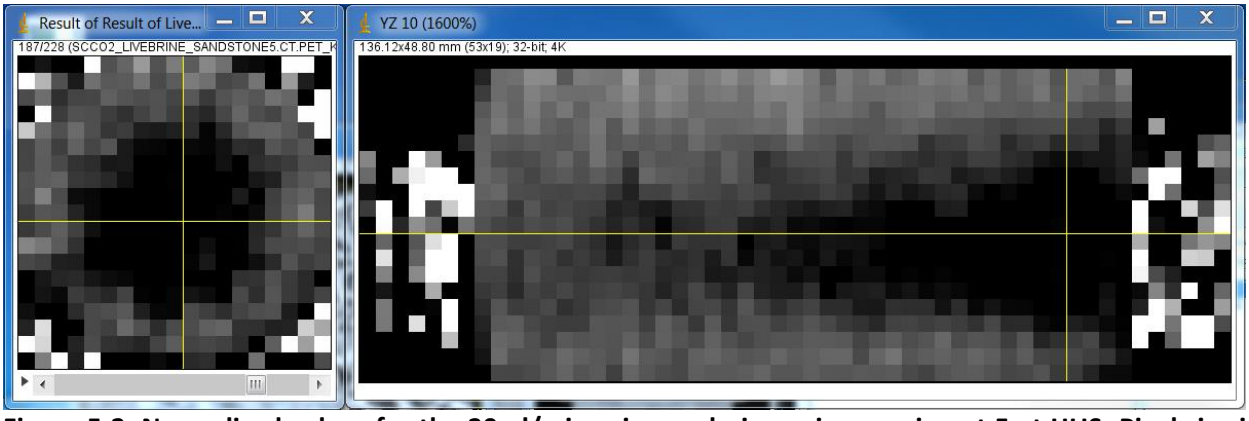


**Figure 5-2. Normalized values for the 20ml/min primary drainage in experiment 5 at HUS. Pixel size is increased by a factor of five. A cross-section of the XY-plane and the YZ-plane is seen. The darker the color, the higher water/$CO_2$-fraction. The XY-plane cross-section is from near the outlet end and a water cone with increasing diameter is seen towards the outlet.**

### 5.1.1. 100% scans for reference purposes

Figures 5-3 and 5-4 show the average Hounsfield values of the preliminary scans. Hounsfield units are higher the more the x-rays have been dampened. A higher Hounsfield number indicates more damping. Hence, these values represent the density of the core and the fluids occupying it. As expected water at 90 bar has the highest density, followed by liquid $CO_2$ and then air at atmospheric pressure.

The potassium iodide used in experiment 1 has a molar mass of 166g/mol and sodium iodide, used for the other experiments, has a molar mass of 150g/mol. This results in a slightly higher density for the fluids in experiment 1 although the density difference is too small to be seen in the figures (Fig. 5-3 and 5-4). The unsaturated brine in experiment 1 will also be slightly heavier than the saturated fluids used in the remaining experiments and likewise the unsaturated $CO_2$ should be less dense. This can be seen in Figure 5-4 where the live brine has a slightly lower CT value than the dead brine.

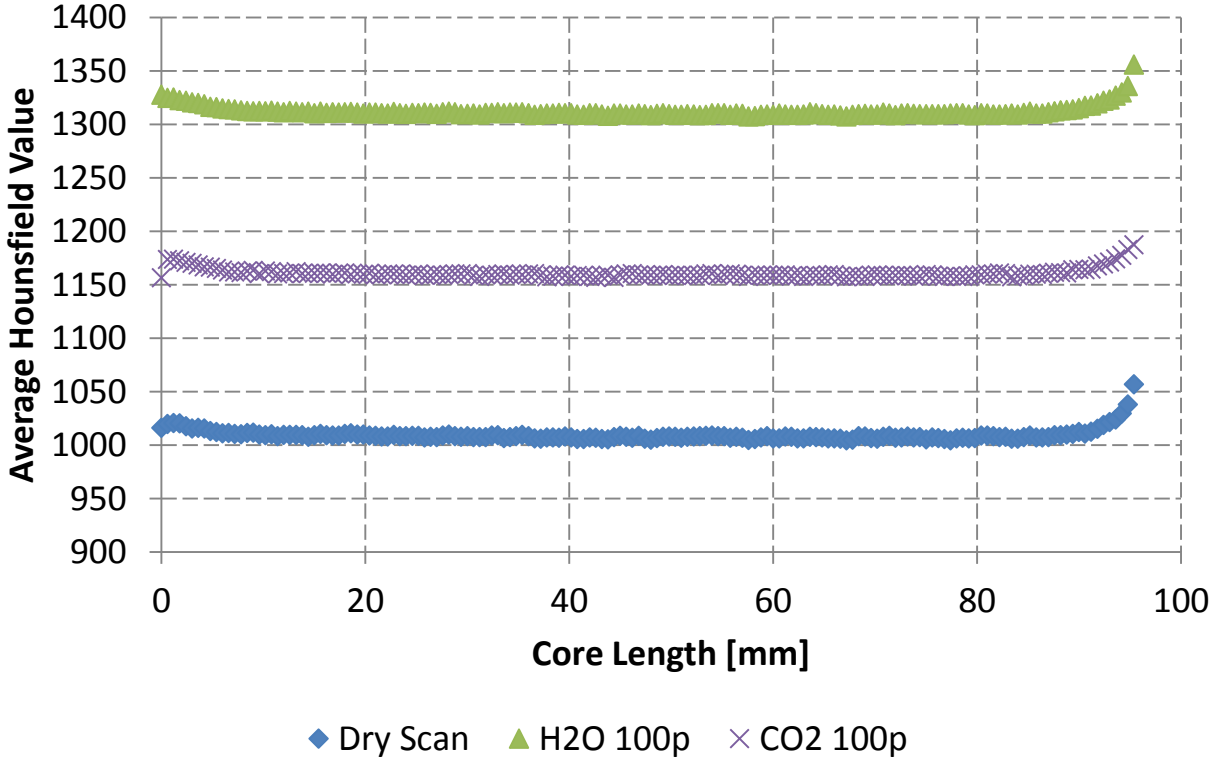


**Figure 5-3. Preliminary scans taken of the system in experiment 1 with a dry core at atmospheric pressure, 100% dead brine saturated core and 100% $CO_2$ saturated core at 90 bar pressure and 25˚C.**

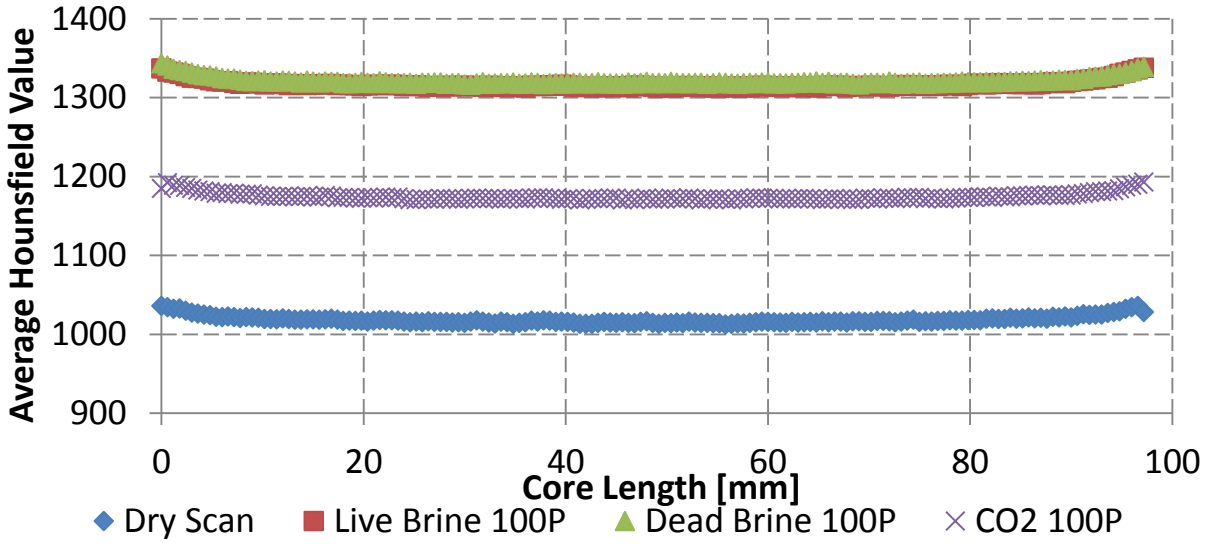


**Figure 5-4. Preliminary scans from experiment 2, including 100% live brine (brine saturated with $CO_2$), 100% dead brine, 100% $CO_2$ scans at 90 bar pressure and 25˚C and a dry scan at atmospheric pressure.**

The density difference in live fluids versus dead fluids seems to be negligible in the 100% scans as the difference in Hounsfield units seems to be the same in Figures 5-3 and 5-4. The difference between the Hounsfield values in the 100% scans in experiment 1 and 2 may be a result of a slightly different pressure because a higher pressure will result in denser liquids and higher CT values. However, this is not likely the case since the dry scans were acquired at atmospheric pressure and the difference can be seen there as well. The temperature may be the cause. A lower temperature would probably result in all of the 100% scans showing a slightly higher density, but this is hard to verify because the core temperature was not monitored in experiment 1. However, in experiment 3 (conducted at 50˚C) the dry scan is similar to the first two experiments (see Figure 5-5). The $CO_2$ has a significantly lower value in experiment 3 since it is in the supercritical phase.

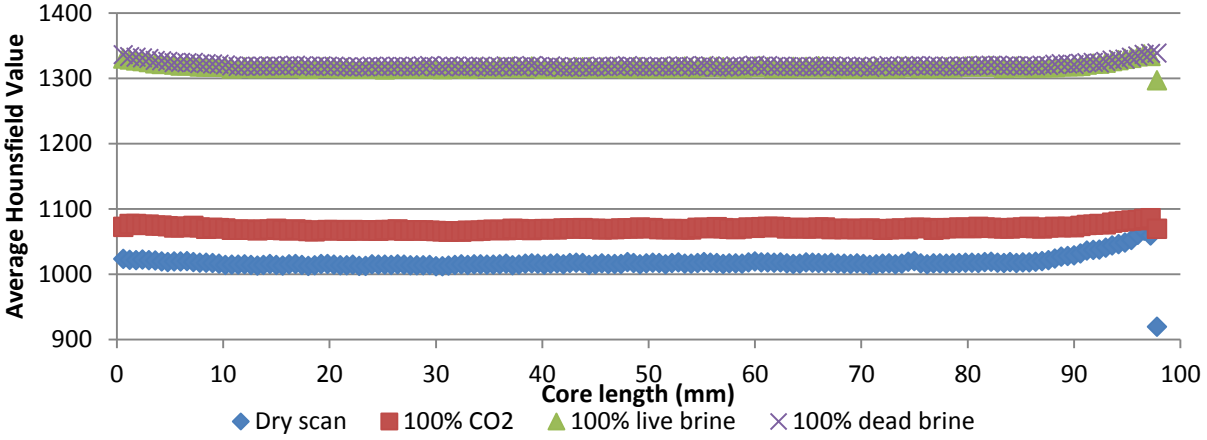


**Figure 5-5. Preliminary scans from experiment 3 with a dry core at atmospheric pressure and with a 100% dead brine saturated core, 100% live brine saturated core and 100% $CO_2$ saturated core at 90 bar and 50˚C.**

### 5.1.2. Primary drainage

Primary drainage was conducted on five sandstone cores and it can emulate the migration of a $CO_2$ plume through a saline aquifer. Fluid distribution throughout the cores and pressure data are investigated, chronologically. The behavior in the primary drainage for all the experiments will be presented and discussed prior to imbibition and secondary drainage.

The primary drainage curves have been plotted using normalized CT values obtained using the 100% scans as a reference and the saturation equation in section **3.5** to obtain water saturations as a function of core length.

Figure 5-6 shows water saturation through the length of the core after the primary drainage in experiment 1. The effects of the $CO_2$ injection are most prominent at the inlet-end of the core and are decreasing toward the outlet-end. The $CO_2$ saturation at the outlet-end of the core is very low, and almost no brine from the end has been displaced. This may be a result of capillary end-effects (Richardson et al., 1952) and is seen in all displacements in these experiments. End effects, or boundary effects, must be reckoned with in nearly all experiments dealing with multi-fluid flow and are discussed later in this section.

A better sweep was observed with increasing injection rates, as well as lower total water saturation, as seen in Figure 5-7 from experiment 2 where higher injection rates were included. A higher injection rate results in higher capillary pressure and the non-wetting $CO_2$ may then displace brine from smaller pores resulting in higher microscopic sweep efficiency.

The difference between 1ml/min and 2ml/min in the primary drainage curves for experiment 1 (Figure 5-6) and experiment 2 (Figure 5-7) may be a result of the tubing and valve not being fully operational (it seemed to be semi-plugged) in experiment 1 and therefore not delivering the desired rate. This may explain the smaller sweep and higher residual water saturation. Other factors like anomalies in the homogeneity of the cores and temperature variations may also be part of the reason for these observations. In experiment 1 the fluids were unsaturated whereas in experiment 2 the fluids were saturated with each other. It was observed in a similar experiment (Berg et al., 2013) that less brine is produced when the fluids were unsaturated than when they were saturated. However, this was negligible when more than one pore volume of $CO_2$ was injected. This may provide an explanation for the observed differences in water saturations between experiment 1 and experiment 2.

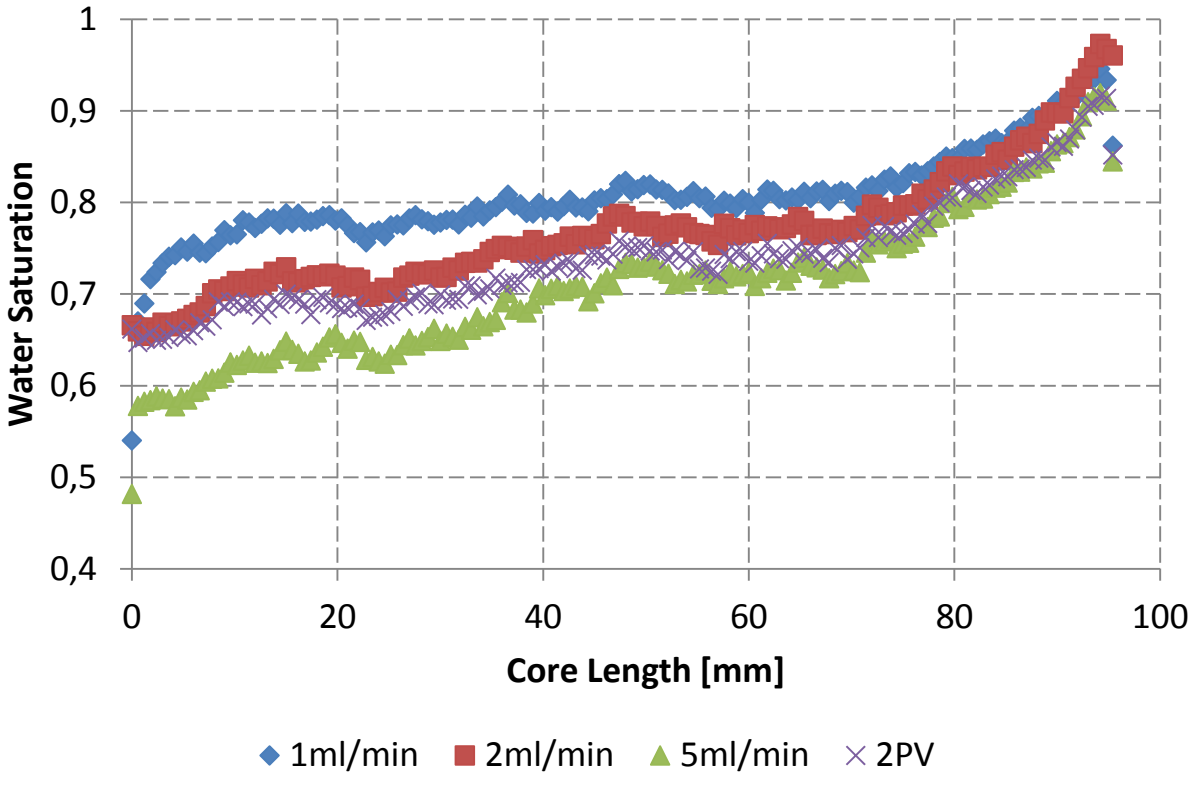


**Figure 5-6. Primary drainage water saturation vs core length for all rates in experiment 1, conducted at 25˚C and 90 bar. Unsaturated fluids were used. 2PV is the scan taken after 2 pore volumes were injected at 2ml/min.**

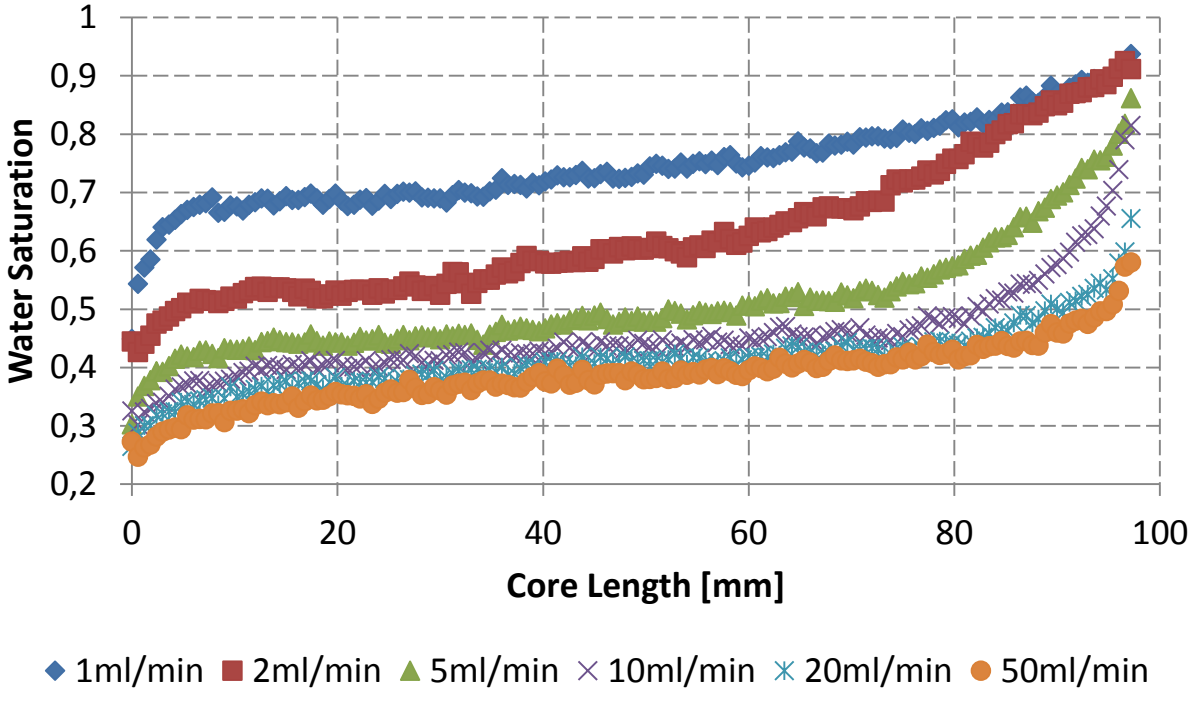


**Figure 5-7. Primary drainage water saturation vs core length for all rates in experiment 2, conducted at 25˚C and 90 bar. Saturated fluids were used.**

Figures 5-8 and 5-9 show the primary drainage from experiment 3 and experiment 4. The temperature in these experiments was 50˚C. The water saturation in these cores after primary drainage was, as seen from the figures, higher than in the first two experiments where the temperature was 25˚C. Supercritical $CO_2$ has a more gas-like viscosity and density than liquid $CO_2$ (see Table 4-1) and therefore viscous fingering may occur easier. This may result in an earlier breakthrough, less sweep and a higher remaining water fraction. From a $CO_2$ sequestration perspective this indicates that reservoir conditions where $CO_2$ is in the liquid phase are more effective than when it is supercritical. On the other hand, conditions in most storage sites are in the supercritical region for $CO_2$.

In experiment 5 (Figure 5-10) the pressure aimed for was 100 bar, resulting in higher density and viscosity of the supercritical $CO_2$ than in experiment 3 and 4, resulting in a lower water fraction after the drainage was finished. However, the water fraction from experiment 2 where the $CO_2$ was liquid in phase is still lower, despite the less pronounced end-effects in experiment 5. The lower residual water saturation caused by higher pressure, and thus also higher density, suggests that higher pressure is favorable for carbon storage in an open system.

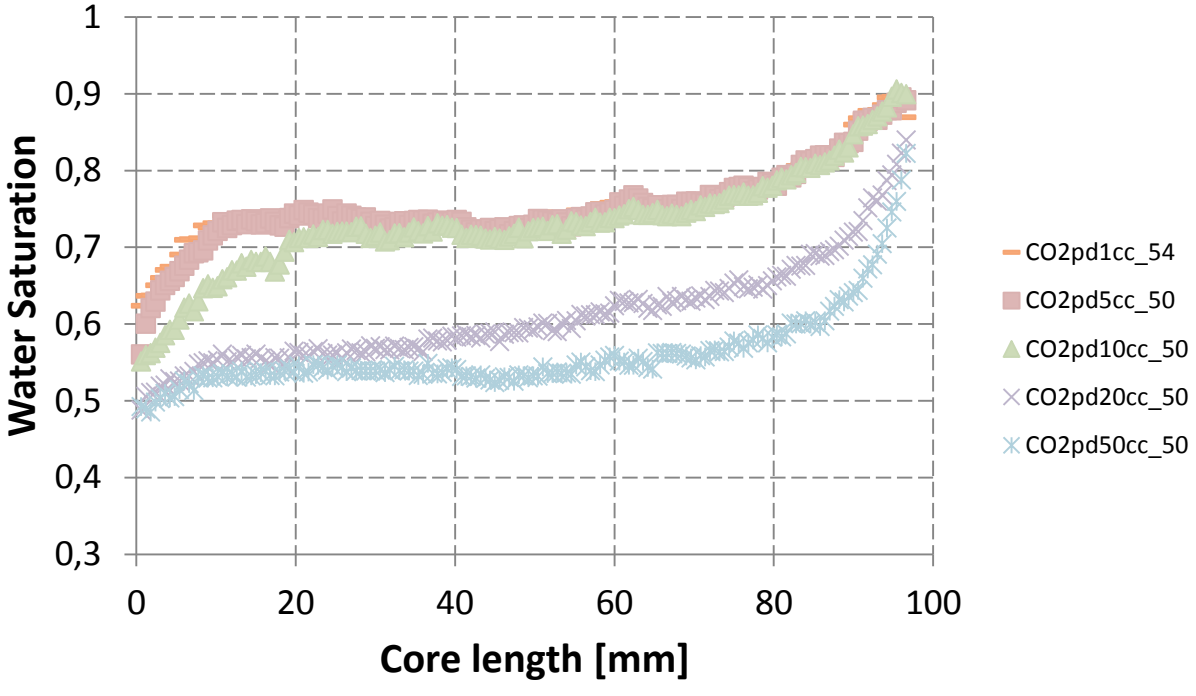


**Figure 5-8. Primary drainage water saturation vs core length for all rates in experiment 3, conducted at 50˚C and 90 bar. The fluids were saturated with each other. CO2pdXcc_Y is the name of the scan taken after Y ml of $CO_2$ was injected with a rate of X ml/min.**

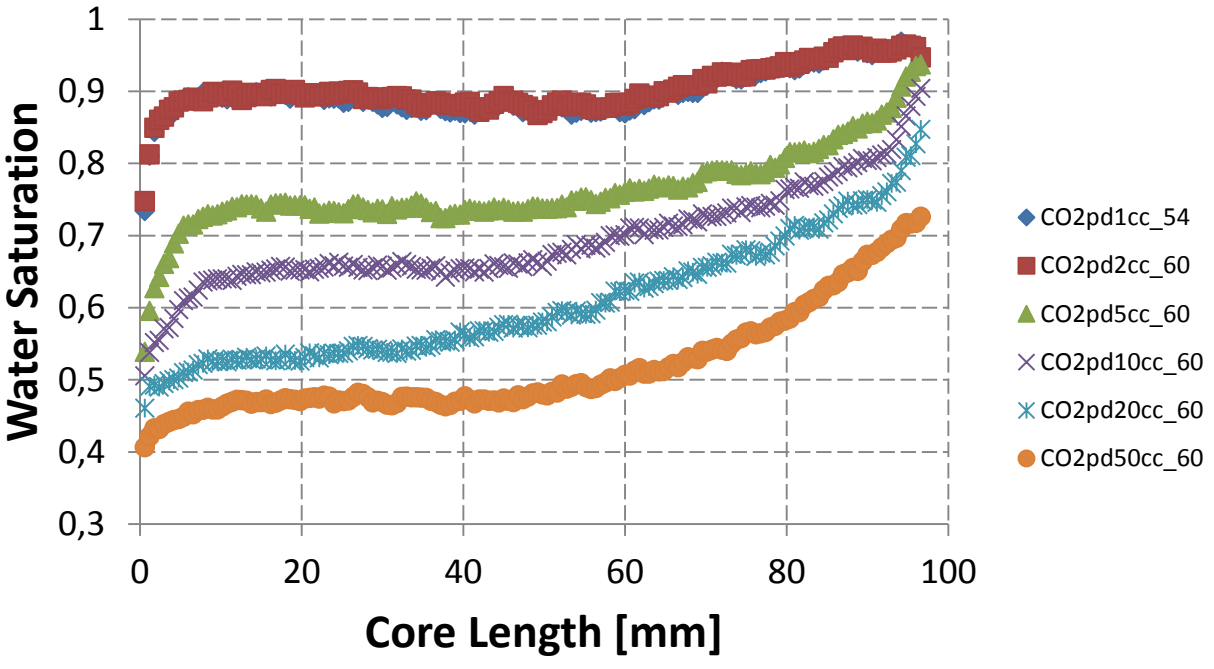


**Figure 5-9. Primary drainage water saturation vs core length for all rates in experiment 4, conducted at 50˚C and 90 bar. The fluids were saturated. CO2pdXcc_Y is the name of the scan taken after Y ml of $CO_2$ was injected with a rate of X ml/min.**

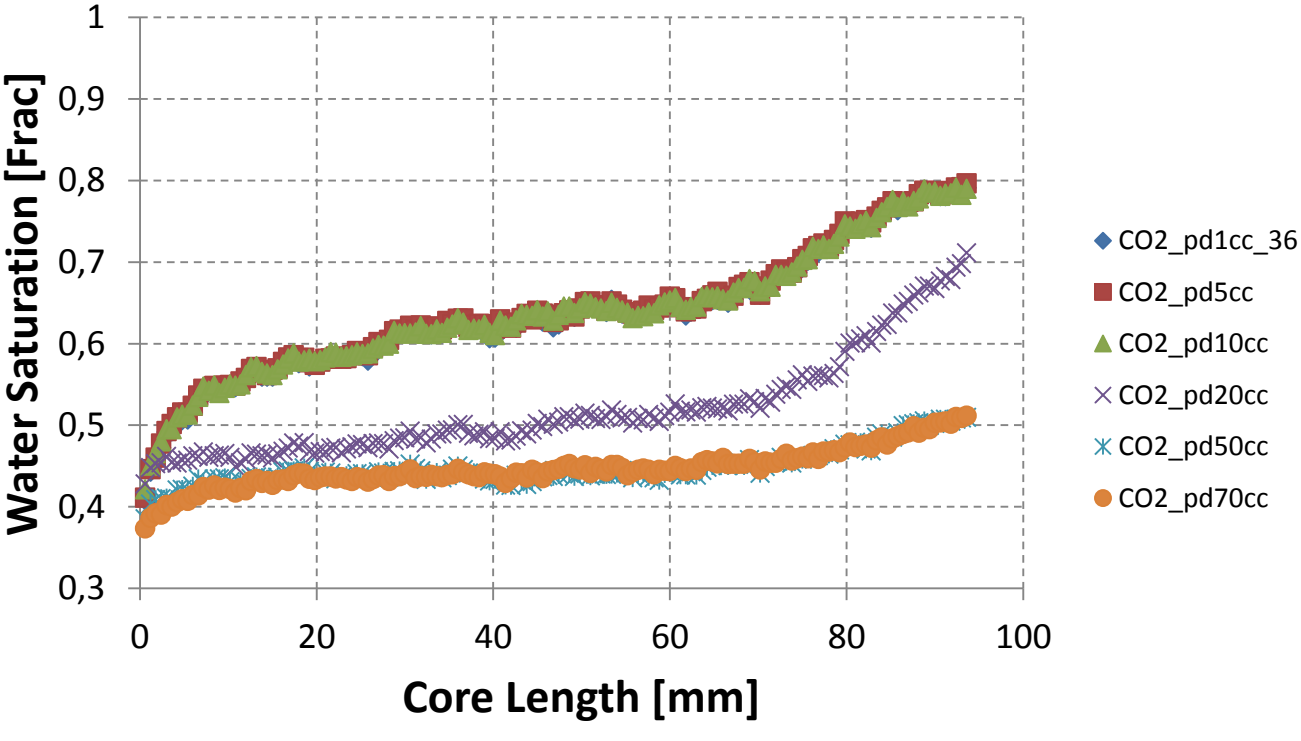


**Figure 5-10. Primary drainage water saturation vs core length for all rates in experiment 5, conducted at 50˚C and 100 bar. The fluids were saturated. CO2pdXcc_Y is the name of the scan taken after Y ml of $CO_2$ was injected with a rate of X ml/min.**

These primary drainage profiles (Figures 5-6 to 5-10) are characterized by a positive saturation gradient towards the outlet of the core. This is a result of the capillary end-effect that propagates back in the core, something that is also seen in similar experiments (Pini et al., 2011, Berg et al., 2013). At lower flow rates the outlet-end water saturation is close to one, indicating a capillary pressure close to zero. The outlet-end $CO_2$ saturations then increase with increasing rates. The end-piece used can be seen as an open receiving vessel, hence there is no capillary pressure in the small volume of water between the end-piece and the outlet-end of the core. As a result of this the capillary forces in the core tend to retain the brine (wetting phase), leading to higher brine saturation near the outlet-end of the core than throughout the remaining length of the core. This phenomenon is called the boundary effect, or capillary end effect, and it must be reckoned with in nearly all laboratory investigations dealing with multi-fluid flow (Richardson et al., 1952).

In experiment 3, 4 and 5 the saturations for the first rates seem to overlap, something that may be explained by looking at the differential pressures shown in Figures 5-11 - 5-13. These differential pressures are also needed to construct capillary pressure curves.

Figures 5-11 and 5-12 show that the differential pressure started out at a higher level than it reached at 2ml/min and almost at a similar level reached at 5ml/min. This may explain why the post primary drainage water saturations for rates 1ml/min, 2ml/min and 5ml/min almost completely overlap each other. The differential pressure seems to be the main driving force of the displacement. From a carbon dioxide storage point of view this suggests that a higher differential pressure during $CO_2$ injection is desirable as long as injection or reservoir pressures do not exceed limitations for geomechanical stability.

The differential pressures observed in experiment 3 and 4 (Figures 5-11 and 5-12) are very unstable due to the production pump being set to keep constant pressure, hence adjusting the rate continuously. Thus the production pressure fluctuates and the differential pressure follows.

Figure 5-13 shows the differential pressure from experiment 5 where the production pump was set to retract with a constant rate and the rate was adjusted manually to maintain 100 bar production and injection pressure. Both pumps were adjusted and the anomalies seen at the first injection rate correspond well with the production pump being set to retract at rates up to 15ml/min, creating a differential pressure of up to around 0.7psi (0.05 bar). This resulted in the primary drainage water saturation curves for 1ml/min, 5ml/min and 10ml/min overlapping each other. This seems to have made flow channels for the $CO_2$ leading to a differential pressure lower than for 1ml/min before the anomalies for all rates lower than 20ml/min.

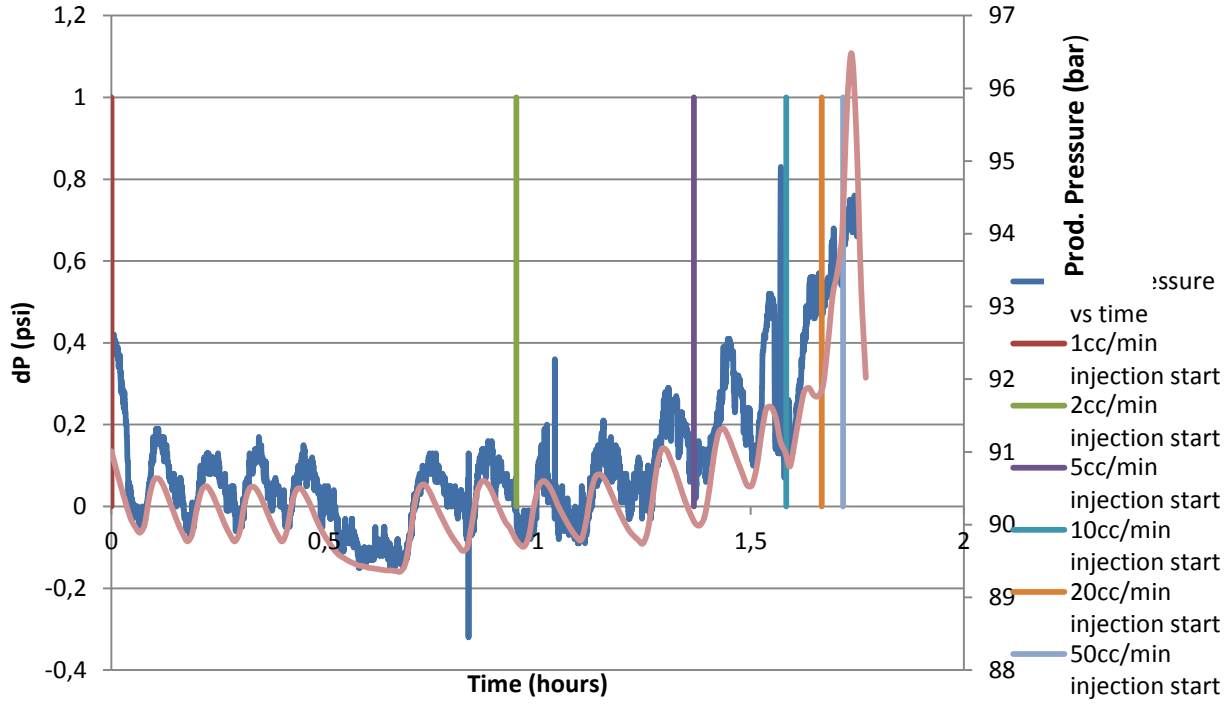


**Figure 5-11. Differential and production pressure for the primary drainage in experiment 3. The colored bars indicate the point in time when the rate is increased.**

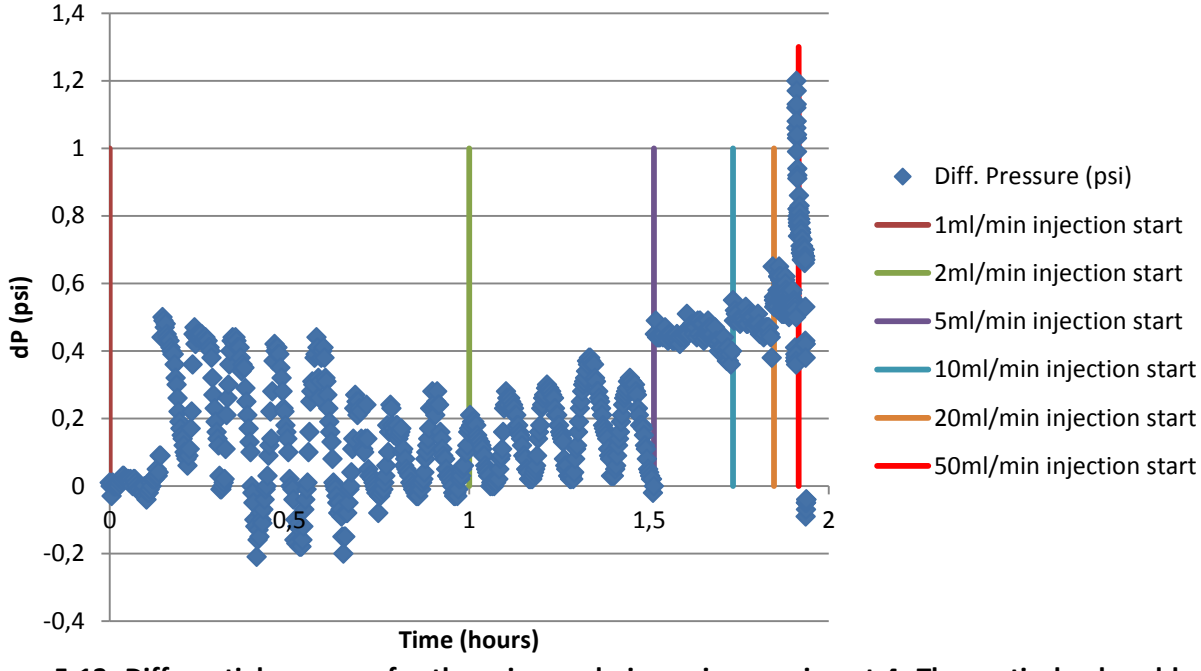


**Figure 5-12. Differential pressure for the primary drainage in experiment 4. The vertical colored bars indicate the point in time when the rate is increased.**

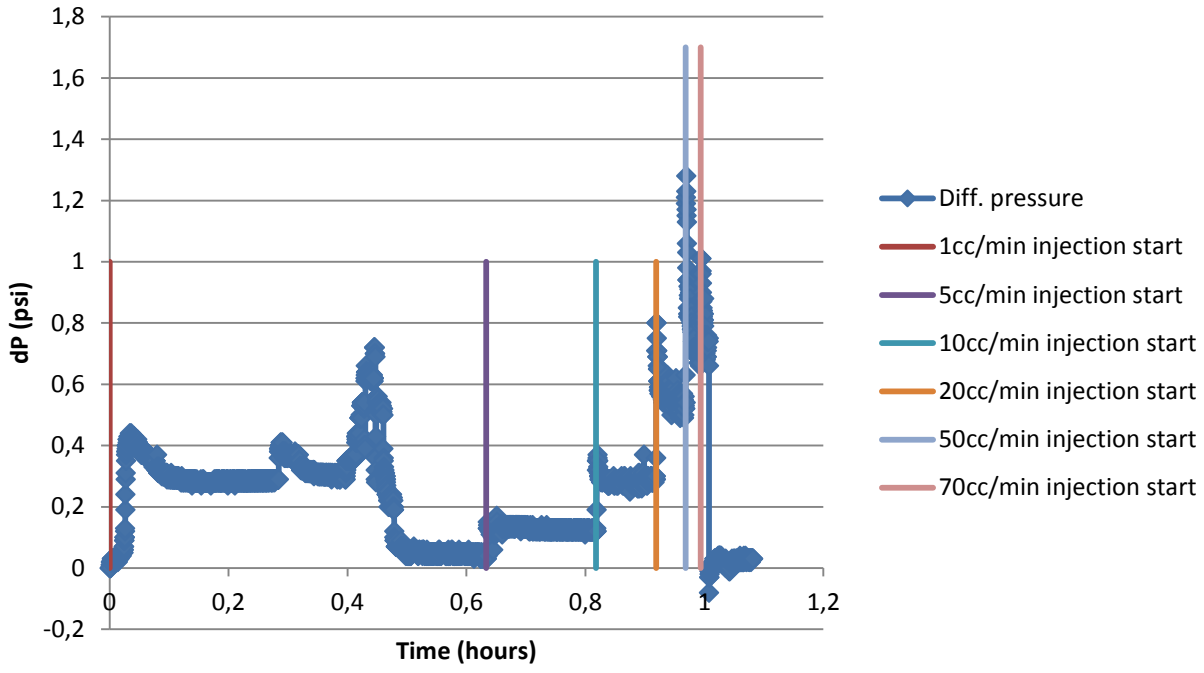


**Figure 5-13. Differential pressure for the primary drainage in experiment 5. The colored bars indicate the point in time when the rate is increased.**

Although the system was functioning well, it was a recurring challenge that the absolute pressure was difficult to maintain stable at desired value. As seen in Figure 5-11 fluctuations in the absolute pressure seem to result in fluctuations in the differential pressure. The highest differential pressure in experiment 5 occurs at 50ml/min and is around 1.3psi, or 0.09 bar. No more water was displaced when the rate was increased to 70ml/min, as seen in Figure 5-10.

Figure 5-14 shows the manually logged differential pressure of experiment 2, conducted at conditions where $CO_2$ is in a liquid phase. Experiment 2 exhibits the lowest water saturation after primary drainage, something that correlates with the highest differential pressure of all the experiments, 1.52psi. This is, as expected in such high-permeable rock, a low differential pressure and corresponds to 0.1 bar.

The production pump in experiment 2 was set to keep constant pressure at 90 bar. The reason for the differential pressure seemingly being more stable may be that the experiment was conducted at room temperature. This eliminates problems with expansion of the liquids due to temperature changes and indicates that a better isolated system in the experiments conducted at 50˚C could have kept drainage curves from overlapping each other due to the highest differential pressures being reached prior to the highest injection rates.

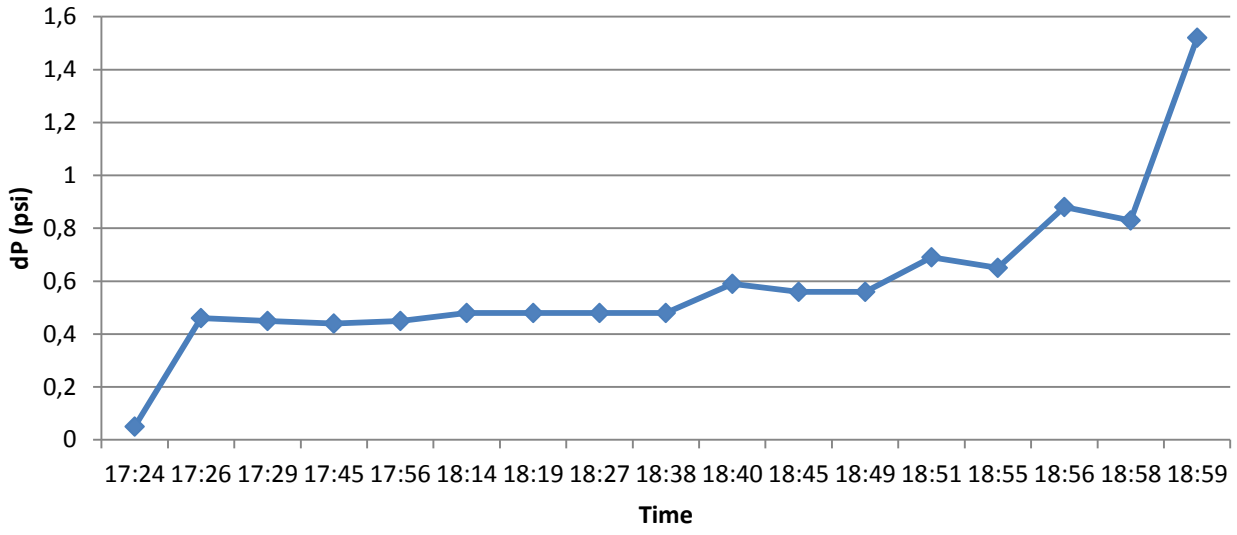


**Figure 5-14. Differential pressure for the primary drainage in experiment 2.**

### 5.1.3. Spontaneous imbibition

The first three experiments were conducted with no spontaneous imbibition whereas experiment 4 and 5 successfully utilized a technique to emulate the process of spontaneous imbibition on a short time scale. Slugs of brine were injected followed by $CO_2$ with decreasing rates. This technique supplies the rock with brine for the imbibition and the $CO_2$ distributes it throughout the core, thus speeding up the process. As the $CO_2$ injection ceases the brine is allowed to imbibe spontaneously into the rock. The $CO_2$ rates were lower in experiment 4 than in experiment 5 allowing more brine to spontaneously imbibe into the porous material, as seen in Figure 5-15 and Figure 5-16, respectively. In experiment 4 a water saturation fraction averaging at 0.66 throughout the length of the core was reached in the spontaneous imbibition after decreasing the $CO_2$ flow rate to 1ml/min, while only reaching an average water saturation fraction of 0.50 in experiment 5 where the lowest $CO_2$ rate was 15ml/min.

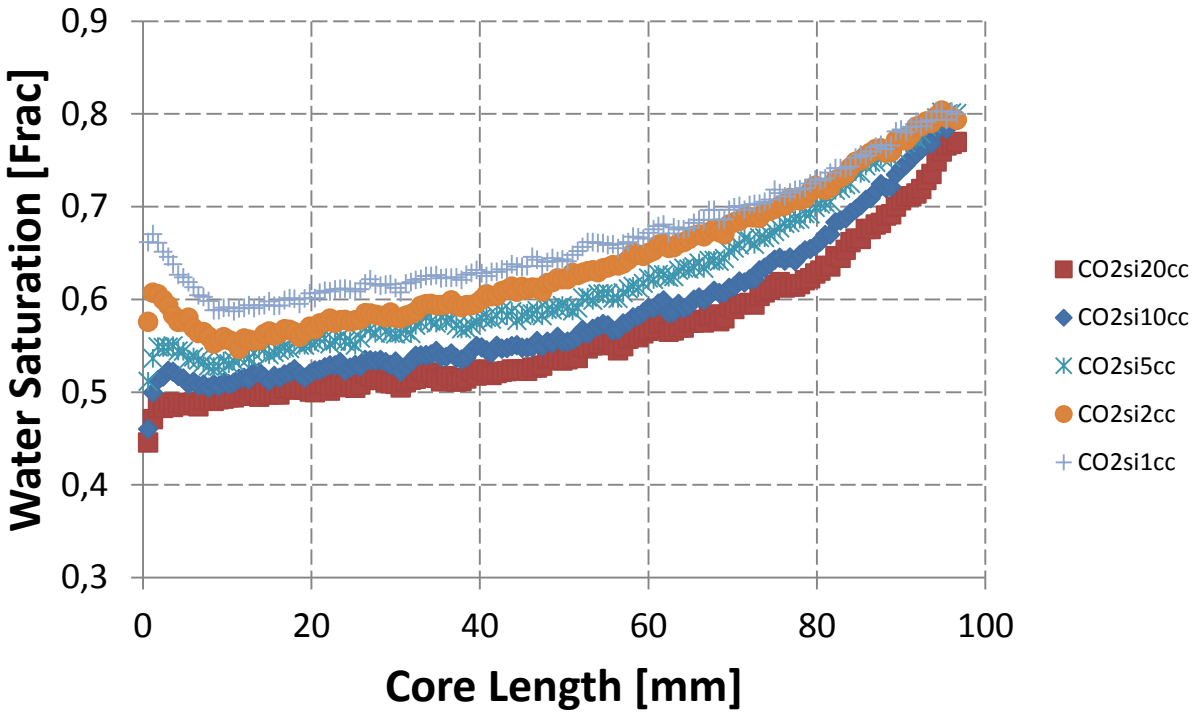


**Figure 5-15. Water saturation vs core length for the spontaneous imbibition in experiment 4, conducted at 50˚C and 90 bar. The fluids were saturated. CO2siXcc is the name of the scan taken after a brine slug followed by $CO_2$ with a rate of X ml/min was injected.**

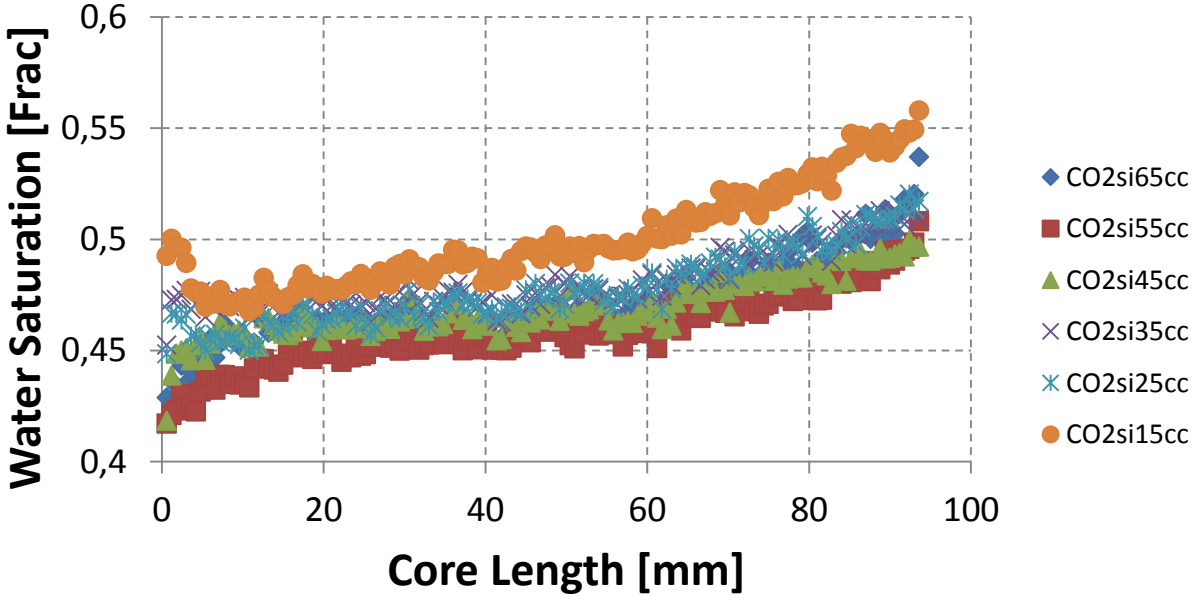


**Figure 5-16. Water saturation vs core length for the spontaneous imbibition in experiment 5, conducted at 50˚C and 100 bar. The fluids were saturated. CO2siXcc is the name of the scan taken after a brine slug followed by $CO_2$ with a rate of X ml/min was injected.**

As the $CO_2$ rate decreases, the differential pressure also decreases and more brine imbibes into the Bentheim core. Figure 5-17 shows the differential pressure for the spontaneous imbibition in experiment 5. The negative peaks is a result of the injection and production pump rates being adjusted manually which is something that should be improved in future experiments. The smaller peaks between the high peaks are the water slug injections. It can be seen from Figure 5-17 and Figure 5-16 that the second highest $CO_2$ injection rate (55ml/min) generates the highest differential pressure and thus lower water saturation than the highest $CO_2$ injection rate (65ml/min).

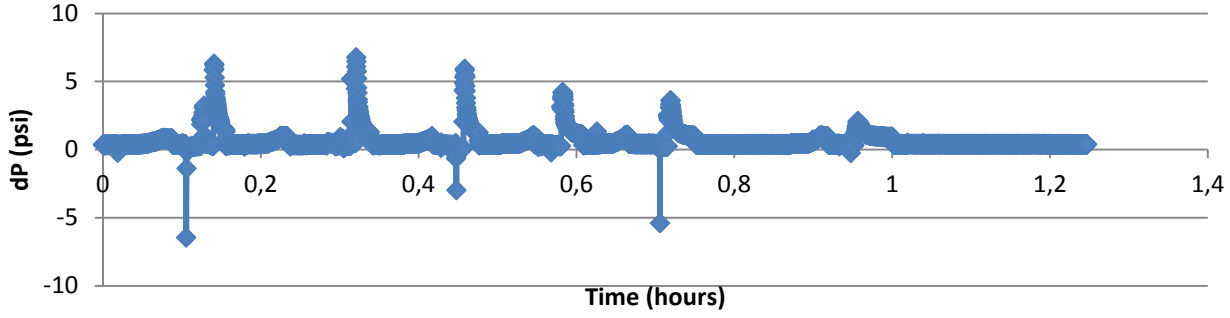


**Figure 5-17. Differential pressure for the spontaneous imbibition in experiment 5. The tallest peaks correspond with the injection of the $CO_2$ slugs and the smaller ones in between correspond with injection of the brine slugs.**

### 5.1.4. Forced imbibition

A forced imbibition was carried out for all of the experiments by injecting brine with increasing rates into the cores. This displacement process emulates the trailing edge of an advancing $CO_2$ plume migrating through an aquifer or artificial water injection after $CO_2$ injection. The residual $CO_2$ saturation after forced imbibition is of particular interest from a $CO_2$ storage point of view as it provides quantitative information about the storage capacity of a $CO_2$-brine-sandstone system.

For all rates of the forced imbibition seen in Figure 5-18 the water saturation at the inlet-end of the core is close to 100%. The water-wet Bentheim sandstone has a very low residual $CO_2$ saturation in this experiment, and a decrease can be seen with increasing rates of water injection. The low residual $CO_2$ saturation is probably caused by not being able to inject $CO_2$ at high rates in the primary drainage (due to the problems experienced with the tubing) and therefore having displaced less water than expected. In addition to this the fluids were unsaturated and therefore a mass transfer between the fluids may occur. Residual $CO_2$ may go into solution with the brine during the imbibition; hence more $CO_2$ will be flushed out with the brine. Had the brine been saturated, more snapped off $CO_2$ bubbles might have remained as residually trapped $CO_2$.

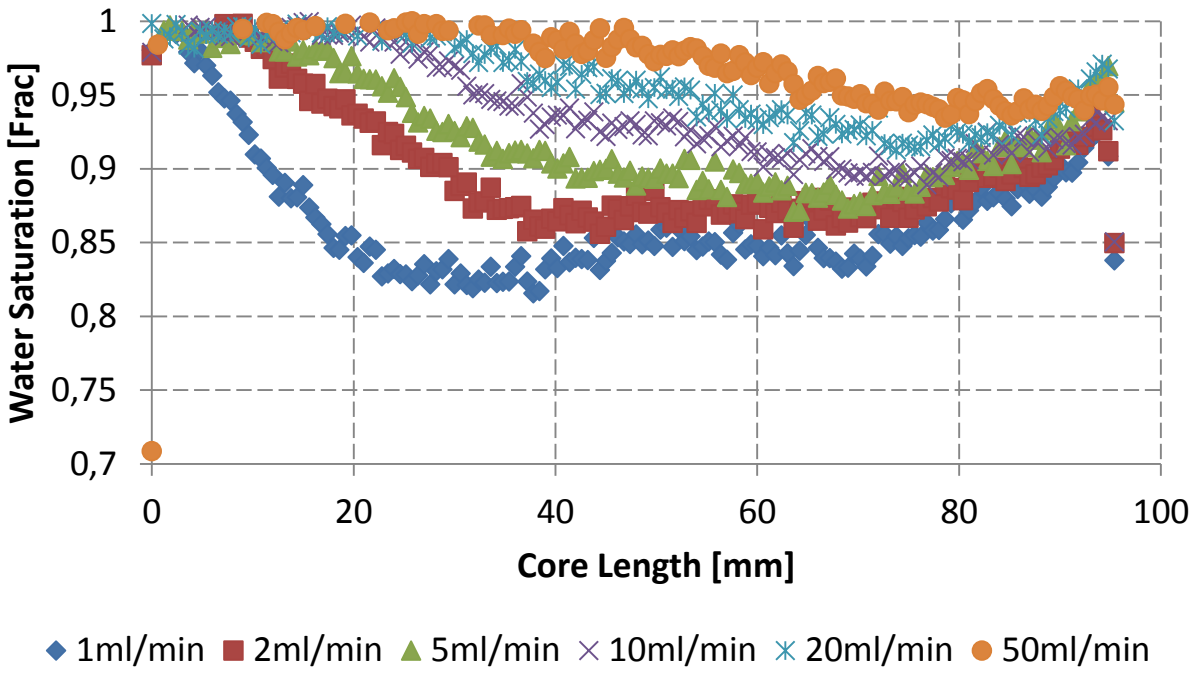


**Figure 5-18. Water saturation vs core length for all rates of the forced imbibition in experiment 1, conducted with unsaturated fluids at 25˚C and 90 bar.**

From Figure 5-19 it is observed that increasing the brine flow rate mostly impacts the water saturation in the first and middle parts of the length of the core, but less towards the outlet end. When brine is injected at the face of the core the sweep there increases with increasing rate and as it displaces $CO_2$ in the core it may run into established flow channels and the sweep may decrease over the length of the core. Also, capillary end effects are likely to have an impact.

Experiment 2 (Figure 5-19) shows the highest residual $CO_2$ saturation of all the experiments after the imbibition, averaging at 21.9% throughout the core. This may be explained by the $CO_2$ being in a liquid phase: Liquid $CO_2$ is more dense and viscous than supercritical $CO_2$ and thus it is less mobile and may be harder to displace. The lower temperature also results in less of the fluids being dissolved in each other, resulting in a lower interfacial tension, suggesting a higher residual $CO_2$ saturation in systems where the interfacial tension is lower. Storage of carbon dioxide may be more effective in systems where the temperature is low enough for the $CO_2$ to be in a liquid phase, compared to when it is supercritical.

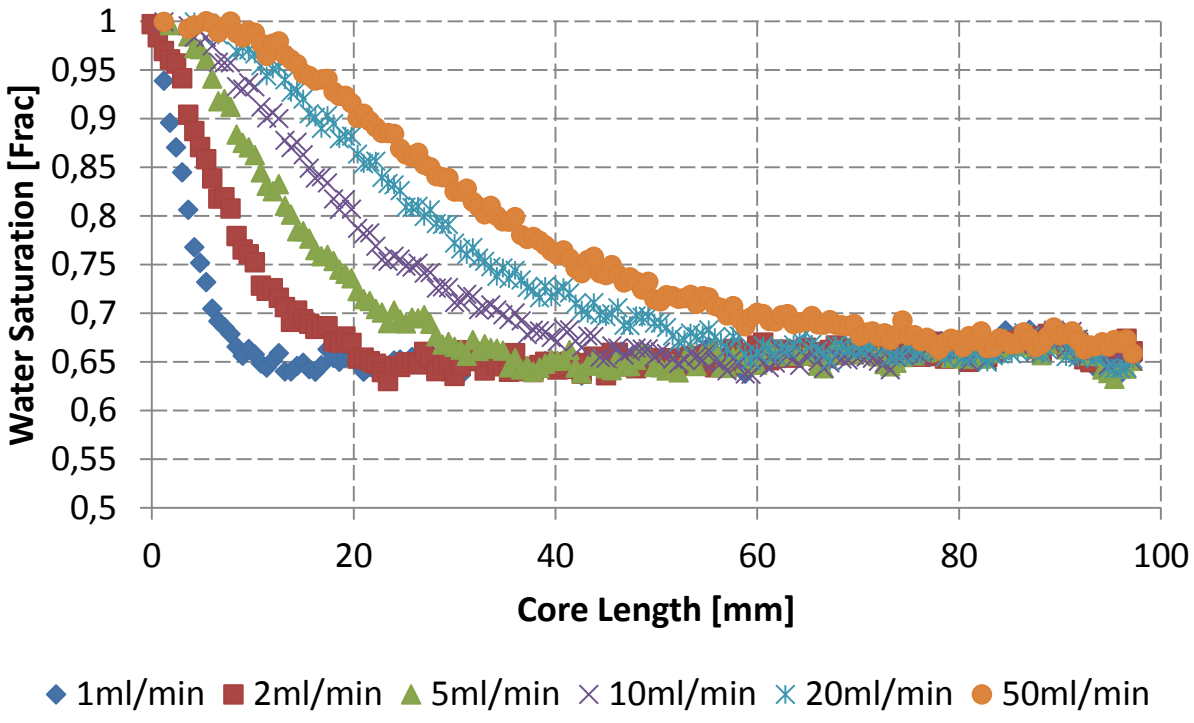


**Figure 5-19. Water saturation vs core length for all rates of the forced imbibition in experiment 2, conducted with saturated fluids at 25˚C and 90 bar.**

The residual $CO_2$ saturation after waterflooding is capillary trapped and thus relevant information with regards to storage. The water saturation is higher (lower residual $CO_2$ saturation) after the forced imbibition in the last three experiments (50˚C) - shown in Figures 5-20, 5-21 and 5-22 - than in experiment 2 (25˚C) (Figure 5-19). The lower viscosity and density of the supercritical $CO_2$, as well as the abovementioned higher interfacial tension between the two fluids, may make it easier for the brine to displace it than to displace liquid $CO_2$. Also, a system consisting of supercritical $CO_2$, brine and sandstone is suggested not to be strongly water-wet, exhibiting an increased water contact angle on quartz surfaces, thus resulting in less capillary trapping (less snap-off) and fewer small residual $CO_2$ clusters (Iglauer et al., 2011a). Figures 5-20 and 5-21 also show higher water saturation than Figure 5-22. The residual $CO_2$ saturation after imbibition in experiment 5 (Figure 5-22) averages at 15.4% throughout the core. An explanation for this may be that the pressure was higher in experiment 5 and thus the $CO_2$ was denser and more viscous, making it harder for the brine to displace it, suggesting that a higher pressure is favorable for supercritical carbon dioxide storage.

In Figure 5-22 the data set named H2OFI50cc2 represents a CT scan taken after the system was re-pressurized to 100bar after the forced imbibition. It is known, through scans taken at same saturation (see Figure 5-31), but at different pressures, that higher pressure increases fluid density and thus results in a higher water saturation. This knowledge makes it hard to explain why H2O50cc2 shows the low

water saturation that it does, leaving a calculated 26.1% average residual $CO_2$ saturation throughout the core length. This water saturation seems too high compared to the rest of the experiments and may be considered an anomaly. However, compared to literature data (Pentland, 2010) it is not unreasonably high.

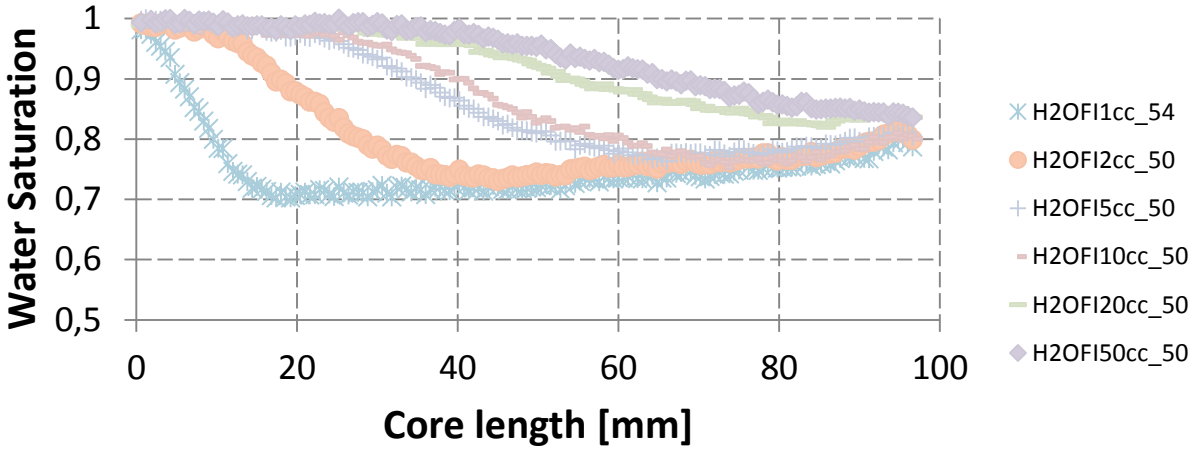


**Figure 5-20. Water saturation vs core length for all rates of the forced imbibition in experiment 3, conducted with saturated fluids at 50˚C and 90 bar. H2OFIXcc_Y is the name of the scan taken after Y ml of brine is injected with a rate of X ml/min.**

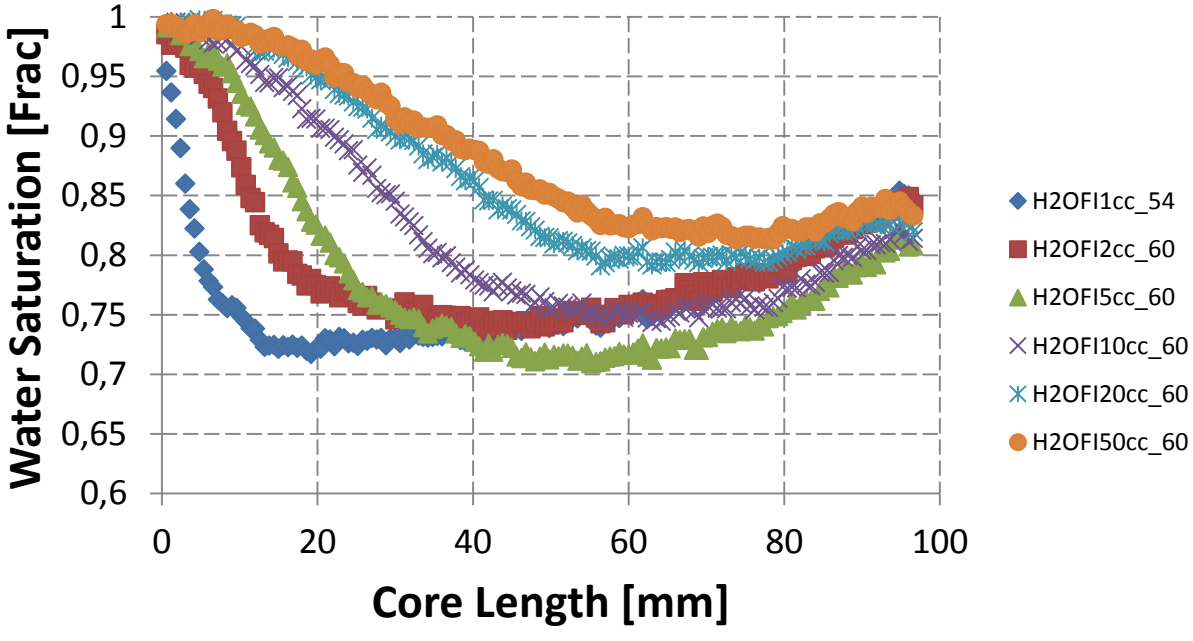


**Figure 5-21. Water saturation vs core length for the forced imbibition in experiment 4, conducted with saturated fluids at 50˚C and 90 bar. . H2OFIXcc_Y is the name of the scan taken after Y ml of brine is injected with a rate of X ml/min.**

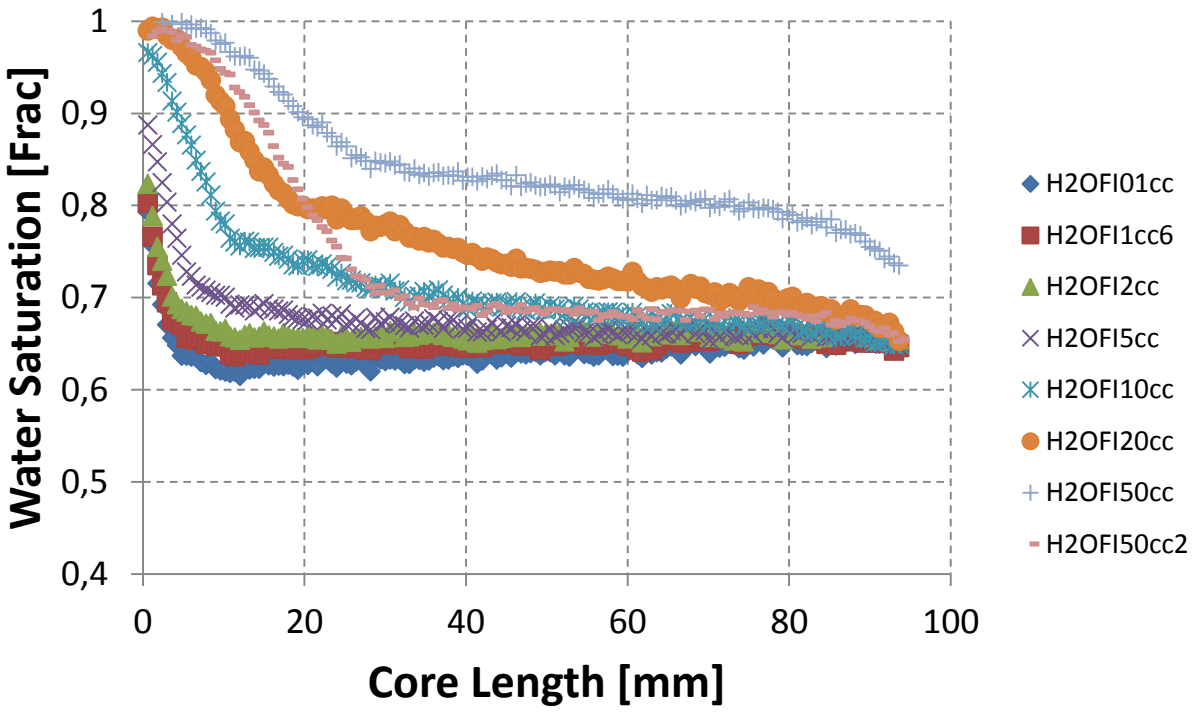


**Figure 5-22. Water saturation vs core length for the forced imbibition in experiment 5, conducted with saturated fluids at 50˚C and 100 bar. H2OFIXcc_Y is the name of the scan taken after Y ml of brine is injected with a rate of X ml/min.**

In experiment 3, 4 and 5 there were taken several scans of the 1ml/min brine injection in order to visualize the first displacements. However, it is best seen in experiment 3 (Figure 5-22) because there was no spontaneous imbibition conducted before the forced imbibition like in experiment 4 and 5.

Figures 5-23 and 5-24 show the first displacements with brine injection rate 1ml/min for experiment 3 and 4. The curves are much closer in experiment 4 than in experiment 3. In both of these experiments an increase in water saturation is observed with an increase in the amount of injected brine.

The inlet-end effect in Figure 5-23 seems to have an impact after 15ml of brine is injected. This may be a result of the water saturation needing to reach a certain level before the capillary boundary effect comes into action. However, in Figure 5-24 the end-effects are seen from the start of the injection, probably a result of the spontaneous imbibition preceding the forced imbibition creating a water filled space in the interface between the inlet end-piece and the core. These observations may prove beneficial for prediction of behavior at the trailing edge of a $CO_2$ plume and in the area near an artificial brine injection well in a geological storage site.

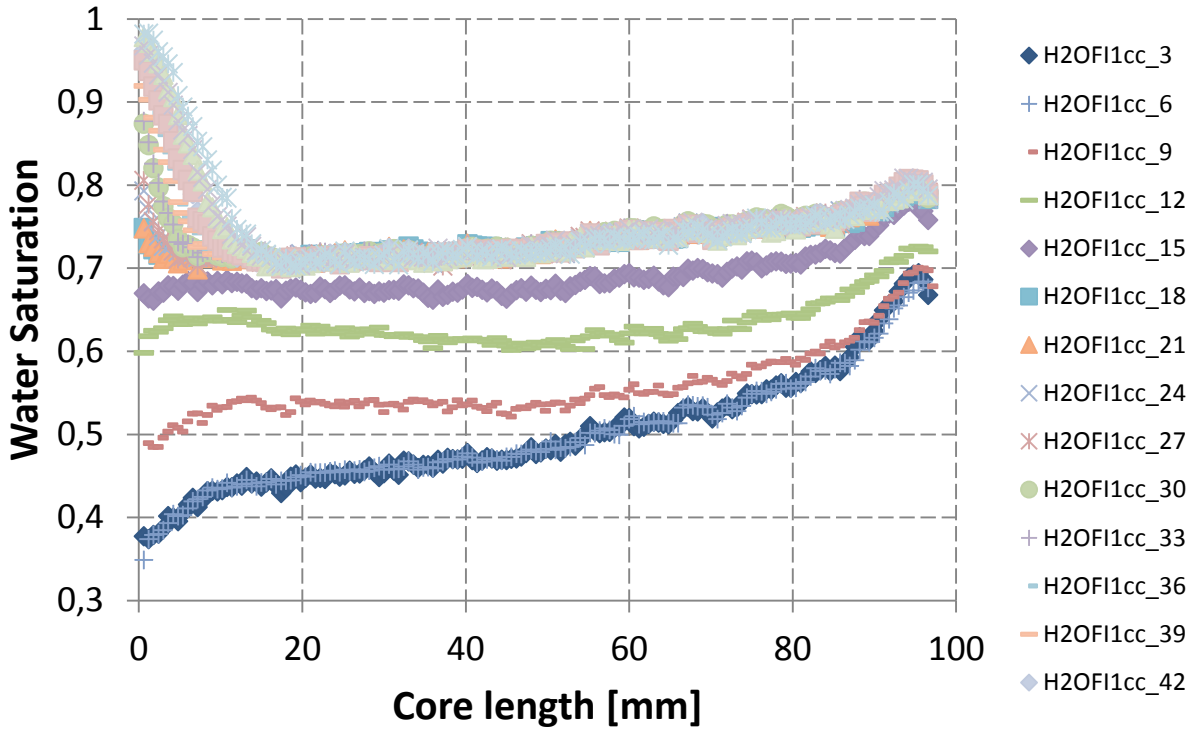


**Figure 5-23. Water saturation curves of the forced imbibition in experiment 3 for 1ml/min. H2OFI1cc_Y is the name of the scan taken after Y ml of brine is injected with a rate of 1 ml/min.**

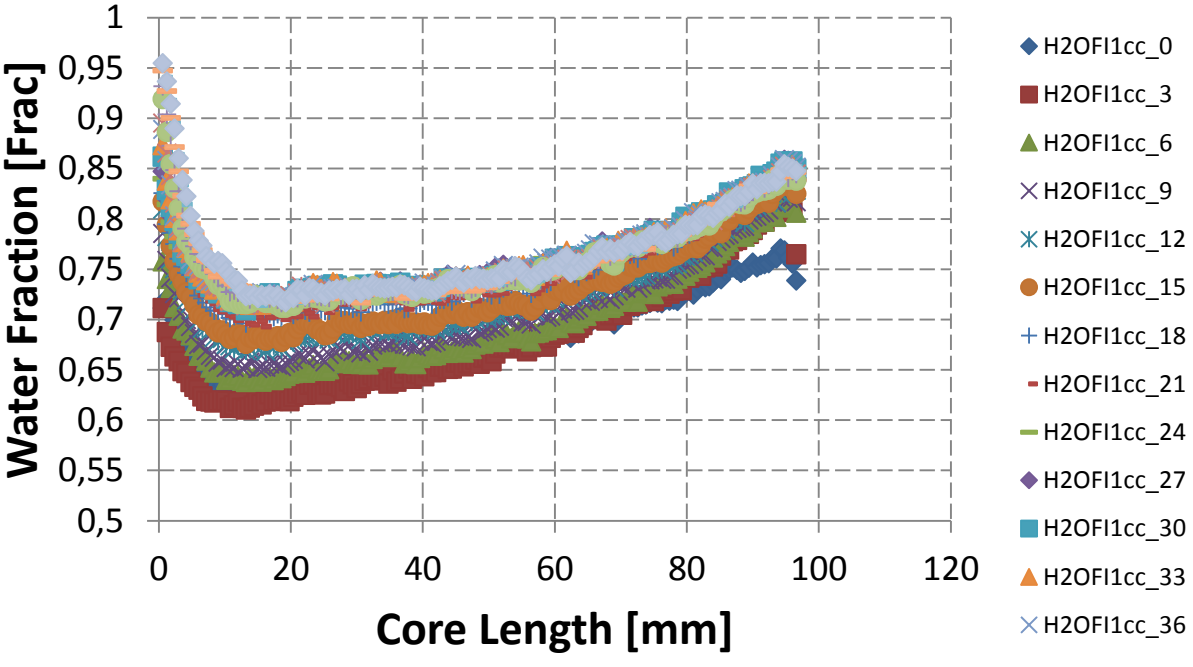


**Figure 5-24. Water saturation curves of the forced imbibition in experiment 4 for 1ml/min. H2OFI1cc_Y is the name of the scan taken after Y ml of brine is injected with a rate of 1 ml/min.**

### 5.1.5. Secondary drainage

The secondary drainage was executed for comparison with the primary drainage and may be seen as an emulation of a post brine secondary $CO_2$ injection in a saline aquifer in a geological storage site. Figures 5-26 to 5-29 show the water saturation through the core length for the secondary drainage for all rates and all experiments. Compared to the curves for primary drainage the calculated water saturations are slightly lower. This is as expected due to hysteresis effects from the primary drainage. The secondary drainage in experiment 1, 2 and 3 shows similarities to the primary drainage, most so in experiment 1. This makes sense because the conditions before the secondary drainage in experiment 1 were almost similar to the 100% water saturation that was the case before the primary drainage. These findings suggest that injecting alternating volumes of $CO_2$ and brine is beneficial for carbon dioxide storage. However, as mentioned in the literature survey in section **3.,** an interesting approach for further studies would be to co-inject $CO_2$ and brine followed by chase brine for comparison with these experiments.

In experiment 4 and 5 it seems as the secondary drainage displaced a slug of water from the inlet-end of the core 10-20 mm into the core. This may be a result of injecting $CO_2$ at a rate of 0.1ml/min prior to 1ml/min in experiment 4 and then establishing flow channels through larger pores for the remainder of the core length due to low capillary pressure. When the rates increase this phenomenon seems to disappear and the curves flatten and look more similar to the primary drainage.

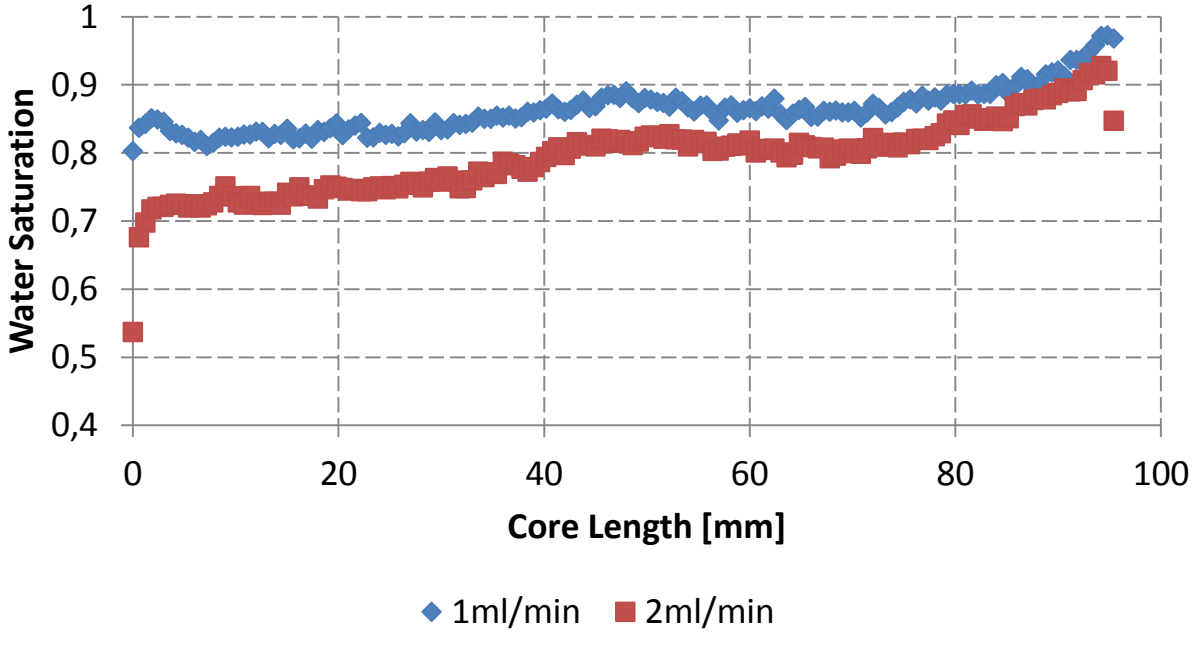


**Figure 5-25. Water saturation vs core length for the secondary drainage in experiment 1, conducted with unsaturated fluids at 25˚C and 90 bar.**

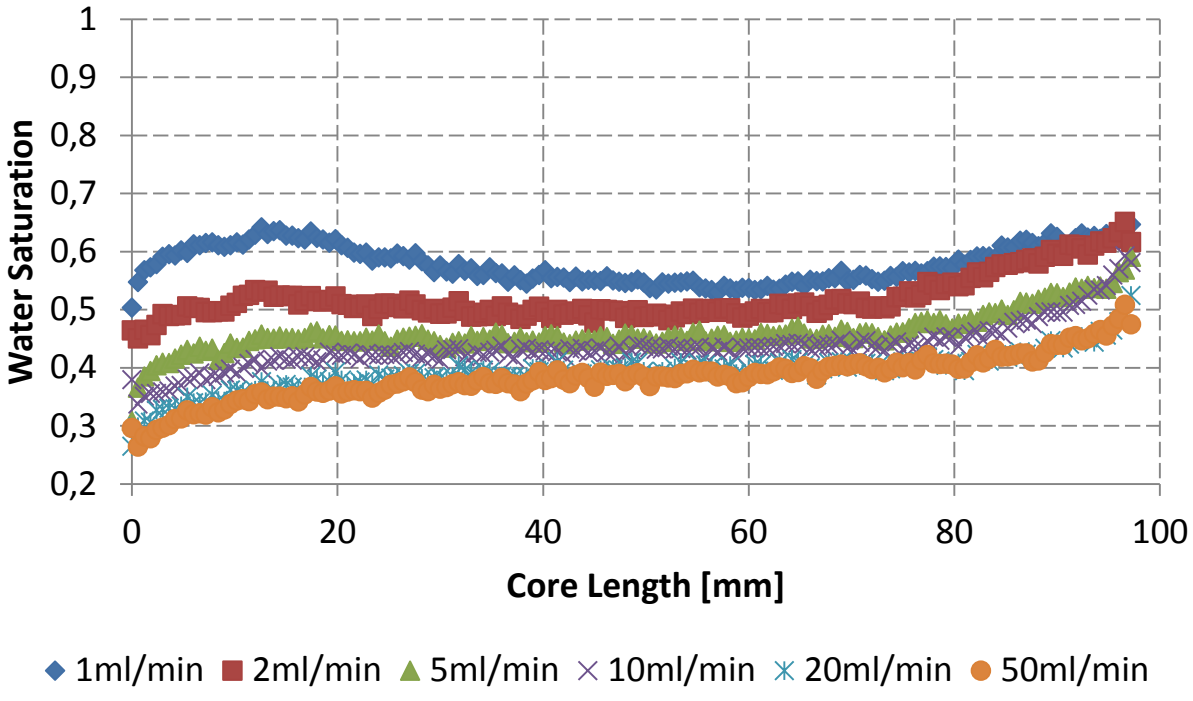


**Figure 5-26. Water saturation vs core length for the secondary drainage in experiment 2, conducted with saturated fluids at 25˚C and 90 bar.**

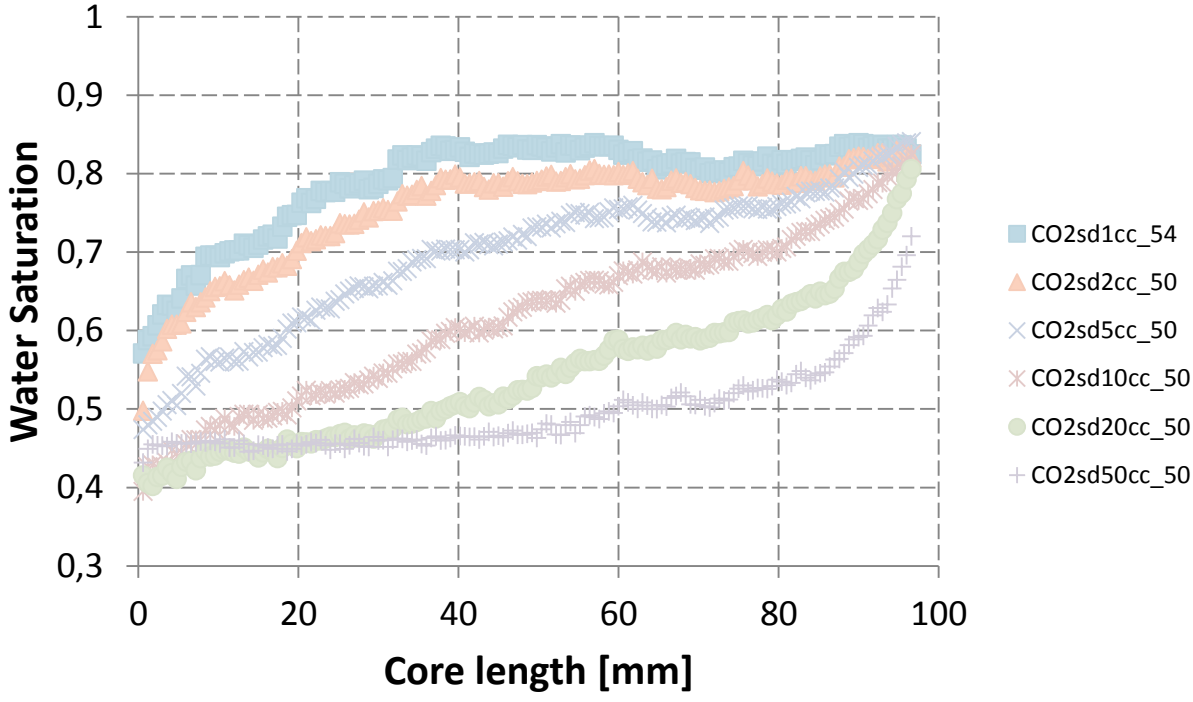


**Figure 5-27. Water saturation vs core length for the secondary drainage in experiment 3, conducted with saturated fluids at 50˚C and 90 bar. H2OsdXcc_Y is the name of the scan taken after Y ml of brine is injected with a rate of X ml/min.**

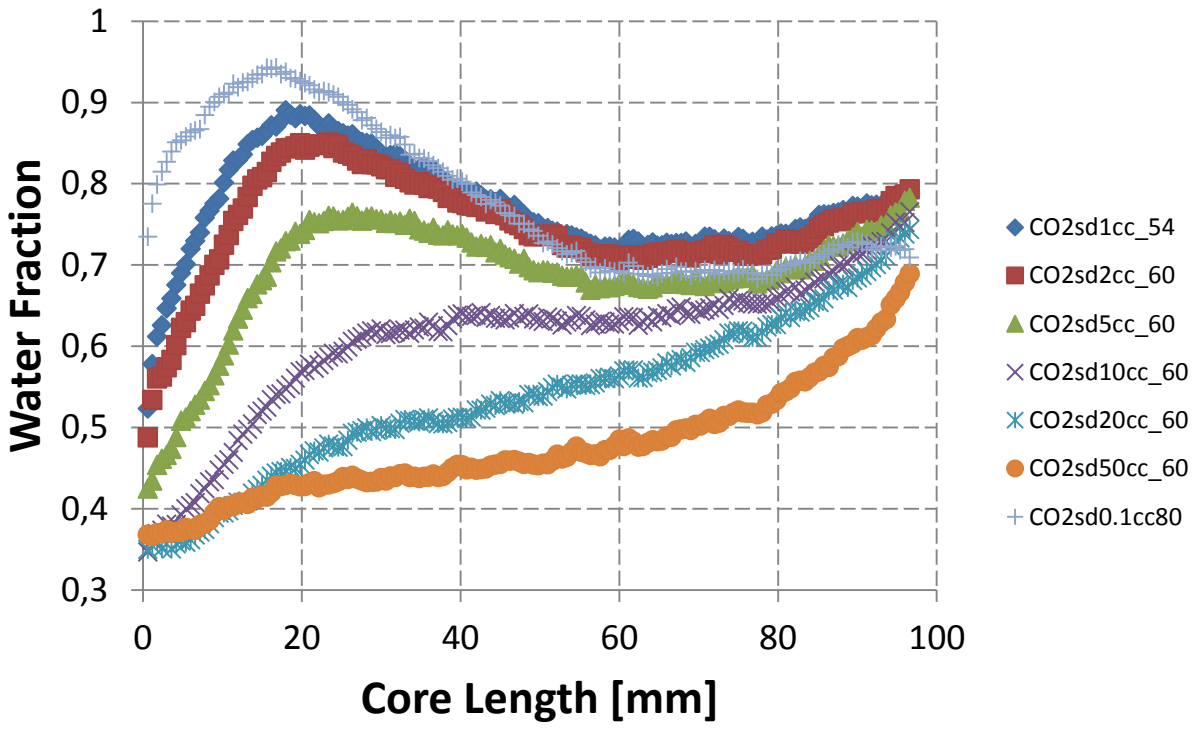


**Figure 5-28. Water saturation vs core length for the secondary drainage in experiment 4, conducted with saturated fluids at 50˚C and 90 bar. H2OsdXcc_Y is the name of the scan taken after Y ml of brine is injected with a rate of X ml/min.**

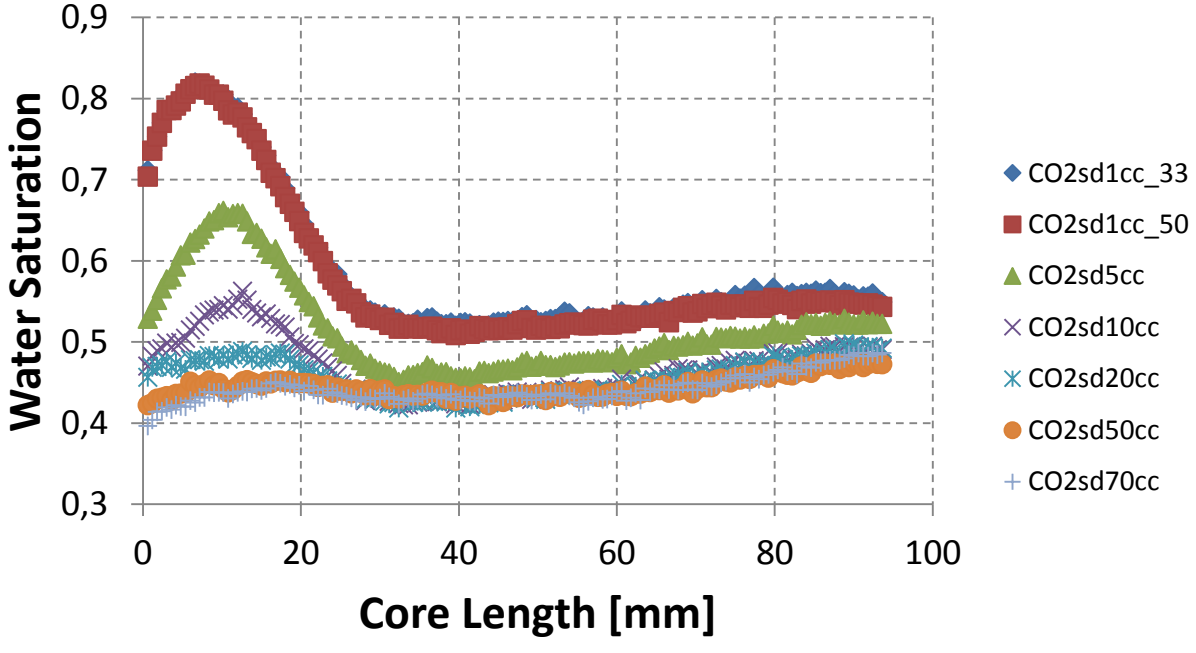


**Figure 5-29. Water saturation vs core length for the secondary drainage in experiment 5, conducted with saturated fluids at 50˚C and 100 bar. H2OsdXcc_Y is the name of the scan taken after Y ml of brine is injected with a rate of X ml/min.**

Figure 5-30 shows water saturation through the length of the core in experiment 3 for secondary drainage with rate 1ml/min. The first scan is taken before the injection started and the water saturation is therefore similar to after the forced imbibition. In experiment 4 a rate of 0.1ml/min was injected over night before the secondary drainage, hence those curves would be closer together, but still water saturation is decreasing with time for 1ml/min.

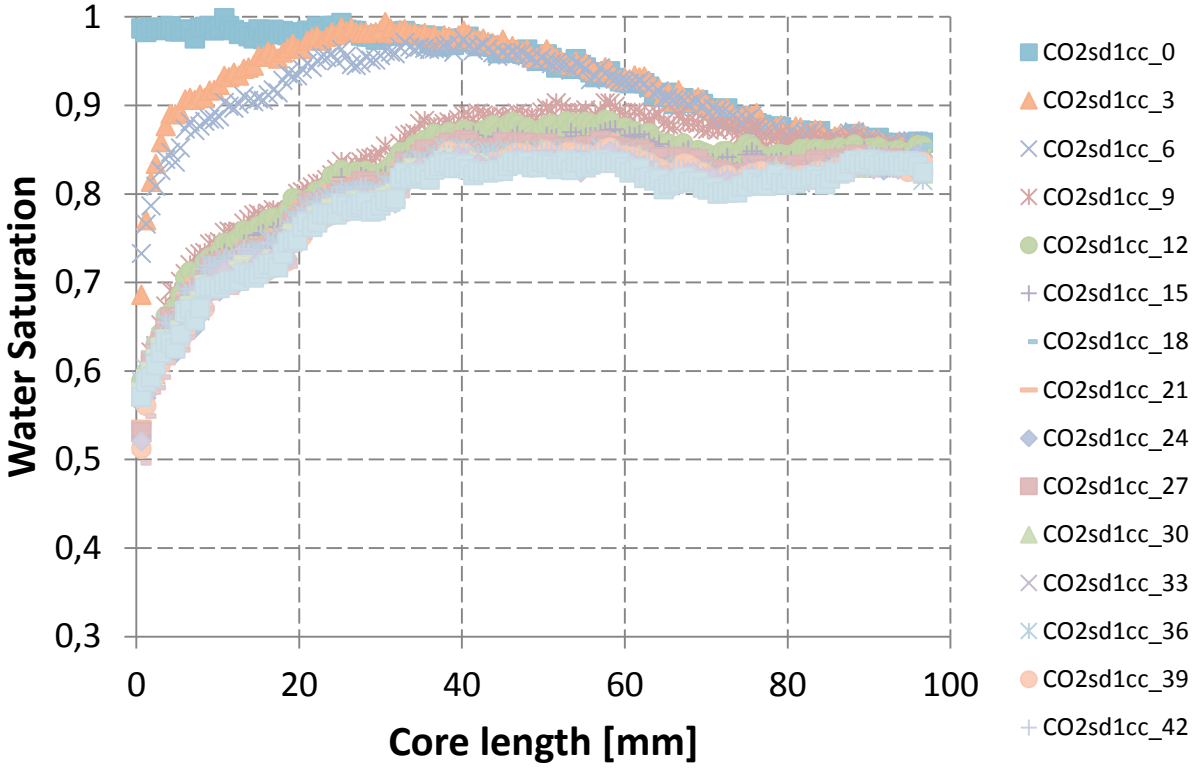


**Figure 5-30. Water saturation curves of the secondary drainage in experiment 3 for 1ml/min.**

### 5.1.6. Effect of different pressures

The absolute pressure and differential pressure seem to follow each other closely (as seen in Figure 5-11). The absolute pressure has a large effect on the CT values and in experiment 4 several scans were taken at the same saturation, but with different pressures, to see the impact of varying pressure (Figure 5-31).

The water saturation calculated from the CT values shows improperly high values when the pressure increases above the correct experimental pressure, due to an increase in density. This is most definitely a

source of uncertainty because the pressure was hard to keep stable with the equipment used in this system. The temperature also has an impact and for future works the main challenge will be to minimize these two uncertainties.

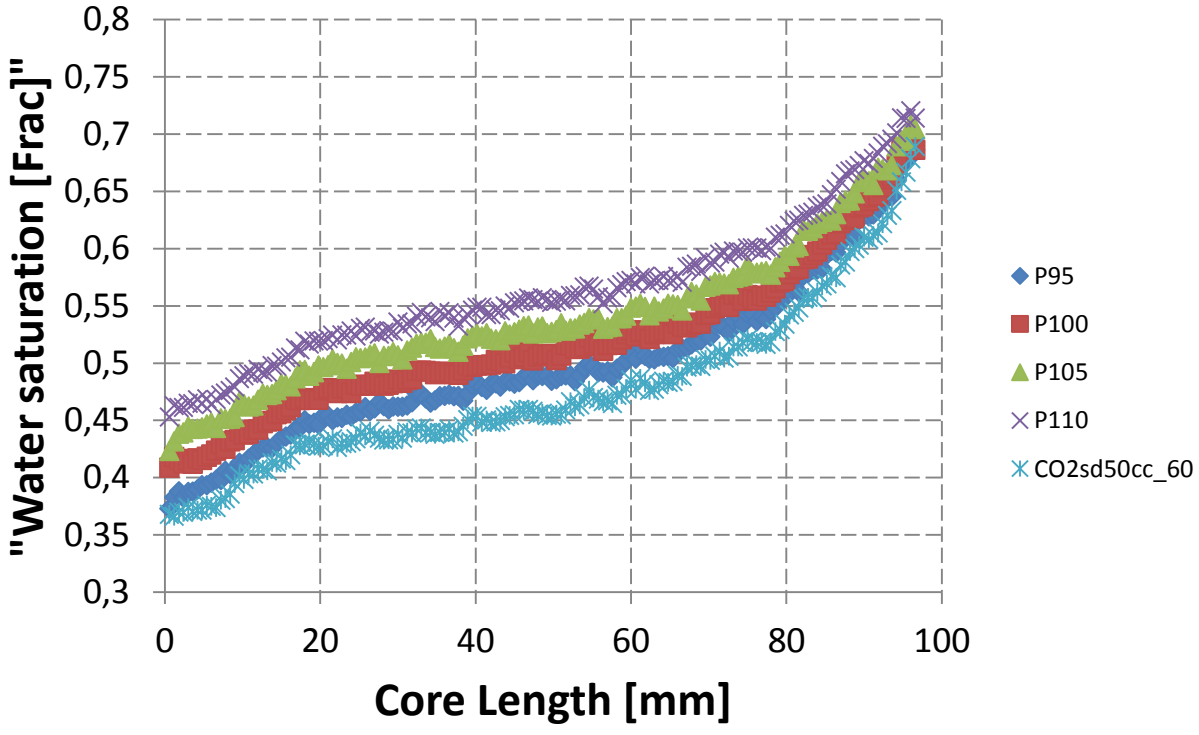


**Figure 5-31. Scans taken at different pressures, but at the same water saturation, for experiment 4. The scans show different water saturations even though the saturation is the same for all scans. The differences in pressures result in "false saturations" due to the density change in the fluids.**

### 5.1.7. Capillary pressure

Capillary pressure is an important part of understanding fluid flow in porous media and because it is traditionally a time consuming process to measure capillary pressure curves it is beneficial to investigate more efficient methods, like the one utilized in this work. Figure 5-32 shows an example of how CO2/water capillary curves can be obtained by combining the measured pressure drop across the core with the slice-averaged inlet water saturations. The drainage capillary pressure curves exhibit a broad plateau followed by a sharp increase, similar to the Berea sandstone used by Pini (2011). This is typical behavior for well-sorted rocks with narrow pore size distribution.

It is observed in similar experiments (Pini et al., 2011) that capillary pressure measured at 25˚C is consistently lower than capillary pressure measured at 50˚C, for the same saturation. This is a result of the interfacial tension (IFT) decreasing, with decreasing temperature (increasing CO2 solubility in water). Figure 5-33 shows the primary drainage curves from experiment 2 (25˚C) and experiment 4 (50˚C). These curves do not correspond exactly to aforementioned results by Pini. This may be a result of the uncertainties linked to keeping a constant absolute pressure during the displacements. However, once a specific saturation is reached the capillary pressure is higher for the 50˚C experiments. The reason the results do not match early in the drainage process may be that the differential pressure, which is the driving force of the displacements, tended to reach higher levels during the first rates as discussed in the primary drainage section.

The capillary pressure curves exhibited in Figure 5-32 and 5-33 suggests the efficacy of this novel method. Even though the results does not exactly match literature data and the unstable pressures during the experiment makes it harder to compare with mentioned data the curves were successfully obtained, providing insights and experience for future work.

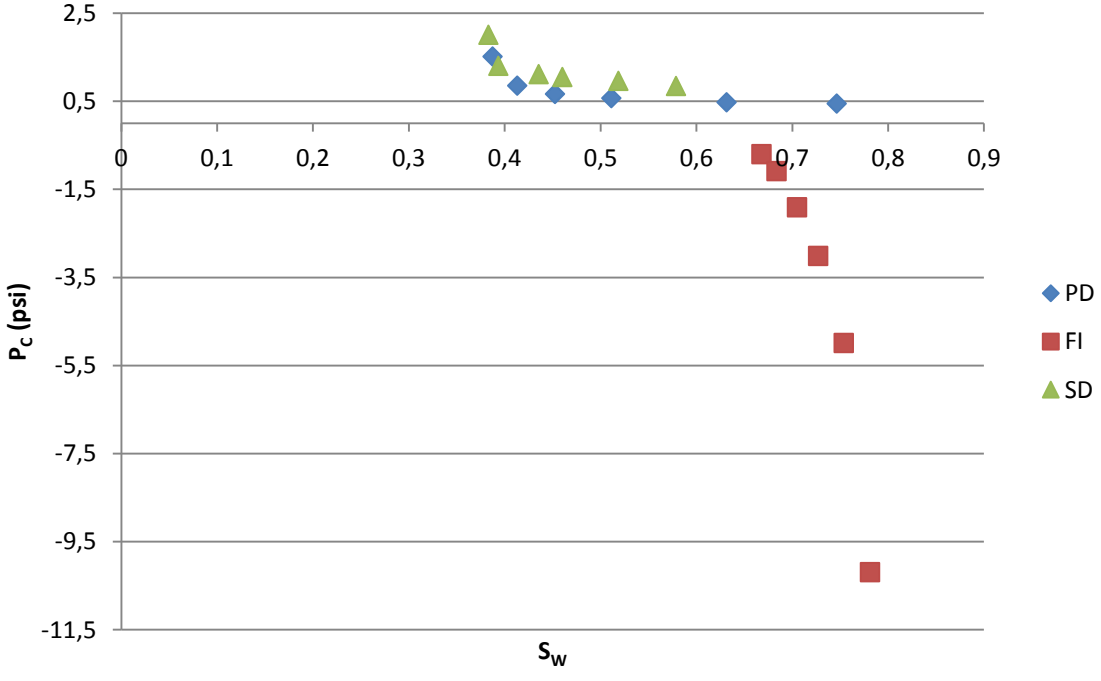


**Figure 5-32. Capillary pressure curve obtained from average differential pressure and saturation values in experiment 2. PD: primary drainage; FI: forced imbibition; SD: secondary drainage.**

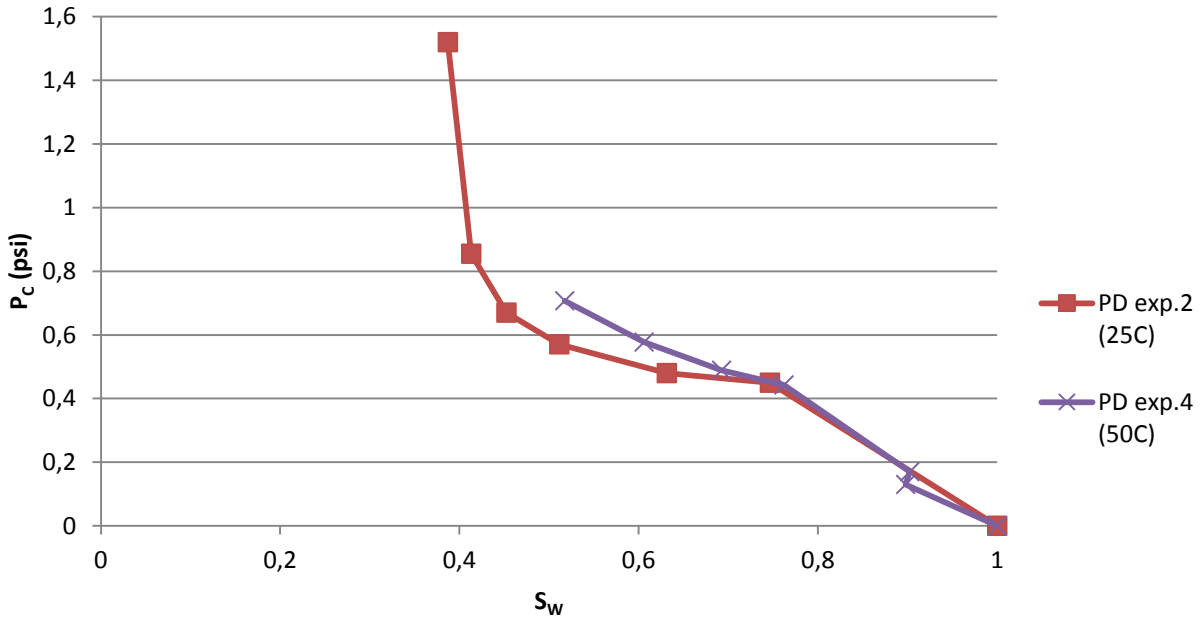


**Figure 5-33. Primary drainage capillary pressure curves for 25˚C and 50˚C from experiment 2 and 4, respectively.**

## 5.2. $CH_4$-$CO_2$ exchange at the hydrate lab

The objective in this thesis, with respect to hydrate, is to examine the process that takes place when liquid $CO_2$ is introduced to methane hydrate in porous media. Because $CO_2$ is a more stable hydrate former than methane, it will preferably liberate $CH_4$ and safely sequestrate $CO_2$, all without dissociating the hydrate. There are three ways in which $CO_2$ can be sequestrated using this method: (1) Replacing CH4 as the guest molecule in the hydrate, (2) Forming $CO_2$ hydrate with the excess water and (3) Remaining in the core as free $CO_2$. Alternative (1) and (2) are considered as safe long-term storage of $CO_2$ and alternative (3) is depending on other processes - like capillary trapping, solubility trapping, mineral trapping and stratigraphic trapping – for safe storage. For this thesis a Bentheim sandstone core, CO2_32, with readily formed methane hydrate was used for an exchange experiment. Figure 5-34 shows methane consumption during the hydrate formation. The curve has a typical shape with a high methane consumption rate after a low enough temperature for hydrate to form is reached. The pump was set to keep constant pressure, however, it stopped during the formation and the consumed volume of methane had to be corrected for. The formation was performed by Marie Dahle Høyland for her master thesis (Høyland, 2014).

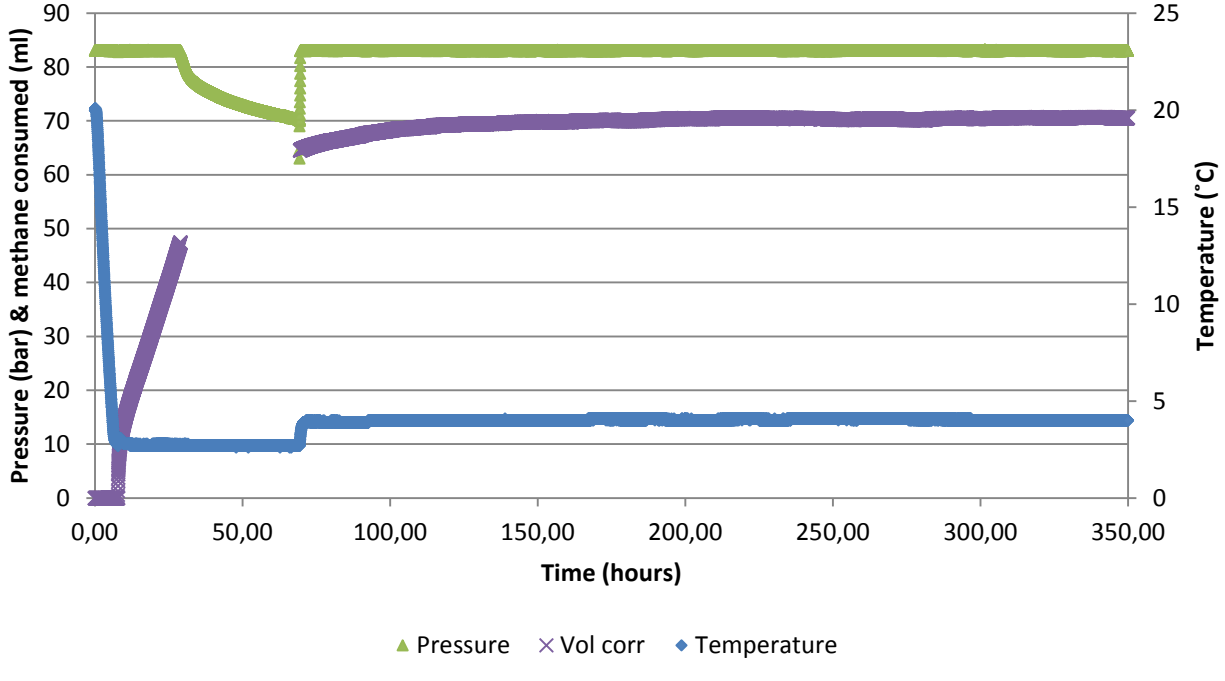


**Figure 5-34. Methane consumption vs time during hydrate formation. The injection pump stopped and thus the methane volume consumed had to be corrected for.**

The three $CO_2$ injections can be seen in Figure 5-35 where the injection curve has the steepest slopes. The differential pressure has a fairly constant value of around 1bar, giving an indication of the permeability relative to previous in-house experiments if required. $CO_2$ flow through the system is observed and gas fractions are measured successfully by the GC (Fig. 5-36). In between the three $CO_2$ flushes the curve showing cumulative volume of gas should be flat. However, this is not the case for the period from around 12 hours to 74 hours where the cumulative volume of gas injected increases. This increase comes from a leak from the outlet pressure transducer and was discovered when the second $CO_2$ injection was supposed to start. Because the leak was located on the outlet side of the core it is impossible to know the composition of the leaked gas. The volume of leaked gas was 33.5ml and the leak was corrected for by multiplying the produced amount in the first flush by 1.085. With a room temperature of 24˚C and an average pressure of 86.6bars (the pump setting), 0.52mol of $CO_2$ was injected between the first and second flushing (calculated using data from NIST web book (Commerce, 2011)). This creates an exchange scenario during the period between the first and second flush, only at a much lower injection rate (0.47ml/hour) than the planned exchanges (6ml/hour). Estimations of the production in the time between the first two flushes have been made.

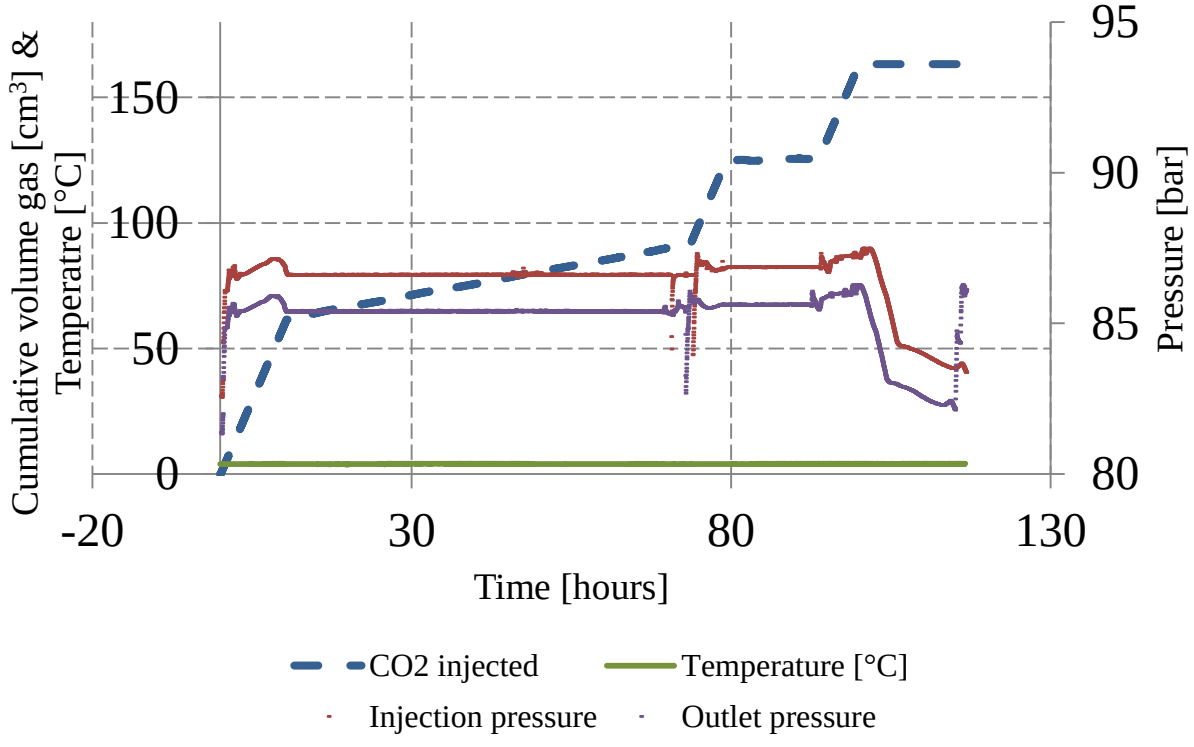


**Figure 5-35. Pump and pressure data. The three highest injection rates are the three CO2 flushes. A significant leak is seen from the slope after the first injection where gas is consumed even though the experiment was stopped.**

The average $CO_2$ mol percentages in effluent gas from the two first flushes are 69% and 97%, respectively. For the estimations of stored $CO_2$ a value of between 97% and 100% $CO_2$ in effluent gas should be used, providing a worst case scenario. Utilizing these numbers an estimated minimum of 0.5044mol of $CO_2$ was produced during the first stop. A total of 2.96mol $CO_2$ was injected from the pump during the whole experiment. A total of 1.57mol of $CO_2$ was produced during the three flushes when the leakage rate is taken into account. These numbers suggest that 0.89mol of $CO_2$ remain in the system, resulting in 30% of the injected $CO_2$ being sequestrated. With a total of 0.43mol of methane in the system before the exchange, the amount of remaining $CO_2$ estimated from this method seem unreasonable at first. Even if it is assumed that 100% of the leaked gas is $CO_2$, the number is high at 0.87 mol. However, it is possible that the $CO_2$ has formed hydrate with excess water as well as remaining as free $CO_2$. Carbon dioxide has a significantly higher molar mass and density than methane and 0.89mol of $CO_2$ in the core corresponds to a volume of 48ml while 0.43mol methane equals 97ml in free form. Consequently this estimation is still within the realms of reality. Table 5-2 shows the stored amount of $CO_2$ using the estimations above, including that all the leaked gas was $CO_2$.

**Table 5-2. Estimated amount of $CO_2$ stored using pump data.**

| Injected $CO_2$ (mol) | Produced $CO_2$ (mol) | Stored $CO_2$ (mol) | Stored $CO_2$ (%) |
|---|---|---|---|
| 2.96 | **2.09** | **0.87** | **29.4** |

Another method for estimating the amount of stored $CO_2$ is to assume that all the free $CH_4$ is replaced with $CO_2$ during the injection and that one mol of $CH_4$ in hydrate is replaced by one mol of $CO_2$ (constant hydration number). However,this method also has uncertainties because some free $CH_4$ will remain in the core as residual gas and the hydration number is not constant. Also, the solubility of the components is not taken into account, hence water may dissolve in $CO_2$ and cause a lower hydrate saturation after the exchange.

If an assumption is made that 97mol% of the leaked gas during the weekend was $CO_2$ and the rest was methane an amount of 0.01mol of methane was produced from hydrate. With the other assumptions made this leads to 0.01mol of $CO_2$ stored in hydrate. The $CO_2$ fraction in hydrate is a calculated fraction of the amount of $CO_2$ in the hydrate and the total amount of guest molecules in the hydrate, while the total fraction of stored $CO_2$ is the fraction of the total amount of injected $CO_2$ remaining in the core. The data from this method is presented in Table 5-3.

**Table 5-3. Estimated amount of $CO_2$ stored using methane formation and production data.**

| $CO_2$ storage estimations in CO2_32 | | | | | |
|---|---|---|---|---|---|
| Before $CO_2$ injection | | **After $CO_2$ injection** | | | |
| $CH_4$ in hydrate (mol) | **Free $CH_4$ in the core (mol)** | **$CO_2$ stored in hydrate (mol)** | **Free $CO_2$ in the core (mol)** | **$CO_2$ fraction in hydrate (%)** | **Total amount of $CO_2$ sequestrated (%)** |
| 0.27 | **0.132** | **0.01** | **0.533** | **3.7** | **18.3** |

Both of these methods have significant uncertainties due to the assumptions made. Some $CO_2$ may have formed with excess water, making the last method an underestimation of stored $CO_2$. However, the amount of methane in the gas composition that leaked during the first stop (when the GC was stopped) may have been less than 3%, resulting in an overestimation of methane being produced from hydrate and an overestimation of $CO_2$ being stored in hydrate.

None of the two methods discussed above offers quantitative information about the amount of $CO_2$ stored. They merely imply that some $CO_2$ is sequestrated in the core, be it as hydrate or as free gas. The true amount may be a number somewhere between these two estimates. However, continuous flow through the system was observed in all three of the injections. This is an essential premise for determining actual amount of stored $CO_2$ in future experiments. In addition, more experiments are needed for statistics in order to determine storage potential.

Figure 5-36 shows the fluid fractions in the effluent during the first $CO_2$ injection, and looks like a typical gas fraction curve from a $CH_4$-$CO_2$ exchange experiment. Before injection was started at 0.1ml/min the entire system - except the core, inlet tubing and outlet tubing – was filled with $CO_2$, hence the initial measurements show a gas fraction of nearly 100% $CO_2$. As time goes by the free methane in the core and outlet tubing reaches the GC and a steep increase in the methane fraction is seen, accompanied by a steep decrease in the carbon dioxide fraction. After reaching the vertices, a symmetrical increase in carbon dioxide and decrease in methane follows, prior to stabilizing at a high carbon dioxide fraction and a low methane fraction. The nitrogen peak originates from nitrogen in free air trapped in the core prior to hydrate formation and confirms that the first samples are indeed free gas from the tubing and the core.

Figure 5-37 shows the recovery of methane for the first $CO_2$ injection, where the majority of the methane is produced and the recovery curves cease. The blue curve shows the recovery when the estimated correction factor for the leak is included. This recovery of around 0.3 from the first flush corresponds with previous in-house studies (Hågenvik, 2013, Hossainpour, 2013).

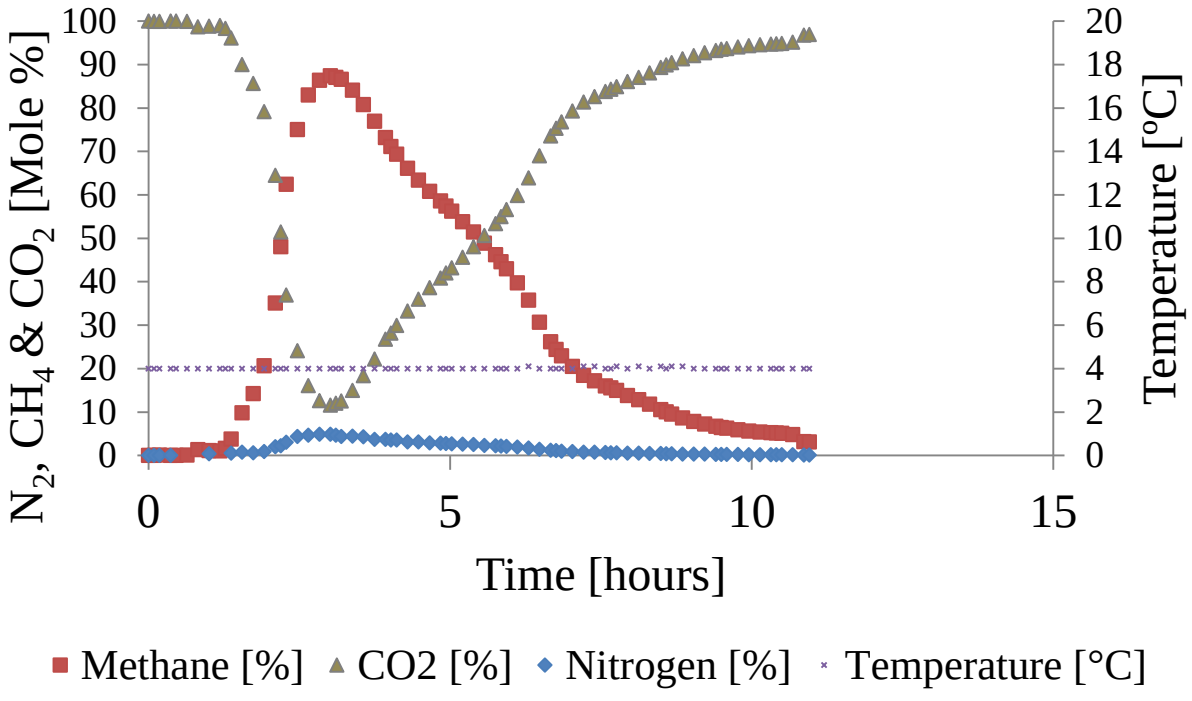


**Figure 5-36. Fluid fractions from GC data in the effluent of the first $CO_2$ injection.**

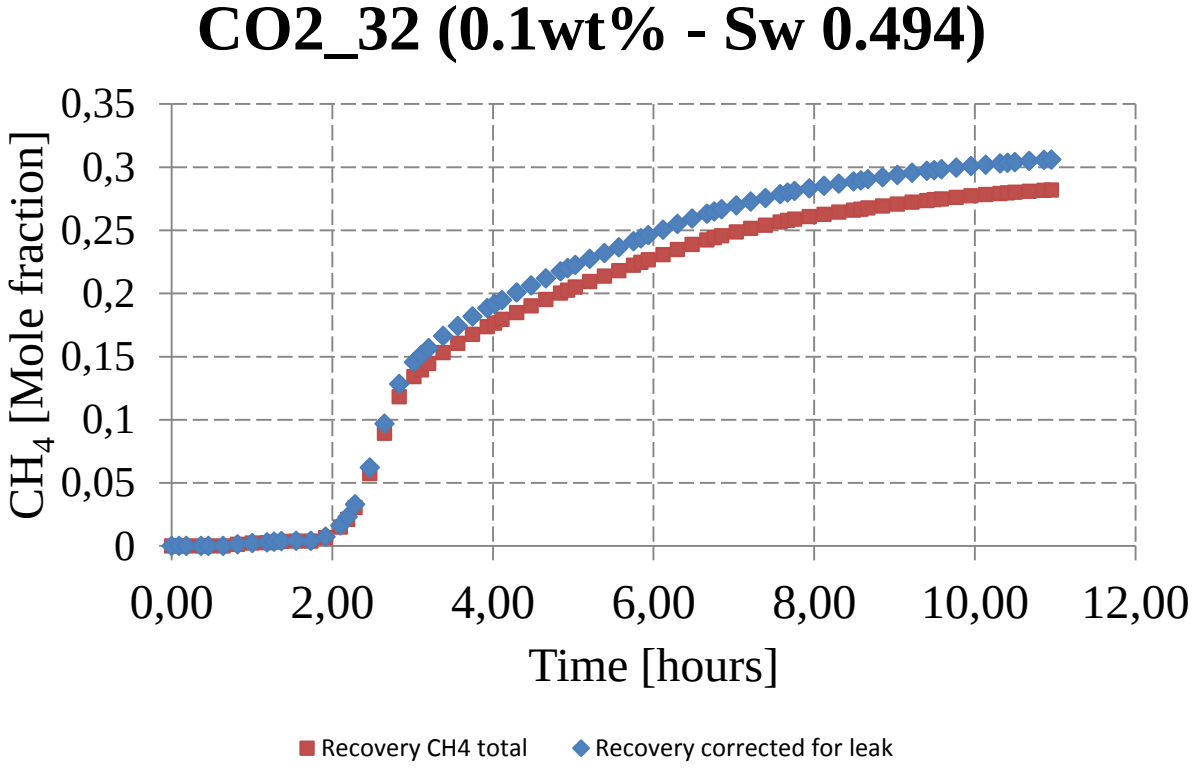


**Figure 5-37. Methane recovery during the first $CO_2$ injection, including recovery corrected for leakage.**

## 5.3.Uncertainties

The instrumental uncertainties in the equipment used for the experiments in this thesis have low uncertainties than the experimental uncertainties. Uncertainties related to human errors, variations in experimental conditions, leaks and equipment failure affect the results more than the equipment uncertainties. This section will address all the relevant uncertainties.

### *General uncertainties*

Temperature and pressure variations and leaks are the most prominent uncertainties. The temperature of the room affects the experiments. In the hydrate lab the thermostat is set to keep a lower temperature at night and the temperature in the CT room at HUS is varying. Pumps keeping constant pressure react too slow and sometimes retract or inject too fast or too slow to keep the pressure constant. This is a major source of error. Leaks are unavoidable and the leak volume is impossible to monitor during experiments. Testing for, and minimizing, leaks is a standard procedure, but still represent a significant uncertainty. Experiments were delayed and equipment had to be changed several times due to leakage. Calipers, injection rate of pumps and pressure gauge readings have uncertainties of ±0.01mm, ±5% and ±2%, respectively. However, the non-uniformity of the stone results in larger errors during cutting of the stone than the caliper readings. The effect of leakage and the pumps ability to maintain desired pressure for rates used in the experiments in this thesis are also more prominent than the equipment uncertainties.

### *Uncertainties related to CT imaging*

Measurements with X-ray CT are subject to a variety of errors and image artefacts including beam hardening, star-shaped or so-called X-artefacts, positioning errors and machine errors (Akin and Kovscek, 2003). Like most CT scanners, the one used for these experiments was developed for medical purposes and was originally intended for qualitative imaging and not for quantitative analysis. The X-ray source delivers a spectrum of X-ray energies and the lower energy, or soft, portions of the X-ray spectrum are absorbed preferentially in the air/sample interface and in the sample itself. The X-ray spectrum then attenuates toward the lower energy portions of the spectrum, introducing an error in the linear attenuation measurement called beam hardening. Reconstruction algorithms and beam filtering provide corrections for beam hardening. However, these methods are not optimized for dense materials such as reservoir rocks.

Another important uncertainty concerning CT imaging is positioning of the core. The position of the core holder must remain constant through the experiment to avoid errors in the process of image subtraction

to obtain fluid-phase saturations. In the experiments conducted for this thesis the core holder did not need to be moved during experiments. However, valves where operated and connections fitted and tightened, thus the possibility that the core holder has been moved exists, although it is improbable.

### *Uncertainties in equilibrating brine and $CO_2$*

The amount of $CO_2$ that will dissolve in brine under the experimental conditions in this thesis was calculated using data from Rochelle (2002). There are uncertainties in reading solubility data from that work; however, calculations were made with a safety margin to make sure that there would be enough $CO_2$ to fully saturate the brine. The brine and $CO_2$ mix was shook in a shaker for several hours, which should be enough. In a similar study by Pentland (2010) the fluids were fully equilibrated within an hour, using a different mixer (Pentland, 2010). Saturating $CO_2$ with brine was done in a similar manner based on data from Sabirzyanov (2000), except the solution was not mixed in the shaker because the container used was too heavy. This may have resulted in the $CO_2$ not being fully saturated with brine. Although the fraction of brine soluble in $CO_2$ is much lower than the fraction of $CO_2$ soluble in brine this may have implications on the displacements. If the fluids were in fact not fully saturated this would result in a lower residual $CO_2$ saturation because more $CO_2$ would be flushed out with the brine instead of being left as immobile droplets.

Experiments have implied that capillary pressure is not affected by dissolution of $CO_2$, i.e. if the brine is not fully saturated (Plug and Bruining, 2007).

### *Uncertainties related to $CH_4$-$CO_2$ exchange*

During the formation of methane hydrate there are some uncertainties that may be of significance. The Bentheim sandstone is assumed to be very homogeneous and porosity and permeability is not measured. If inhomogeneities were to occur, incorrect water saturations may be provided. In the preparation and saturation of the core water may evaporate leading to an underestimation of salinity and an overestimation of initial water saturation.

It is assumed that all free methane present in the core after hydrate formation is produced when injecting carbon dioxide. This methane is seen as zero recovery from hydrate and is therefore a potential underestimation of the exchanged gas. The hydration number is assumed to be constant, when in reality it is not, something that could lead to an error in estimations. All in all, many assumptions were made

and for better comparability between in-house hydrate experiments the same assumptions as in previous experiments on the same setup are used:

- The hydration number (*N*H) was set to a constant value of 5.99
- The grain density for the Bentheim Sandstone was set to 2.65 g/ml
- 26 % volume expansion were used when water formed hydrate
- The room- and core temperature was set to constant values in the calculations
- The temperature gradient between tubing and the core was not taken into account
- The density of water was set to 1.0 g/ml (before NaCl was added)
- The tubing volume between core and inlet/outlet valves was set to 5 ml
- No leakage during production (discussed and corrected for in section 5.2)
- No water production during CO2 injection
- The tortuosity factor *b* in Archie's second law was set to 1.0
- The saturation index *n* in Archie's second law was assumed constant during formation

### *Uncertainties in equipment*

The uncertainties in the equipment used for experiments are provided by the manufacturers and are significantly lower than the experimental uncertainties and uncertainties in the assumptions made. Some examples are given in Table 5-4.

**Table 5-4. Equipment uncertainties given by the manufacturer.**

| Equipment | Measurement | Uncertainty | Unit |
|---|---|---|---|
| **Slide caliper** | Length/diameter | ± 0.005 | cm |
| **GF-3000 Digital Balance** | Weight | ± 0.02 | g |
| **ST Stigma 500** | Flow | ± 0.10 | % |
| **ST Stigma 500** | Pressure | ± 0.10 | % |
| **HH506RA Thermometer** | Temperature | ± 0.1 | ˚C |

An example of uncertainty calculations of pore volume based on equipment uncertainties is provided in Table 5-5, although these uncertainties are insignificant compared to experimental uncertainties and assumptions made. The porosity value is assumed to be 23% based on numerous previous measurements and the homogeneity of Bentheim sandstone. The uncertainty of the porosity is neglected in this example.

The uncertainty of value R, given by variables *x, y, z, …, i*, where $S_{\bar{x}}$, $S_{\bar{y}}$, $S_{\bar{z}}$, … , $S_{\bar{i}}$ are the uncertainties related to each variable, can be calculated by equation:

$$S_{\bar{R}} = \sqrt{\left(\frac{\partial R}{\partial x} S_{\bar{x}}\right)^2 + \left(\frac{\partial R}{\partial y} S_{\bar{y}}\right)^2 + \left(\frac{\partial R}{\partial z} S_{\bar{z}}\right)^2 + \ldots + \left(\frac{\partial R}{\partial i} S_{\bar{i}}\right)^2} \quad (5.1)$$

where $x, y, z, \ldots, i$, are uncorrelated variables and $\bar{x}$, $\bar{y}$, $\bar{z}$, … , $\bar{i}$ , are the arithmetical middle values of the measured variables given by:

$$\bar{x} = \frac{x_1 + x_2 + \ldots + x_N}{N} = \frac{1}{N}\sum_{i=1}^{N} x_i \quad (5.2)$$

The uncertainties related to each value, $S_{\bar{i}}$, are given by:

$$S_{\bar{i}} = \sqrt{a_T^2 + a_M^2} \quad (5.3)$$

where $a_M$is the equipment uncertainty and $a_T$ is the measurement uncertainty given by:

$$a_T = \frac{Mmax - Mmin}{\sqrt{N}} \quad (5.4)$$

Where Mmax is the highest measured value and Mmin is the lowest measured value. N is the number of measurements.

**Table 5-5. Calculated uncertainties in pore volume.**

| Core ID | Weight dry (g) | Length (cm) | Diameter (cm) | Porosity, $\phi$ (%) | PV (ml) |
|---|---|---|---|---|---|
| **CO2_1** | 391.53 ± 0.005 | 9.82 ± 0.02 | 5.02 ± 0.005 | 23% | 44.70 ± 0.2 |
| **CO2_2** | 406.65 ± 0.005 | 10.05 ±0.02 | 5.04 ± 0.005 | 23% | 46.12 ± 0.2 |
| **CO2_3** | 406.31 ± 0.005 | 10 ± 0.005 | 5.04 ± 0.005 | 23% | 45.89 ± 0.2 |
| **CO2_4** | 402.67 ± 0.005 | 9.95 ± 0.01 | 5.03 ± 0.005 | 23% | 45.48 ± 0.2 |
| **CO2_5** | 407.2 ± 0.005 | 10.07 ± 0.02 | 5.04 ± 0.005 | 23% | 46.21 ± 0.2 |

# 6. Conclusions and future work

### *Conclusions*

Five $CO_2$-brine displacement experiments and one $CH_4$-$CO_2$-hydrate exchange experiment have successfully been conducted for the purpose of broadening knowledge concerning $CO_2$ sequestration in saline aquifers. Noteworthy conclusions are:

A functioning setup for high-pressure and elevated temperature CO2-brine displacement experiments has been built and utilized together with a CT scanner in order to observe fluid behavior in porous sandstone samples. CT imaging has proven to be a helpful asset to study the displacement processes in both saturated and unsaturated $CO_2$-brine-sandstone systems. Fluid behavior and distributions, including boundary and hysteresis effects in sandstone cores are successfully visualized using a medical CT scanner.

Residual $CO_2$ saturations of up to 21.9% and 15.4% after a forced imbibition were seen for the 25˚C experiments and the 50˚C experiments, respectively. Higher pressures, and lower temperatures, leading to a higher $CO_2$ density seem to increase residually trapped $CO_2$. This may also be seen as further confirmation that a supercritical $CO_2$-brine-sandstone system is not strongly water-wet, in agreement with literature data.

Differential pressure seems to be the main driving force between displacements, and it closely follows the absolute pressure. Higher differential pressure increases displacements.

A time-efficient method where slugs of water are followed by $CO_2$ injection with decreasing rate is successfully used to emulate a spontaneous imbibition, which otherwise typically is a time-consuming process.

A novel method to measure drainage capillary pressure curves at the core and sub-core scale, presented by Pini (2011), is tested. Pressures at both ends of the core are combined with saturation values calculated from the CT scans to plot capillary pressure curves.

$CO_2$ was injected into a system consisting of brine, methane gas and methane hydrate in Bentheim sandstone and it was observed that $CO_2$ flowed through the and also remained in the system. Estimations indicate that an exchange process between methane and carbon dioxide occurred in the hydrate phase. In addition, $CO_2$ probably was stored as a free liquid phase in the system and, as seen in previous in-house studies, formed hydrate with excess water.

The $CH_4$-$CO_2$ exchange process was conducted with a $CO_2$ injection rate five times higher than in the majority of previous in-house exchange experiments. In general, this significantly reduces the uncertainties related to leakage and the measured mass flow and also improves the efficiency of the experiments.

### *Future work*

More accuracy in regards of keeping a stable absolute pressure, as well as keeping the entire system at desired temperature is the first that comes to mind when reflecting upon the $CO_2$-brine displacement experiments. A different approach for back pressure as well as better isolation or heating of the system, especially tubing, should be looked in to.

It is shown in simulation studies that co-injection of $CO_2$ and brine followed by brine injection improves $CO_2$ storage capacity (Qi et al., 2009). It would be of interest to conduct core scale experiments for verification and further studies on this subject.

A natural next step in the $CO_2$-brine displacement experiments executed for this thesis would be to utilize radioactive tracers, i.e. $C^{11}$, for further visualization using PET/CT. Previous in-house studies utilizing such tracers have provided competency in performing this kind of PET/CT experiments.

Core scale experiments of $CO_2$ storage in $CH_4$ hydrates should be compared with larger scale experiments, i.e. block experiments, as well as numerical simulations at both core and reservoir scale.

To get better estimations of the amount of $CO_2$ stored, multi-step depressurization should be applied. Utilizing known dissociation pressures for methane and $CO_2$ in addition to GC and MFM measurements, more accurate data regarding $CO_2$ sequestration may be obtained. However, dissociation experiments of $CH_4$-$CO_2$ binary hydrates have suggested that hydrate composition remains unchanged upon dissociation (Rovetto et al., 2007).

# References


AKIN, S. & KOVSCEK, A. R. 2003. Computed tomography in petroleum engineering research. *Geological Society, London, Special Publications,* 215**,** 23-38.

BALDWIN, B. A., STEVENS, J., HOWARD, J. J., GRAUE, A., KVAMME, B., ASPENES, E., ERSLAND, G., HUSEBO, J. & ZORNES, D. R. 2009. Using magnetic resonance imaging to monitor CH4 hydrate formation and spontaneous conversion of CH4 hydrate to CO2 hydrate in porous media. *Magn Reson Imaging,* 27**,** 720-6.

BEER 1852. Bestimmung der Absorption des rothen Lichts in farbigen Flüssigkeiten. *Annalen der Physik,* 162**,** 78-88.

BENSON, S. M., TOMUTSA, L., SILIN, D., KNEAFSEY, T. & MILJKOVIC, L. 2005. Core scale and pore scale studies of carbon dioxide migration in saline formations. *Lawrence Berkeley National Laboratory***,** Medium: ED.

BERG, S., OEDAI, S. & OTT, H. 2013. Displacement and mass transfer between saturated and unsaturated CO2–brine systems in sandstone. *International Journal of Greenhouse Gas Control,* 12**,** 478-492.

BIRKEDAL, K. A., ERSLAND, G., HUSEBO, J., KVAMME, B. & GRAUE, A. 2010. Geomechanical Stability During CH4 Production From Hydrates - Depressurization Or CO2 Sequestration With CO2-CH4 Exchange. *44th U.S. Rock Mechanics Symposium and 5th U.S.-Canada Rock Mechanics Symposium, 27-30 June.* Salt Lake City, Utah: American Rock Mechanics Association.

BOSWELL, R. C., T. 2006. The Gas Hydrate Resource Pyramid. Available: http://www.netl.doe.gov/technologies/oil-gas/publications/Hydrates/Newsletter/HMNewsFall06.pdf [Accessed Fall 2006].

BRAUTASET, A., ERSLAND, G., GRAUE, A., STEVENS, J. & HOWARD, J. 2008. USING MRI TO STUDY IN SITU OIL RECOVERY DURING CO2 INJECTION IN CARBONATES

CHAMWUDHIPRECHA, N. & BLUNT, M. J. 2011. CO2 Storage Potential in the North Sea. *International Petroleum Technology Conference, 15-17 November.* Bangkok, Thailand: International Petroleum Technology Conference.

COLLETT, T. 2005. Results at Mallik Highlight Progress in Gas Hydrate Energy Resource Research and Development. *Society of Petrophysicists and Well-Log Analysts*.

COMMERCE, U. S. S. O. 2011. Thermophysical Properties of Fluid Systems. *NIST Chemistry WebBook.*

CONDOR, J. A., SUEBSIRI, J., UNATRAKARN, D., WILSON, M. A. & ASGHARI, K. 2010. Carbon Footprint and Principle of Additionality in CO2-EOR Projects: The Weyburn Case. *SPE Latin American and Caribbean Petroleum Engineering Conference, 1-3 December.* Lima, Peru: Society of Petroleum Engineers.

DAINTITH, J., MARTIN, E. 2010. *A dictionary of science*, Oxford University Press.

DUGSTAD, A. & HALSEID, M. 2012. Internal Corrosion In Dense Phase CO2 Transport Pipelines - State of the Art And the Need For Further R&D. *CORROSION 2012, 11-15 March.* Salt lake City, Utah: NACE International.

EBINUMA, T. 1993. *Method for dumping and disposing of carbon dioxide gas and apparatus therefor*. US 07/846,290.

ERSLAND, G., HUSEBØ, J., GRAUE, A., BALDWIN, B. A., HOWARD, J. & STEVENS, J. 2010. Measuring gas hydrate formation and exchange with CO2 in Bentheim sandstone using MRI tomography. *Chemical Engineering Journal,* 158**,** 25-31.

ERSLAND, G., HUSEBØ, J., GRAUE, A. & KVAMME, B. 2009. Transport and storage of CO2 in natural gas hydrate reservoirs. *Energy Procedia,* 1**,** 3477-3484.

GRAUE, A., KVAMME, B., BALDWIN, B. A., STEVENS, J., HOWARD, J., ASPENES, E., ERSLAND, G., HUSEBØ, J. & ZORNES, D. 2006a. Environmentally Friendly CO2 Storage in Hydrate Reservoirs Benefits

From Associated Spontaneous Methane Production. *Offshore Technology Conference, 1-4 May.* Houston, Texas, USA: Offshore Technology Conference.
GRAUE, A., KVAMME, B., BALDWIN, B. A., STEVENS, J., HOWARD, J. J., ERSLAND, G., HUSEBO, J. & ZORNES, D. R. 2006b. Magnetic Resonance Imaging of Methane - Carbon Dioxide Hydrate Reactions in Sandstone Pores. *SPE Annual Technical Conference and Exhibition, 24-27 September.* San Antonio, Texas, USA: Society of Petroleum Engineers.
HALLAND, E. K., MUJEZINOVIC, J., RIIS, F., BJØRNESTAD, A., MELING, I. M., GJELDVIK, I. T., TAPPEL, I. M., BJØRHEIM, M., RØD, R. S. & PHAM, V. T. H. 2014. CO2 Storage Atlas - Norwegian Continental Shelf. *In:* HALLAND, E. K., MUJEZINOVIC, J. & RIIS, F. (eds.).
HAMRE HÅHEIM, T. 2013. *Methane Production from Natural Gas Hydrates.* MSc., University of Bergen.
HESTER, K. C., BREWER, P. G. 2009. Clathrate Hydrates in Nature. *Annual Review of Marine Science,* Vol. 1: 303-327 (Volume publication date January 2009)**,** 303-327.
HOEGH-GULDBERG, O., MUMBY, P. J., HOOTEN, A. J., STENECK, R. S., GREENFIELD, P., GOMEZ, E., HARVELL, C. D., SALE, P. F., EDWARDS, A. J., CALDEIRA, K., KNOWLTON, N., EAKIN, C. M., IGLESIAS-PRIETO, R., MUTHIGA, N., BRADBURY, R. H., DUBI, A. & HATZIOLOS, M. E. 2007. Coral Reefs Under Rapid Climate Change and Ocean Acidification. *Science,* 318**,** 1737-1742.
HOSSAINPOUR, R. 2013. *Catalysts for Enhanced $CO_2$-$CH_4$ Exchange in Natural Gas Hydrates.* Master of Science, University of Bergen.
HUSEBØ, J. 2008. *Monitoring depressurization and CO2-CH4 exchange production scenarios for natural gas hydrates.* PhD, University of Bergen.
HØYLAND, M. D. 2014. *Measurements and visualization of hydrate growth in porous media.* Master of Science, University of Bergen.
HÅGENVIK, C. 2013. *$CO_2$ Injection in Hydrate bearing Sandstone with Excess Water.* M. Sc., University of Bergen.
IGLAUER, S., PALUSZNY, A., PENTLAND, C. H. & BLUNT, M. J. 2011a. Residual CO2 imaged with X-ray micro-tomography. *Geophysical Research Letters,* 38**,** L21403.
IGLAUER, S., WÜLLING, W., PENTLAND, C. H., AL-MANSOORI, S. K. & BLUNT, M. J. 2011b. Capillary-Trapping Capacity of Sandstones and Sandpacks.
INTERGOVERNMENTAL PANEL ON CLIMATE CHANGE, I. 2005. Carbon Dioxide Capture and Storage. *In:* MEYER, B. M. O. D. H. D. C. M. L. L. (ed.).
INTERGOVERNMENTAL PANEL ON CLIMATE CHANGE, I., WORKING GROUP I 2013. Climate Change 2013 The Physical Science Basis. *In:* PRESS, C. U. (ed.). 32 Avenue of Americas, New York: IPCC.
INTERGOVERNMENTAL PANEL ON CLIMATE CHANGE, I., WORKING GROUP III 2014. Mitigation of Climate Change. IPCC.
JEFFREY, G. A. 1984. Hydrate inclusion compounds. *Journal of inclusion phenomena,* 1**,** 211-222.
KOMAI, T., YAMAMOTO, Y. & OHGA, K. 2000. Dynamics of Reformation and Replacement of CO2 and CH4 Gas Hydrates. *Annals of the New York Academy of Sciences,* 912**,** 272-280.
KOMAI, T. K., T.; KANG, S.; NAGASHIMA, K.; YAMAMOTO, Y 2002. In situ observation of gas hydrate behaviour under high pressure by Raman spectroscopy. *Journal of Physics: Condensed Matter,* 14.
KVAMME, B., GRAUE, A., BUANES, T., KUZNETSOVA, T. & ERSLAND, G. 2007. Storage of CO2 in natural gas hydrate reservoirs and the effect of hydrate as an extra sealing in cold aquifers. *International Journal of Greenhouse Gas Control,* 1**,** 236-246.
LEE, H., SEO, Y., SEO, Y. T., MOUDRAKOVSKI, I. L. & RIPMEESTER, J. A. 2003. Recovering methane from solid methane hydrate with carbon dioxide. *Angew Chem Int Ed Engl,* 42**,** 5048-51.
MAKOGON, I. U. F. 1997. *Hydrates of hydrocarbons,* Tulsa, Okla. :, PennWell Pub. Co.
MAKOGON, Y. F. 2010. Natural gas hydrates – A promising source of energy. *Journal of Natural Gas Science and Engineering,* 2**,** 49-59.

MCGRAIL, B. P. Z., T.; HUNTER, R. B.; WHITE, M. D.; PATIL, S. L.; KULKARNI, A. S. 2004. A New Method for Enhanced Production of Gas Hydrates with CO2. *AAPG Hedberg Conference - "Gas Hydrates: Energy Resource Potential and Associated Geologic Hazards".* Vancouver, Canada.

MORIDIS, G. J. & COLLETT, T. S. 2003. Strategies for gas production from hydrate accumulations under various geological and reservoir conditions. *TOUGH Symposium.* Lawrence Berkeley National Laboratory, Berkeley, California.

MORIDIS, G. J., COLLETT, T. S., BOSWELL, R., KURIHARA, M., REAGAN, M. T., KOH, C. & SLOAN, E. D. 2009. Toward Production From Gas Hydrates: Current Status, Assessment of Resources, and Simulation-Based Evaluation of Technology and Potential. *SPE Reservoir Evaluation & Engineering,* 12**,** 745-771.

MORIDIS, G. J. & SLOAN, E. D. 2006. Gas production potential of disperse low-saturation hydrate accumulations in oceanic sediments. *Lawrence Berkeley National Laboratory*.

MOSHER, D. C., LOUDEN, K., LEBLANC, C., SHIMELD, J. & OSADETZ, K. 2005. Gas Hydrates Offshore Eastern Canada: Fuel For The Future? *Offshore Technology Conference, 2-5 May.* Houston, Texas, USA: Offshore Technology Conference.

NGHIEM, L., SHRIVASTAVA, B., KOHSE, M., HASSAM, C. & YANG 2010. Simulation and Optimization of Trapping Processes for $CO_2$ Storage in Saline Aquifers. *Canadian International Petroleum Conference.* Calgary, Canada: SPE.

NGHIEM, L. X., SHRIVASTAVA, V. K., TRAN, D., KOHSE, B. F., HASSAM, M. S. & YANG, C. 2009. Simulation of CO2 Storage in Saline Aquifers. *SPE/EAGE Reservoir Characterization & Simulation Conference* Society of Petroleum Engineers.

OTA, M., MOROHASHI, K., ABE, Y., WATANABE, M., SMITH, J. R. L. & INOMATA, H. 2005. Replacement of CH4 in the hydrate by use of liquid CO2. *Energy Conversion and Management,* 46**,** 1680-1691.

PENTLAND, C. H. 2010. *Measurements of Non-wetting Phase Trapping in Porous Media.* Doctor of Philosophy, Royal School of Mines, Imperial College London.

PENTLAND, C. H., EL-MAGHRABY, R., IGLAUER, S. & BLUNT, M. J. 2011. Measurements of the capillary trapping of super-critical carbon dioxide in Berea sandstone. *Geophysical Research Letters,* 38**,** L06401.

PERRIN, J.-C. & BENSON, S. M. 2009. An Experimental Study on the Influence of Sub-Core Scale Heterogeneities on CO2 Distribution in Reservoir Rocks. *Transport in Porous Media*.

PERRIN, J.-C., KRAUSE, M., KUO, C.-W., MILJKOVIC, L., CHAROBA, E. & BENSON, S. M. 2009. Core-scale experimental study of relative permeability properties of CO2 and brine in reservoir rocks. *Energy Procedia,* 1**,** 3515-3522.

PINI, R., KREVOR, S. C. M. & BENSON, S. M. 2011. Capillary pressure and heterogeneity for the CO2/water system in sandstone rocks at reservoir conditions. *Advances in Water Resources,* 38**,** 48-59.

PLUG, W. J. & BRUINING, J. 2007. Capillary pressure for the sand–CO2–water system under various pressure conditions. Application to CO2 sequestration. *Advances in Water Resources,* 30**,** 2339-2353.

QI, R., LAFORCE, T. C. & BLUNT, M. J. 2009. Design of carbon dioxide storage in aquifers. *International Journal of Greenhouse Gas Control,* 3**,** 195-205.

RAMSTAD, T. & RUESLÅTTEN, H. 2013. Technical Report from Task 1.

RICHARDSON, J. G., KERVER, J. K., HAFFORD, J. A. & OSOBA, J. S. 1952. Laboratory Determination of Relative Permeability. *Journal of Petroleum Technology,* 4**,** 187-196.

ROCHELLE, C. A. & MOORE, Y. A. 2002. The solubility of supercritical $CO_2$ into pure water and synthetic Utsira porewater. Keyworth, Nottingham: British Geological Survey.

ROCHELLE, C. A. M., Y. A. 2002. The solubility of supercritical $CO_2$ into pure water and synthetic Utsira porewater. Keyworth, Nottingham: British Geological Survey.

ROVETTO, L. J., BOWLER, K. E., STADTERMAN, L. L., DEC, S. F., KOH, C. A. & SLOAN, E. D. 2007. Dissociation studies of CH4–C2H6 and CH4–CO2 binary gas hydrates. *Fluid Phase Equilibria,* 261**,** 407-413.

SABIRZYANOV, A. N., IL`IN, A. P., AKHUNOV, A. R. & GUMEROV, F. M. 2000. Solubility of Water in Supercritical Carbon Dioxide. *High Temperature,* 40**,** 203-206.

SCHODERBEK, D., MARTIN, K. L., HOWARD, J., SILPNGARMLERT, S. & HESTER, K. 2012. North Slope Hydrate Fieldtrial: CO2/CH4 Exchange. *OTC Arctic Technology Conference, 3-5 December.* Houston, Texas: Offshore Technology Conference.

SEEBURGER, D. A. 1981. *Studies of natural fractures, fault zone permeability, and a pore space-permeability model.* Doctor of Philosophy, The Board of Trustees of the Leland.

SENGUL, M. 2006. CO2 Sequestration - A Safe Transition Technology. *SPE International Health, Safety & Environment Conference, 2-4 April.* Abu Dhabi, UAE: Society of Petroleum Engineers.

SIBSON, R. H. 1995. Selective fault reactivation during basin inversion: potential for fluid redistribution through fault-valve action. *Geological Society, London, Special Publications*.

SINGH, V. P., CAVANAGH, A., HANSEN, H., NAZARIAN, B., IDING, M. & RINGROSE, P. S. 2010. Reservoir Modeling of CO2 Plume Behavior Calibrated Against Monitoring Data From Sleipner, Norway. *SPE Annual Technical Conference and Exhibition, 19-22 September.* Florence, Italy: Society of Petroleum Engineers.

SIRA, J. H., PATIL, S.L., KAMATH, V.A., U. OF ALASKA, FAIRBANKS 1990. Study of Hydrate Dissociation by Methanol and Glycol Injection. *SPE Annual Technical Conference and Exhibition, 23-26 September 1990.* New Orleans, Louisiana: Society of Petroleum Engineers.

SLOAN, E. D. & KOH, C. A. 2008. *Clathrate hydrates of natural gases (third edition)*, Boca Raton, Fla., CRC Press.

STANTON, R., FLORES, R., WARWICK, P. D., GLUSKOTER, H. & STRICKER, G. D. Coal bed sequestration of carbon dioxide. *In:* SURVEY, U. S. G. (ed.).

STATISTICS NORWAY, S. N. 2014. *Emissions of greenhouse gases* [Online]. Division for Energy and Envirnomental Statistics: Statistics Norway. Available: http://www.ssb.no/en/klimagassn/.

THIBEAU, S., NGHIEM, L. X. & OKHUMA, H. 2007. A Modeling Study of the Role of Selected Mineral in Enhancing CO2 Mineralization During CO2 Aquifer Storage. *SPE Annual Technical Conference and Exhibition.* Anaheim, California.

TREIBER, L. E. & OWENS, W. W. 1972. A Laboratory Evaluation of the Wettability of Fifty Oil-Producing Reservoirs. *Society of Petroleum Engineers Journal,* 12**,** 531-540.

VINEGAR, H. J., SHELL DEVELOPMENT CO. 1986. X-Ray CT and NMR Imaging of Rocks. *Journal of Petroleum Technology,* Volume 38.

WANG, X. & ECONOMIDES, M. J. 2011. Natural Gas Hydrates as an Energy Source - Revisited. *International Petroleum Technology Conference, 15-17 November.* Bangkok, Thailand: International Petroleum Technology Conference.

WILKINSON, D. 1986. Percolation effects in immiscible displacement. *Physical Review A,* 34**,** 1380-1391.

WITHJACK, E. M., ARCO OIL AND GAS CO. 1988. Computed Tomography for Rock-Property Determination and Fluid-Flow Visualization. *SPE Formation Evaluation,* Volume 3.

WRIGHT, I. W., RINGROSE, P. S., MATHIESON, A. S. & EIKEN, O. 2009. An Overview of Active Large-Scale CO2 Storage Projects. *SPE International Conference on CO2 Capture, Storage, and Utilization, 2-4 November.* San Diego, California, USA: Society of Petroleum Engineers.

# APPENDIX

## Nomenclature

| | | |
|---|---|---|
| $\Delta G$ | = | Gibbs free energy |
| $\boldsymbol{\phi}$ | = | Porosity |
| $\mu$ | = | Viscosity |
| dp | = | Pressure difference |
| $\theta$ | = | Contact angle |
| $P_{nw}$ | = | Pressure in non-wetting phase |
| $P_w$ | = | Pressure in wetting phase |
| $P_C$ | = | Capillary pressure |
| $\sigma$ | = | Interfacial tension (IFT) |
| r | = | Radius |
| Å | = | Ångstrøm ($10^{-10}$m) |
| $S_w$ | = | Water saturation |
| $S_{wc}$ | = | Connate water saturation |
| $S_{wi}$ | = | Initial water saturation |
| $\mu_a$ | = | Linear attenuation coefficient |
| I | = | Intensity |
| EOR | = | Enhanced oil recovery |
| Sc | = | Supercritical |
| GC | = | Gas chromatograph |
| MFM | = | Mass flow meter |

# Appendix A

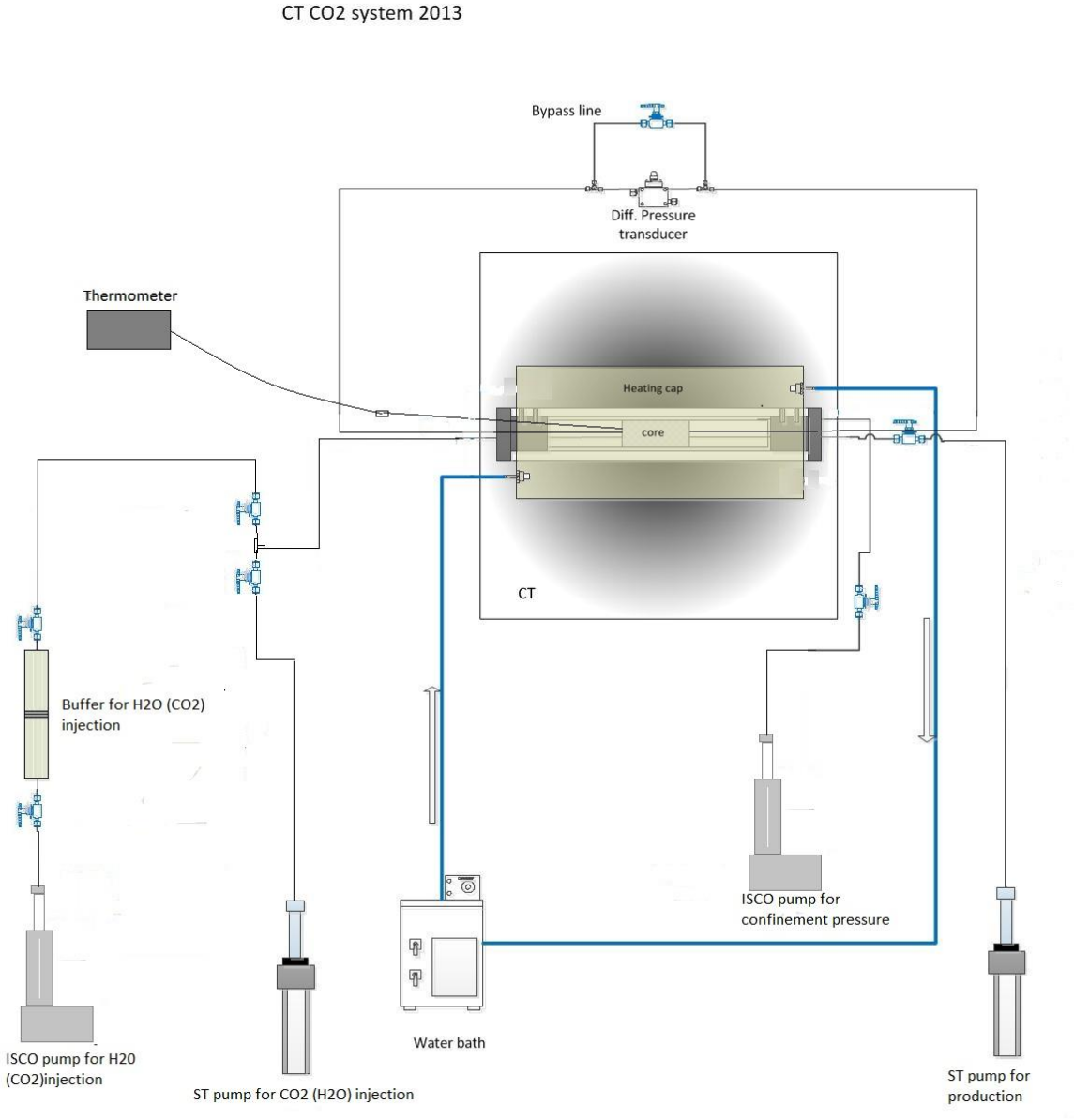


**Figure A1. Experimental setup at Haukeland University Hospital modified for the possibility co-injecting $CO_2$ and brine (although co-injection was not performed).**